Università
Ca'Foscari
Venezia

Master's Degree programme

in Sustainable Chemistry and Technologies
"Second Cycle (D.M. 270/2004)"
Final Thesis

Study and morphological characterization of copper sulphide-based nanoparticles

Supervisor
Ch. Prof. Patrizia Canton

Graduand
Gloria Saorin
Matriculation Number 846278

Academic Year
2017/ 2018

Summary

Abstract 5
Introduction 6
Nanotechnology 6
Plasmonic nanocrystals 6
Drude Model 7
Necessary conditions for LSPR in nanocrystals 8
Losses in plasmonic nanocrystals 9
Mie theory 9
Colloidal synthetic methods 10
Heat up method 10
Copper sulphides 13
LSPR in copper sulphides $Cu_{2-x}S$ system 15
Stoichiometry-dependence 15
Surrounding medium 16
Size 17
Shape 18
Interactions between particles 18
Uses and challenges 19
Aim of the thesis 21
Experimental part 22
Characterization 22
Scanning Electron Microscopy (SEM) 22
Transmission Electron Microscopy (TEM) 22
X Ray Diffraction (XRD) 22
FT-IR Spectroscopy 23
UV-VIS-NIR Spectroscopy 23
DLS analysis 23
Chemicals 24
Nanodisks 25
Heat up nanodisks synthesis 25
CuS nanodisk protocols 28
Materials 31
Results and discussion 31
Synthesis of copper sulphides nanoparticles thought a green approach 57
CuS-NPs synthetic protocols 58
CuS-CIT ligand trisodiumcitrate 59
CuS-PAA ligand polyacrylic acid 68

CuS-CTAB ligand Cetyl trimethylammonium bromide 78
Comparison between NPs 88
Conclusions 90
Bibliography 91

Abstract

In this thesis different synthetic approaches for obtaining copper sulphide nanoparticles have been studied with particular attention to the condition for obtaining covellite phase and monodisperse nanoparticles.
Mainly oval shaped copper sulphide nanoparticles have been obtained via a synthesis at low temperature in water medium. This study shows that by varying the organic capping ligand the nanoparticles produced have different size distribution, morphology and crystallographic phases.
The synthesis of copper sulphide nanocrystals with a disk-like morphology has also been studied.
The plasmonic behaviour for all the synthesized nanoparticles have been experimentally investigated by UV-VIS absorption, their morphology and average size by means of TEM, SEM and DLS together with X-ray diffraction to understand their crystallographic phases.
The copper sulphide nanoparticles synthesized in this work can be used as photothermal mediators and so employed in the treatment of tumours.

Introduction

Nanotechnology

Over the last several decades the research area of nanotechnology has been developed and impacted on many aspects of the modern society. The nanotechnology is the study and the control of matter with at least one nanometric dimension (1-100nm) that shows different physical, chemical and biological properties compared to bulk materials and to molecules or atoms. (Zhang et al. 2008; Xie, Carbone, et al. 2013)(National Nanotechnology Initiative 2018)

In nanotechnology two approaches are mainly used:

- Bottom-up approach: starting from molecular components, nanomaterials are produced by their spontaneous chemical interaction
- Top-down approach: nanomaterials are produced via high-controlled miniaturization of bulk materials

For materials with nanometric dimension, properties such as fluorescence, electrical conductivity, melting point, magnetic permeability and chemical reactivity depend on particle size and it is called quantum size effects. Quantum effects make tunability of properties possible, i.e. by changing the particle size a specific material property can be fine-tuned.
Another characteristic of nanoscale materials, is the large surface area per mass of material that makes these particles more reactive and usable in numerous fields such as in catalysis or drug delivery.
Nanotechnology is applied in medical research and give the opportunity to develop a more precise and personalized treatment for patients.

Plasmonic nanocrystals

Plasmonic nanocrystals (NCs) are nanoparticles on which collective oscillation of free charge carriers (plasmon) can be induced by an incident light. This phenomenon is called, at nanometric scale, localized surface plasmon resonances (LSPR) and it is showed by particles with smaller dimension than the wavelength of the incident light.
Since there are numerous different ways to achieve a population of free carrier in a nanoparticle, there are many useable materials. Metals like copper, silver and gold have been widely used to obtain plasmonic nanocrystals; they are characterized by easy synthesis comparing to other metals and a convenient energy range of LSPR. For these reasons, nanocrystals of Cu, Ag and Au have been extensively studied and are suitable for several applications. The major issue of these metal nanocrystal is their high optical losses due to electronic transitions. Possible materials that can be used as alternative to metals for producing plasmonic nanocrystals have been developed and can be grouped into three categories:

1. Extrinsically doped semiconductors and metal oxides NCs

In this NCs dopant atoms are introduced to provide the extra carriers. Generally, since a certain number of the extra carriers can be trapped or can't have enough mobility, their number resulted to be comparable in terms of order of magnitude to the number of impurities but a bit lower. The tuning of these material is possible both during the synthesis and post-synthesis.

2. Self-doped materials, i.e. copper deficient copper chalcogenides[1] and oxygen deficient metal oxides NCs.
Self-doped materials have a non-stoichiometric phase and free carrier are present as a result of the variation of the oxidation state of generally one of their elements that result in extra electrons in the conduction band

[1] Chemical compound which contains at least one chalcogen anion. A chalcogen is an element of the 16 group of periodic table i.e. O, S, Se, Te, Po.

or in holes in an otherwise filled valence band. This condition can also be achieved by a post synthesis redox reaction.

3. Metal Oxides NCs

These materials have a conductive behaviour due to their electronic structures.

For the firsts two categories the free carrier' concentration can be tuned, this is not possible with metals.

Drude Model

The Drude Model is the first model developed in 1900 for the dielectric permittivity in metals. In this model electrons are considered as free particles of a gas (plasma) and it uses the classical statistical distribution of Boltzmann to describe them. This model is an oversimplification of the system and has some limits but is an easy tool to understand LSPR in nanocrystals. Dielectric permittivity is described by a complex function of the external electric field's frequency:

$$\varepsilon(\omega) = \varepsilon' + i\varepsilon'' = \varepsilon_\infty - \frac{\omega_p^2}{\omega_+^2\gamma^2} + i\frac{\omega_P^2\gamma}{w(\omega^2+\gamma^2)}$$

ε_∞ background dielectric constant
γ Dumping parameter

This parameter describes the dumping of the collective oscillations. In Drude model which uses a classical approach, this parameter represents carriers scattering: the dumping parameter is the result of different contributes of scattering between electron and phonons, other electrons, defects and the surface.

$$\gamma = \gamma_{e-e} + \gamma_{e-phonon} + \gamma_{e-defect} + \gamma_{e-surface}$$

When NC size is comparable to the mean free path of the carriers γ is bigger than for the corresponding bulk material because the carriers scattering with the surface is relevant.
ω_p Plasma frequency

$$\omega_p{}^2 = \frac{n_e e^2}{\varepsilon_0 m^*}$$

n_e carrier density

m* carrier effective mass

Free carriers can be excited by an external electric field of an electromagnetic radiation, causing their displacement from the equilibrium position in the lattice. Free carriers (plasma) generate coherent and collective oscillation with a particular frequency called plasma frequency. The oscillation of the carriers is due to the external electric field applied and to the restoring force that ions in the lattice exert on free carriers returning them to their equilibrium position. LSPR can be considered as a spring-mass harmonic oscillator where free electrons density is the equivalent mass while coulomb restoring force is the spring constant.
The oscillating movement of carriers is defined as plasmonic mode or plasmon.

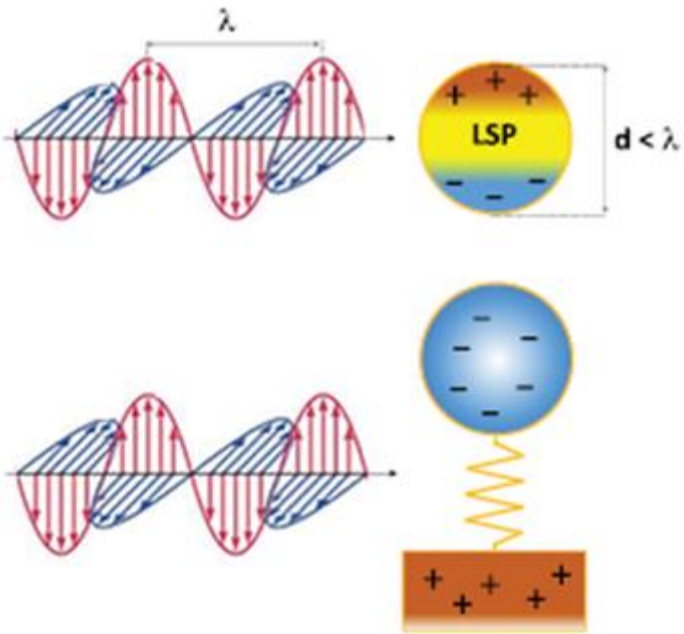

Figure 1 illustration of a LSPR excited by light in a spherical nanoparticle above, LSPR is represented as a spring-mass harmonic oscillator where free electron density is the equivalent mass, below. (Amendola et al. 2017)

Necessary conditions for LSPR in nanocrystals

To show LSPR a NC needs to be bigger than a couple of nanometres and smaller than 1/5 of the LSPR's wavelength. In that case inside the nanocrystal the dielectric polarization can be assumed as uniform and the electronic structure of the particle can be regarded as the one in bulk material. These approximations allow to describe the coherent response of free carriers with the laws of electrostatics and therefore the electrons (considering a metal) cloud distortion caused by an incident light radiation can be expressed by polarizability of the metal α.

For a spherical particle:

$$\alpha = 4\pi R^3 \frac{\varepsilon - \varepsilon_m}{\varepsilon + 2\varepsilon_m}$$

α electronic polarization
R radius of the particle
ε_m dielectric permittivity of embedding medium
ε(ω) complex dielectric function

From this equation it is possible to arrive to the expression of the extinction cross-section σ of a particle and it results that this parameter scales with particle volume, the plasmonic properties of materials are described by their ε(ω) and that LSPR is excited when the frequency of the radiation is:

$$\varepsilon'(\omega) = -\chi\, \varepsilon_m \quad \textit{Frolich condition}$$

ε'(ω) real component of complex dielectric permittivity
χ geometrical factor (2 for a sphere)

The Frolich condition is valid if the imaginary component of ε is small or weakly dependent on frequency. Frolich condition is a clear explanation of the LSPR sensitivity to the local environment. With the increase of the ε_m the Coulomb restoring force decreases and so does the LSPR. The displacement of the charges, that occurs in the LSPR, can be seen as an oscillating dipole that gives rise to an oscillating field that reach the surrounding of the particle. That field decays exponentially with distance around the particle surface and is orders of magnitude enhanced with respect to the incoming electric field. This explain the high sensitivity of LSPR to the surrounding medium that is useful in the application of plasmonics as sensors. The influence of ε_m on the LSPR is clearly evidenced in the equation for ω_{LSPR} (that shows the fulfil of the resonance condition):

$$\omega_{LsPR} = \sqrt{\frac{\omega_p^2}{1+2\varepsilon_m} - \gamma^2}$$

The equation reported above is valid only for spherical particles when the quasi-static approximation is valid (Kriegel, Scotognella, and Manna 2017).

This is valid for all materials with free carriers and metallic behaviour. To exhibit metallic behaviour ε'(ω) has to be negative. Since Drude model define ε'(ω) as:

$$\varepsilon'(\omega) = \varepsilon_\infty - [\omega_p^2 / (\gamma^2 + \omega^2)]$$

From this equation it is clear that exist a cross-over frequency ω_c below which ε' is negative. Replacing ω_p with its formula a minimum number of free carriers for having a metallic behaviour at ω_c can be calculated as:

$$n_{\min} = \frac{\varepsilon_\infty \varepsilon_0 m^*}{e^2}(\omega_c^2 + \gamma^2)$$

Hence, the higher the density of the carriers the broader will be the range of ω for which the material behaves as a metal.

Losses in plasmonic nanocrystals

The persistence of plasmonic oscillations is limited in time by losses. Losses are due to different process and are described, in Drude model, by the imaginary component of the dielectric permittivity ε''(ω). Some of the possible process causing losses are structural imperfection, radiative damping and heating but in the majority of cases for plasmonic system the most important process is intraband transition that is simultaneous to the excitation of LSPR. Drude model does not take into account the actual band structure of materials since it uses a classical approach. Anyway, the imaginary term in the Drude model can describe losses due to intraband transitions in wide range of frequencies since these can be contemplated by the classical scattering theory. Indeed, intraband transitions process creates electron-hole couples and this increases the rate of electron-electron scattering (considering a metal nanoparticle).

γ = e / (μ m*) damping parameter in Drude model

m* effective mass
μ carrier mobility

In doped and self-doped semiconductors, the carrier mobility decreases if carriers' density increases. For doped semiconductor to increase the carrier density a larger concentration of dopants is required and this causes impurities scattering while for self-doped semiconductors the dumping parameter increase since the vacancies are distributed in the lattice in a disordered mode. If the materials contain domains of multiple phases additional complication has to be taken into account.
Losses influence the LSPR width (and the dephasing time that is inversely proportional). The higher is the dumping factor the broader would be the LSPR band. The quality factor is defined as the ratio between the LSPR peak energy and the full width at half maximum, the stronger is the LSPR response the higher is the factor.

Mie theory

Mie theory is the easiest theory that allows to define the optical properties for a spherical, homogenous particle embedded in a dielectric medium. Beside to spherical particles this theory can be applied to other spheroids such as rods, wires and also to platelets and disks which are extreme case of spheroids. For particles with circular cross section two modes are possible for their plasmon resonance:

- Transverse or out of plane mode

- Longitudinal or in plane mode

This can be understood since the field arising from charge displacement due to LSPR, is strongly affected by the nanocrystal shape and it would experience a stronger localization around tips or small radius apexes. Mie theory is valid only under certain conditions such as not interacting particles, embedding medium transparent in the region of LSPR, and if the size effects are negligible. If these conditions are not respected more complex theory should be taken into account (Comin and Manna 2014).

Further information will be given in the experimental part.

Colloidal synthetic methods

Since physical and chemical properties of nanocrystals are size-dependent in the last two decades a huge number of researches focused on obtaining monodisperse nanocrystals. Through wet-chemical colloidal synthesis it is possible to produce a wide range of particles, controlling their size and minimizing their polydispersity. The hot-injection method has been the first developed method, it relays on a rapid injection of one of precursor solution in the heated reaction vessel. The solution obtained right after the injection is supersaturated since the injection of the precursor solution allows a fast and good mixing and make the temperature drop and therefore a burst-like nucleation event takes place. A lot of different synthetic protocols with this method are reported in literature (Xie, Carbone, et al. 2013; Zhang et al. 2008). The hot injection method is still the most useful for producing homogeneous nanocrystals. Nowadays the growing number of possible applications of nanocrystals require production methods which can be scaled for producing large quantities of nanoparticles. The intrinsic process that makes the hot injection method a way to achieve monodispersion also prevent it from be scaled. In order to develop scalable synthesis, the heat up technique (or non-injection) has been settled.

Heat up method

In the heat up method all the reagents are mixed into the reaction vessel and after heated in a controlled way to induce nucleation and growth process.

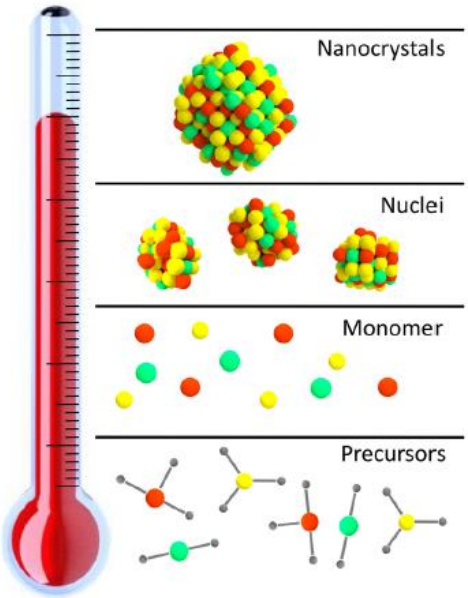

Figure 2 illustration of the stages in a heat up synthesis (Van Embden, Chesman, and Jasieniak 2015)

Precursors are the initial reagents or complex that are formed from reagents and ligands in solution. Precursors are the species present at low temperature, with the heating of the reaction vessel they convert into monomers. With the temperature increase the nucleation is induced and the continued heating makes the nuclei to growth.

In order to achieve monodispersity the nucleation process has to occur in a short time, generate a large number of nuclei and the growth process have to follow the nucleation. In an ideal process when the concentration exceeds the saturation concentration the nucleation occurs producing a large number of nuclei in a short time. With the fast growth of these nuclei the concentration drops below the nucleation level (critical supersaturation level) and therefore the nucleation ends while the growth can continue and in this way nucleation step is separated from growth. This process is represented in diagram, reported in Figure 2. This nucleation condition is neither a necessary nor sufficient condition for monodisperisity (Viswanatha and Sarma 2007), however, the key idea of separating growth and nucleation stage is widely seek in literature for synthesis of monodisperse nanocrystal (hot injection with a burst nucleation event permit the separation of this process from growth).

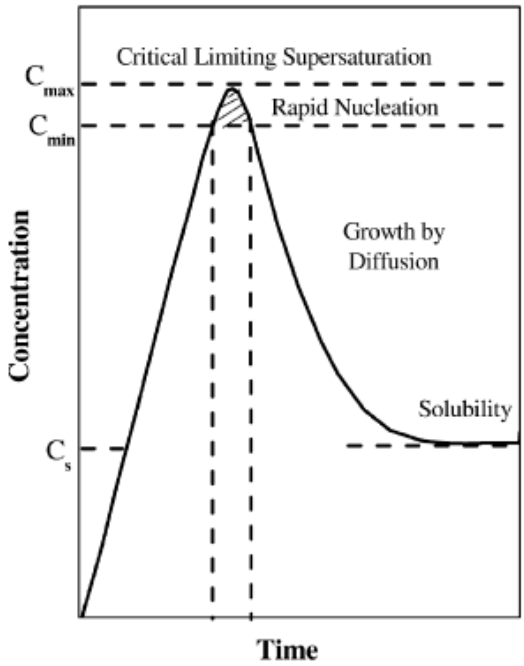

Figure 3La Mer diagram showing the ideal process to achieve monodispersity (Viswanatha and Sarma 2007).

In a het up synthesis in order to achieve fast, and separated from growth, nucleation the chemistry of ligands and precursors has to be taken into account. For obtaining the desired composition and phase purity of the product the reactivity of each component has to be fixed.

Stages of heat-up synthesis

1→ Monomers formation

Nanocrystals require monomers to nucleate and grow. At low temperature reagents are present as precursors and so bonded to ligands. Precursors have to disassociate from ligands to form monomers. Precursors reactivity is related to the ligand's binding constant and to reaction temperature. Basing on calculation reported in literature (Van Embden, Chesman, and Jasieniak 2015) during the heating stage the conversion of precursors to monomers increases exponentially. Knowing that supersaturation S= [M]/[M_0] where [M] is the concentration of free monomer and [M_0] concentration of monomer in equilibrium with a bulk surface this parameter increases exponentially with the exponential conversion of precursors. In the heat up method monomers are generated gradually during the heating and this is the main difference from hot injection where precursors act directly as monomers since their transformation is fast.

2→Nucleation

The nucleation process occurs when [M] become higher than the critical nucleation concentration and therefore the solution is supersaturated and temperature reach its critical value. During nucleation stage the nucleation rate (d[N]/dt where [N] is the nuclei concentration) grows from an infinitesimal value to a maximum. The concentration of nuclei increases significantly. As can be seen in Figure 4 nuclei grow little

above the monomer size and a polydisperse distribution is obtained, due to the presence of new formed and growing nuclei.

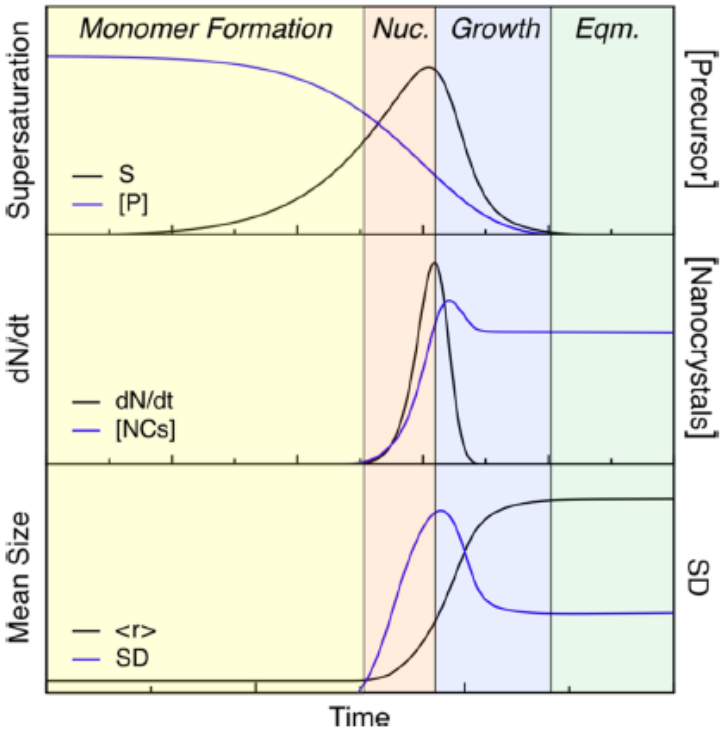

Figure 4parameters evolution during a typical heat up synthesis. In the first graph the precursor concentration [P] and the supersaturation S are plotted against time, the second graph is the representation the nucleation rate (dN/dt) and the concentration of nucleous[NCs] development over time and the third one shows the trend of nanocrystal radius <r> and standard deviation SD of size distribution. (Van Embden, Chesman, and Jasieniak 2015)

3→Growth

This stage's start is characterized by the decline of nucleation rate. Once nuclei are produced they grow by incorporation of monomer into the crystal bulk. Monomers reach the nuclei surface via diffusion. Hence, monomers concentration decreases and once its value would be below the critical concentration the nucleation will stop. In this stage the standard deviation SD of size distribution decrease since when [M] <[M_{rc}] the particles with r<rc dissolved back into solution and the average size of nanocrystals reach its maximum.

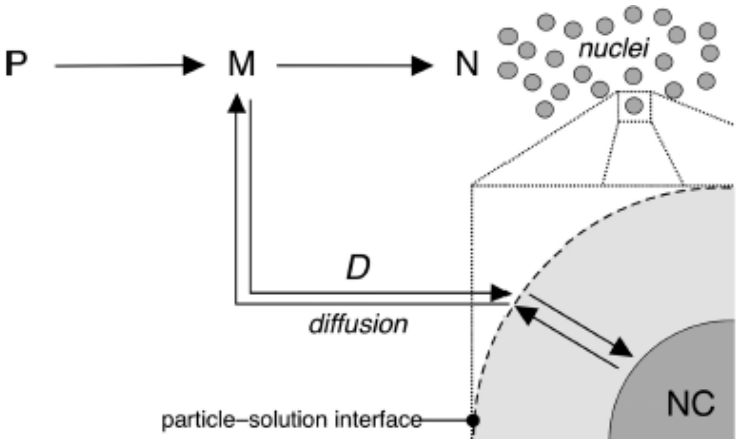

Figure 5 illustration of the four stages occurring in the formation of nanocrystal(Van Embden, Chesman, and Jasieniak 2015)

In heat up synthesis nucleation and growth occur for similar period of time, in contrast to what happen in hot injection synthesis. This is due to the prolonged conversion of precursor into monomers during the heating that sustains [M] above the critical value for a long period before the number of nuclei is high enough to cause a significant decrease of [M] for their growth. The growth of existing nuclei by monomer addition, called heterogeneous nucleation, has a lower energy barrier than the formation of a new phase (high energy

demanding) from monomers (homogeneous nucleation). Hence, nucleation can occur simultaneously with a fast growth. For this reason, when there is no separation in time between nucleation and growth it is difficult to obtain monodisperse distribution. In heat up synthesis the most important reaction parameters that allow to balance nucleation and growth are the heating rate and type of precursors used.

- ➔ Heating rate

Since it is the heating that induces the conversion of precursors to monomers, the heating rate corresponds to the monomer generation rate.

Slow heating rates cause slow conversion of precursor to monomer and therefore the nucleation is delayed. When nuclei are formed and start to growth the production of monomers from precursors is slower that monomers consumption and therefore the net decrease of monomers concentration stops the nucleation. The growth can continue with the remaining monomers.

For rapid heating rates the production of monomer is faster than the growth of existing nuclei and therefore the available monomers contributes almost only to nucleation. This provide a higher number of nuclei and therefore the final average size is reduced with a narrow size distribution. Indeed, it is the nucleation tuning that allow monodispersity; nucleation tuning occurs when during the nucleation event $<r_c>$ the size of the nucleated nanocrystals remains similar to the mean of particles size distribution.

- ➔ Precursors

Ligands and coordinating solvents present in the reaction environment define precursors. The kind of precursors formed influence their reactivity and so their transformation into monomers. The ideal precursors are stable at low temperatures and show rapid reaction or thermal decomposition upon a certain (elevated) temperature in order to obtain a uniform and short nucleation event.

For highly reactive precursors the conversion into monomers is fast and it can occur also at room temperature. Hence, supersaturation is reached early and therefore nucleation starts at low temperature. Due to the high availability of monomers high rate nucleation and growth occur simultaneously. With the growth of nuclei monomers concentration drops holding up the nucleation. This results in a low nanocrystal concentration and polydispersity.

Moderate reactive precursors are converted into monomers with a balance rate during heating. During the heating stage the supersaturation gradually increases but the availability of monomer is not enough high to sustain growth during nucleation stage. With moderate reactive precursors is possible to obtain monodisperse nanocrystal in a good yield.

Low reactive precursors convert into monomers only at high temperature and the conversion occurs with a slow rate, therefore the nucleation is delayed and extended for a long period. The equilibrium condition between clusters formation and dissolution lasts until the supersaturation reach the level that allows the clusters larger than the critical radius to growth. Growth causes monomers concentration to drop and therefore the critical size increases preventing the remaining clusters to growth. The biggest crystals can growth with monomers in solution and for Ostwald Ripening. This Ostwald Ripening leads to a poor yield of large nanocrystals with broad size distribution.

Copper sulphides

The copper sulphide system $Cu_{2-x}S$ has many different possible stoichiometric compositions ranging between a ratio Cu: S 1: 2 and all the following compositions are possible:

Table 1 $Cu_{2-x}S$ phases

name	formula
villamaninite	CuS_2

covellite	CuS
yarrowite	$Cu_{1.12}S$
spionkopite	$Cu_{1.39}S$
geerite	$Cu_{1.6}S$
anilite	$Cu_{1.75}S$
digenite	$Cu_{1.8}S$
djurleite	$Cu_{1.96}S$

Copper sulphide materials are p-type semiconductors thanks to copper vacancies in their lattices and each different composition has distinct free carrier density. The top of valence band in copper sulphides is characterized by a strong contribution of p orbital of S, while the bottom of the conduction band is dominated by the contribution of Cu 4s and 4p orbitals. It can be assumed that the bonding in copper sulphides is created by one copper 4s electron and p electrons of S. By varying stoichiometries the band gap can be tuned (Figure 6).

As reported in literature[5], the valence band of a fully stoichiometric compound Cu_2E (E = chalcogenide), is completely filled and the material behaves like an intrinsic semiconductor. A hole can be crated in the top of the valence band by removing a copper atom from lattice.

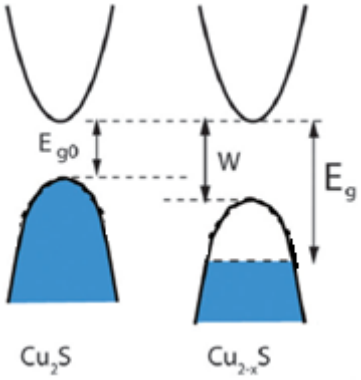

Figure 6: band structures of plasmonic copper sulphides nanocrystals. W is the intrinsic bandgap, Eg is the optical band gap. (Comin and Manna 2014)

As can be seen in Figure 6 copper sulphides materials are degenerate p doped semiconductors having the Fermi level in the valence band. A degenerate semiconductor has the carrier density higher than 10^{19} cm^{-3}. The carrier density of $Cu_{2-x}S$ varies from 10^{18} cm^{-3} for stoichiometric compound to 10^{22} cm^{-3} for non-stoichiometric compounds (C. Beynis 2014) and therefore the latter are degenerate semiconductors (Zeni).

The difference between the bottom of the conduction band and the highest occupied state in the valence band is the optical band gap, since it corresponds to the photon energy needed to promote an electronic transition. In degenerate p doped semiconductor, optical band gap depends on the concentration of free carriers and this dependence is called Burstein-Moss effect. The optical band gap increases with an increased number of vacancies since they occupy the upper part of the valence band thus lowering the Fermi level's energy.

Table 2: values of energy band gap for different copper sulphide materials. The energy grows if x increases.

	X value	Energy of band gap
Chalcocite (Cu_2S)	0	1.2 eV
Digenite ($Cu_{1.8}S$)	0.2	1.5eV
Covellite (CuS)	1	2.0eV

Since the valence band is created with a predominant contribution of the chalcogen orbitals, if a hole is created in this band the chalcogen valence will be mainly influenced. Considering that in Cu_2S compounds

the valence of S is -2 while copper's valence is +1 in the sub-stoichiometric compounds since the valence of copper is still +1 the chalcogen has a valence higher than -2. This is reflected in the structures of sub-stoichiometric compounds where the S_2 pairs are present.
For the copper sulphides system mineral covellite CuS is a particular case. In covellite crystalline phase sulphur is present as both S_2^{2-} and S^{2-}. With regard to valence of copper, instead, it is not yet clear which it is the oxidation state since some studies report that it should be +1, as $(Cu^{1+})_3(S_2^{2-})(S^{1-})$ or $(Cu^{1+})_3\ (S_2^{-})(S^{2-})$, while others claim that bot Cu+1 and +2 are present as $(Cu^{2+})(S_2^{2-})(Cu^{1+})_2(S^{2-})$ others claim that copper ions bind tetrahedrally and trigonally to sulfur ions such as in total $[(Cu)_2]^{3+}$ and Cu^{+} to S_2^{2-} and S^{2-} , whereas S–S bonds are covalent (Lesyuk et al. 2018). Based on calculations the valence of Cu has been set between 1 and 1.5 (Comin and Manna 2014)(Xie, Riedinger, et al. 2013).
The structure of covellite is hexagonal, (space group $P6_3/mmc$, a=3.79 A and c=16.34 A, Z=6). It is formed by triangular CuS_3 (green in Figure 7) units sandwiched between two layers of tetrahedral CuS4 (blue Figure 7). Disulphide bonds link each triple layer to a bottom and a top triple layer, along c axis. Basing on the fact that covellite has an anisotropic conductivity this material can be described as a collection of 2d metal sheets staked perpendicular to the c-axis.

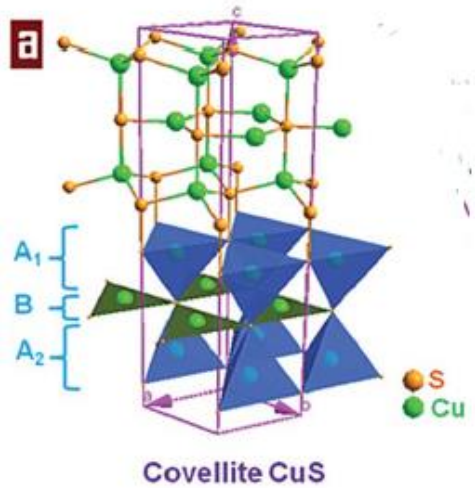

Figure 7: Model representing covellite structure (Rui, Tan, and Yan 2014)

Covellite strong p-type metallic behaviour confirms the highest concentration of free carriers among all the copper sulphide materials.

LSPR in copper sulphides $Cu_{2-x}S$ system

The NIR absorption of $Cu_{2-x}S$ system has been proved (Zhao et al. 2009) to be due to LSPR of free holes in these materials.

Stoichiometry-dependence

The carrier i.e. hole density increases with the increase of x. Plasma frequency depends on the carrier density and increases with this parameter. With a higher plasma frequency, the λ of LSPR decrease and therefore the LSPR moves to higher frequency when x increases (blue shift). An increase in the hole density is also accompanied by an directly proportional increase in the LSPR peak intensity (Faucheaux, Stanton, and Jain 2014).
The carrier concentration for $Cu_{2-x}S$ system sets the LSPR energy which is in the NIR range.

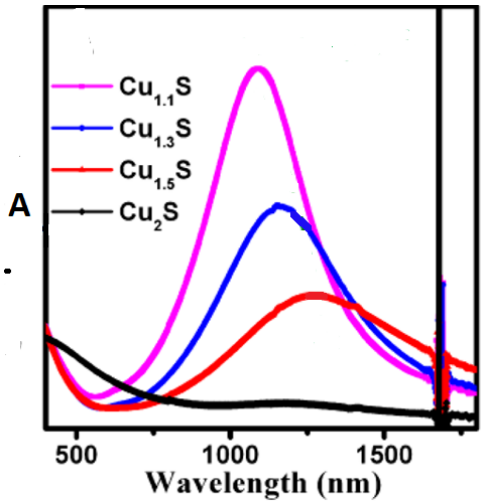

Figure 8:NIR spectra of $Cu_{2-x}S$ (Xie, Carbone, et al. 2013)

If the $Cu_{2-x}S$ nanoparticles are a mixture of different stoichiometry and crystalline phases their LSPR peak is broadened since is composed by the contribution due to all the different materials.

Surrounding medium

As expected by the Frolich condition the LSPR band position is affected by the dielectric constant of the surrounding medium ε_m and hence by its refractive index (n) which is proportional to the square root of ε[2].

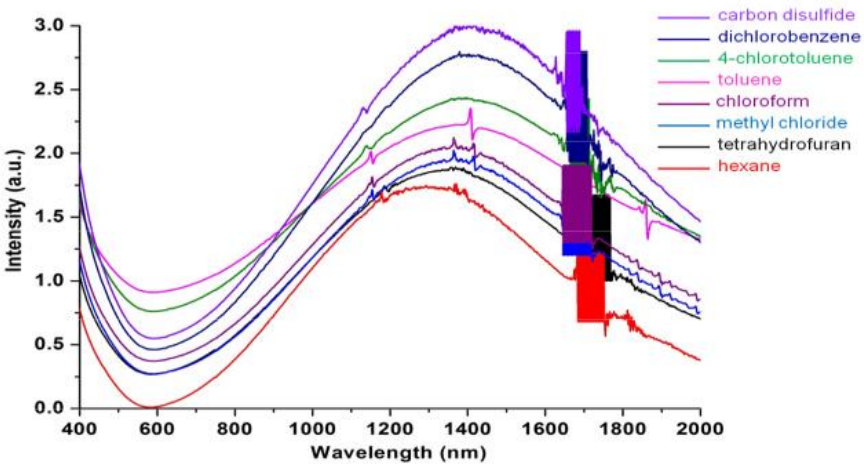

Figure 9: absorption spectra for $Cu_{2-x}S$ nanocrystal in different organic solvent

[2] Refractive index (n) is proportional to the square root of dielectric constant since it can be calculated as $n = (\mu\varepsilon)^{1/2}$ where μ is magnetic permeability

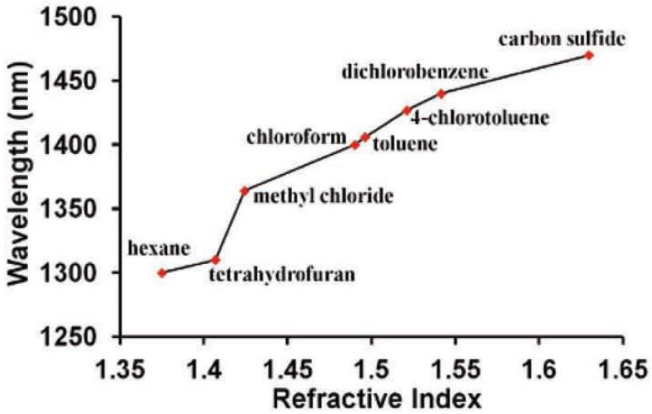

Figure 10:LSPR wavelength versus refractive index of the solvent. As can be seen if the refractive index increases the same is done by λ. (X. Liu et al. 2013)

Furthermore, solvent can influence LSPR also by their adsorption on $Cu_{2-x}S$ nanocrystal. Example of this kind of influence is given by oleic acid, that coordinates through the surface using the deprotonated carboxyl functional group, and, in a less aggressive way, by oleylamine that uses the amino group for surface coordination. Both carboxyl and amino groups can trap vacancies in the surface, the first through its negative charge and the latter with its lone pair electrons, causing an increment of the LSPR wavelength. Hence, beside the role of the solvents or ligands refractive index on the LSPR position also the electron withdrawing abilities of these molecules has to be taken into account. Furthermore, not only the type of anchoring group plays a role on the LSPR position but also the reorganization of the surface ligand arrangement on the nanocrystal surface.

A plasmonic nanoparticle LSPR can be influence by the neighbouring environment which surrounds it within a distance of 1/5 of its diameter (Faucheaux, Stanton, and Jain 2014). Hence, the environment that is experienced by a small nanocrystal is the ligand environment and in that case the modification of the LSPR due to solvent change is very small.

Since LSPR of $Cu_{2-x}S$ nanocrystals lies in the IR region ligand and solvent may show vibrational overtones. In that case, the dielectric term of ligands and solvent has to be considered as frequency dependent and LSPR spectra perturbation is expected.

Size

Many parameters which influence the LSPR are size dependent:

- When the nanocrystal size becomes smaller than the free path length the surface scattering of the carriers increases, and it causes a broadening and a slight red shift of LSPR band
- The quantum size effects cause the confinement of carriers which results in a significant modification of the dielectric function and a blue shift of the LSPR. This phenomenon is shown by nanocrystals with dimensions comparable to the De Broglie wavelength of free carriers in the material. For semiconductors the quantum size effects are operative in the ~5nm range.
- Nanocrystals with different size can have different free carrier concentration
- Effective masses of carriers can change with size
  (Faucheaux, Stanton, and Jain 2014)

The blue-shift of the LSPR peak with the increase of the diameter of spherical particles in the 5 nm range has been reported by (Zhu et al. 2015a).

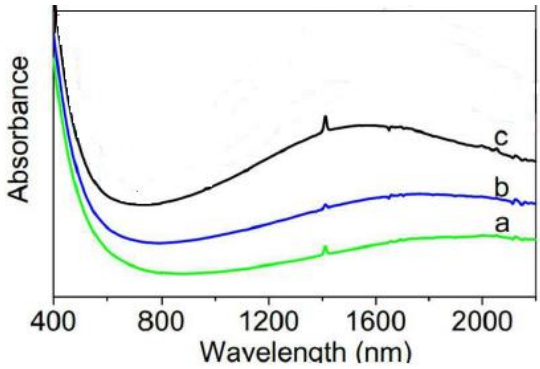

Figure 11: NIR LSPR absorption of spherical djurleite nanocrystals with size of a) 4.1 ± 0.3 nm b) 5.3 ∓0.5 nm c) 6.7 ± 0.6 nm (Zhu et al. 2015a)

Shape

Anisotropic nanocrystals are expected to show separate LSPR modes for each unique axis.
The complete comprehension of the shape dependence of LSPR spectral positions and intensities has not yet been achieved. Indeed, copper sulphide nanocrystals with anisotropic morphologies exhibit LSPR in a spectral range more limited than expected and often some LSPR modes can be overlooked (Xie, Carbone, et al. 2013)but however there are some exceptions. Chalcocite to digenite nanodisks are some of these exceptions and show two LSPR absorption peaks due to the in-plane and out-of-plane modes.

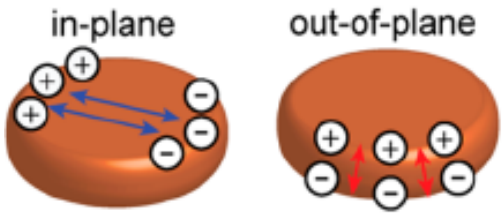

Figure 12: two expected LSPR for nanodisk; in plane LSPR that occur when the illumination wave is polarized parallel to disk and out of plane when it is normal to the disk.

Interactions between particles

If particles are close together, such as when they aggregate, their LSPR can couple. Hence, LSPR peak can shift quite considerably for interparticle coupling. This effect has been used to tune the LSPR of particles that can form assemblies such as copper sulphide nanodisks. Nanodisks are able to form close-packed superlattices.

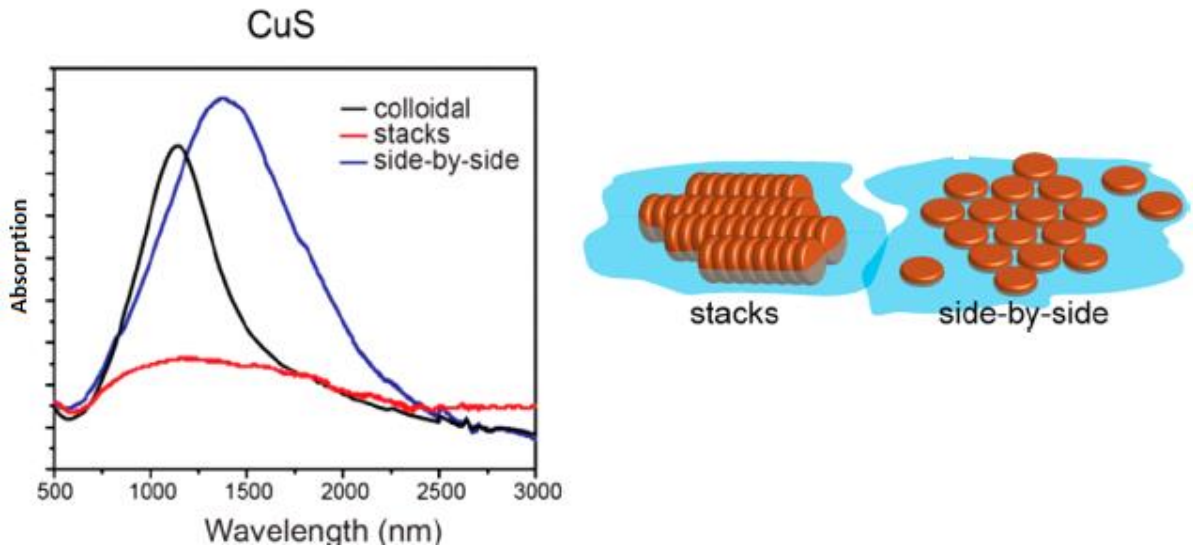

Figure 13: NIR absorption spectra of colloidal solution of and films of covellite nanodisks. Nanodisks can form films orienting in two different ways side by side and staked.(Hsu, Ngo, and Tao 2014)

Uses and challenges

Copper sulphide system nanocrystals are particularly useful thanks to their LSPR tunability. Hence, for $Cu_{2-x}S$ nanostructures, the carrier concentration can be modified via in situ post synthesis,thus changing the LSPR spectrum. Post synthesis processes that allow the changing of carrier density are redox reactions or electrochemical processes. In this way, an on/off switching of LSPR can be obtained; in an oxidizing environment the LSPR is favourited by the creation of vacancies, conversely, in a reducing environment the vacancies are filled and the LSPR is turned off. The possibility to obtain a on off LSPR offers wide opportunities to apply these materials in the field of photonics. Thanks to the cuprus sulphide high sensitivity to redox reaction and electrochemistry processes these materials can be used also as analytical devices using LSPR as a probe.

The characteristic structure of $Cu_{2-x}S$ materials make them suitable to cation exchange and that may be useful for sequestering of toxic metal ions in solution. Covellite is the most suitable material, for this purpose, since the incorporation of and extra ion in its crystalline structure is not accompanied by the expulsion of Cu(I) as it happens for other $Cu_{2-x}S$.

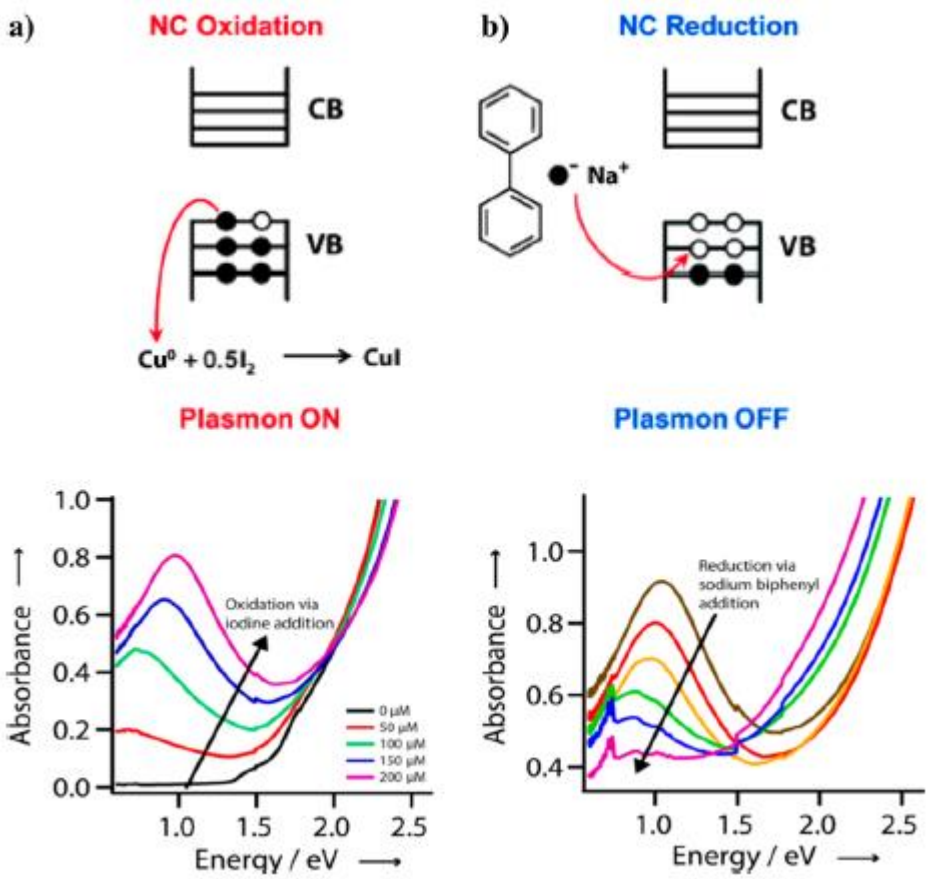

Figure 14: on off control of LSPR in Cu2-xS system. Above the schematic illustration of holes formation and filling, below the change of the absorption spectra in an oxidizing or reducing environment. The oxidizing environment is due to iodine while the reducing to sodium biphenyl. (Faucheaux, Stanton, and Jain 2014)

Thanks to $Cu_{2-x}S$ nanocrystals marked NIR absorption, low cytotoxicity and low cost these materials can be used ad photothermal agents in photothermal therapy. Photothermal therapy is a technique for cancer treatment in which temperature is locally raise to the 42-48°C range in cancer cells. The increment of temperature inside a cell causes its death. The increment of temperature is due to the conversion of light to

heat carried out by the photothermal agent. In photothermal therapy the photothermal agent is accumulated at the tumour site as well the irradiation which is focused only in this area and therefore the cytotoxic effect is limited to the ill tissue. The NIR (λ=700-1100) radiation is preferable to visible light because its potential for deep penetration in biological tissue and therefore sub cutaneous tumours can be treated.

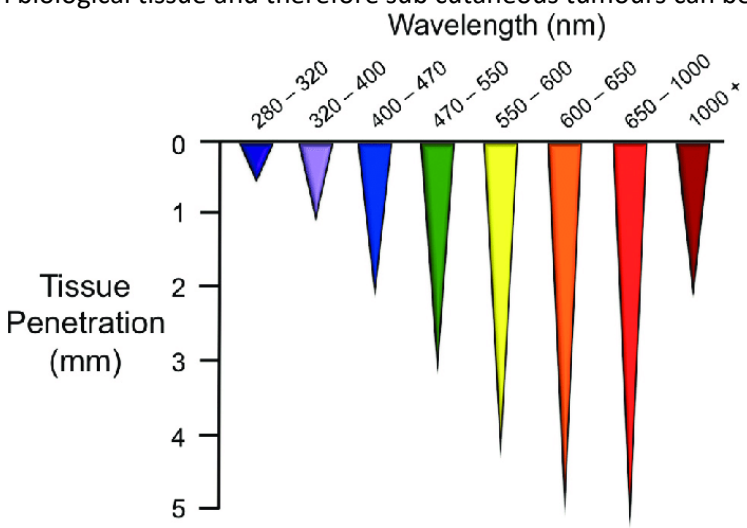

Figure 15: schematic representation of penetration depth of light into skin tissue (Ruggiero et al. 2016)

$Cu_{2-x}S$ are suitable photothermal agent since they absorb NIR radiation thanks to LSPR and release the energy as heat in the de-excitation through non-radiative process[3]. $Cu_{2-x}S$ nanocrystals have the advantage of being low cost materials, of absorbing light over a broad NIR spectral range, of being stable under optical excitation and therefore are more suitable photothermal agents than gold nanoparticle that have been already widely studied. Since covellite has the strongest LSPR than the other kinds of copper sulphides, it has also an high heat conversion efficiency that is the ratio between the energy converted in heat by the particle, and the incoming radiative energy (Marin et al. 2018).

In conclusion, thanks to the possible variations in composition, morphologies and valence states and to their low cost and lack of toxicity $Cu_{2-x}S$ materials can be applied in in a wide range of fields such as photocatalysis, optoelectronic devices, sensors, bio-imaging and photothermal therapy.

Over the years a whole host of possible synthesis of copper sulphide nanoparticles with different shape, size and stoichiometric rate between Cu and S have been reported in literature, such as topochemical reaction, aqueous colloidal capping method, hydrothermal method, hot injection and heat up methods. The morphologies of $Cu_{2-x}S$ nanostructures reported in literature (Zhao et al. 2009) are nanofibers, nanotubes, nanowalls, nanaocages, flowerlike nanoparticles, hollow spheres, nanorods and nanowhiskers.

The fact that copper sulphide system is widely tuneable makes these materials interesting but on the other hand their tuning can be difficult in the control of composition and impurities and in some cases there can be critical reaction conditions. Indeed, copper sulphide system has a rich phase diagrams with narrow structural domains and therefore stoichiometric ratio and environmental conditions have to be strictly controlled during their synthesis to obtain a pure crystalline phase and material composition. Copper sulphides are really sensitive to mild changes in reaction conditions which is why they are often obtained as a mixture of compositions and crystalline phases rendering their characterization extremely difficult (uncertain composition)(Zhao et al. 2009). Pure covellite nanocrystals are particularly hard to obtain since their thermodynamic stability domain is narrower with respect the other crystalline phases and, for this reason, the most restrictive reaction conditions are required.

[3] Heat is produced by conversion of the LSPR energy through scattering with electrons and phonons that happens within several hundreds of femtoseconds. This results in an efficient heating of the nanoparticle which can release the heat in the surrounding environment.

If the stoichiometric ratio is different from the desired one the behaviour of the obtained material is different too because it would have a different carrier density.

Aim of the thesis

The aim of this thesis work is to establish reproducible synthetic protocols for producing copper sulphides nanoparticles which can be used as photothermal mediators. The protocols used to produce anisotropic particles are heat up synthesis whit the aim of developing synthetic path which can be scaled up, while to establish sustainable synthesis route for mainly oval shaped particles green approaches are used. The reaction parameters affecting the NPs morphology, size, phase, size distributions and tendency to assembly are indagate in order to achieve their control.
In order to have a particles set available for further studies on heat conversion efficiency the particles have been fully characterized.

Experimental part

Characterization

Scanning Electron Microscopy (SEM)

Information on the sample is obtained by its interaction with an electron beam that generates signals in the form of secondary electrons, back scattered electrons and X-rays. Secondary electrons are due to inelastic interactions between the primary electron beam and the sample, these electrons are very beneficial for the inspection of the topography of the sample's surface. Backscattered-electrons (BSE) are due to elastic collisions of electrons with atoms. The higher is the atomic number of the atom the higher will be the scattering and hence a higher number of electrons are collected by the detector. When the electron beam strikes the surface of a sample it causes the emission of X-ray photons. Energy Dispersive X-ray Spectroscopy (EDS) uses this emitted X-rays to obtain a localized chemical composition through the analysis of their energy (CFAMM 2017; Phenom-World BV 2017; Joshi, Bhattacharyya, and Ali 2008).

The measures were performed with a ZEISS-Sigma VP FE-SEM

Sample preparation: the specimen is deposited on a sample holder (stub). First of all, the stub has to be properly cleaned, this can be done in an ultrasonic bath with acetone as solvent (two cycles of 15 minutes each). A double-sided conductive tape is used to mount a silicon wafer on the stub. Copper sulphide nanoparticles purified (described for each particle in their respective paragraph) solutions is then dropped onto the silicon wafer.

Transmission Electron Microscopy (TEM)

In this case an electron beam passes through the sample and an image is formed from the transmitted electrons that have interacted with the sample. Interactions between the atoms and the electrons allow to observe sample characteristics such as crystal structure but also its defects, for example in the High Resolution TEM (HRTEM) mode. TEM allows to perform chemical analysis of the sample by EDX(Joshi, Bhattacharyya, and Ali 2008)

The measures were performed with a JEM3010, Jeol microscope.

Sample preparation: $Cu_{2-x}S$ purified solutions have been dropped to TEM grids (holey carbon film on nickel grid) placed above optical paper, and then it has been left to dry.

X Ray Diffraction (XRD)

X-ray diffraction (XRD) is a widely used technique for the study of properties of solids. A X ray beam striking the sample, it is diffracted following the Bragg law:

$$sin\theta = \frac{n\lambda}{2d_{hkl}}$$

Where n is an integer, dhkl is the distance between crystalline planes with Miller indices (hkl) in the crystal, λ is the wavelength of the incident X ray beam and θ is its angle of incidence. The XRD spectra reported the intensities of the diffracted X ray beams as a function of the angle.

The equation of Debye-Scherrer allows to determine the grain dimension of crystallite

$$d = \frac{K\lambda}{b\ cos\theta}$$

Where b is the full width at half maximum of the peak, θ is the angle of incidence, λ is the wavelength of the incident X ray beam (1.54069 A) and K is about 0.9.

The measures were performed with Philips XPert diffractometer and D8 Advance Bruker diffractometer both with a Cu radiation.

Sample preparation: solution of $Cu_{2-x}S$ nanoparticles (purified or not purified as described for each particle in their respective paragraph) were deposited to a zero-background holder by subsequent drops deposition until a good coverage of the holder was obtained.

FT-IR Spectroscopy

IR spectra of $Cu_{2-x}S$ nanoparticles have been acquired to indagate their organic layer. From IR spectra it is possible to establish which molecules are present in the organic layer and which of their possible chemical groups bond the $Cu_{2-x}S$ surface.

IR measurements were performed with Nexus FT-IR

UV-VIS-NIR Spectroscopy

The UV-VIS-NIR Spectroscopy has been used to indagate the LSPR of the $Cu_{2-x}S$ nanoparticles.

UV-VIS-NIR spectra were obtained with Perkin Elmer Lambda 750.

DLS analysis

The size of the suspended particles was measured using the DLS (dynamic light scattering) technique.
The DLS technique is based on the scattering undergone by a laser beam that invests a colloidal suspension, in which the particle size is sub-micrometric (with the instrument particle size from 0.6 nm to 6 µm can be measured). DLS is based on the assumption that every particle is subjected to Brownian motions, and when it is invested by the laser light the scattering phenomenon occurs. Particles motion speed is related to their size, so the particles that have a fast motion will have smaller dimensions than others that move more slowly. The diffused light intensity has a fluctuation frequency which depends on particles diffusion (in solution) speed which in turn depends on their size. Thus, particle size can be extrapolated by the analysis of the fluctuations of the diffused light intensity.
The laser light that invests the sample, is diffused by the particles in all directions and detected only in the direction where the detector is positioned. The light intensity fluctuations are converted into electrical signals and these into dimensions data.
The instrument measures the hydrodynamic diameter of the nanoparticles, ie the diameter of the moving kinetic unit, comprising the coordination sphere and any species adsorbed on the surface (for example polymers or surfactants).
From the measurement a particle size distribution curve, a mean diameter value, and an index that provides information on the polydispersion degree (PDI) of the suspension are obtained. This index is between 0 and 1, the closer it is to 0 the more the suspension is monodispersed, instead for indices equal to 1 the suspensions are considered totally polydisperse. In general, a suspension can be considered monodisperse for values of PDI ≤ 0.2, average polydisperse for $0.2 \leq$ PDI ≤ 0.5 and polydisperse for values higher than 0.6.
The particle size distribution curve is based on the scattering intensity. Moreover, from the results obtained it is possible to derive two different types of calculated distributions: the first provides the distribution with respect to the volume occupied by the particles while the second with respect to the number. To obtain the calculate distributions the refractive indices of the particles, the absorption of the solution and the solvent viscosity have to be set on the instrument.

To perform the analysis the solution has been diluted.

DLS analysis have been performed with Malvern Zetasizer nano series.

Chemicals

- Cetyltrimethylammonium bromide (CTAB, Sigma, 98%, 364.45 g/mol)
- Milli-Q Water
- Sodium Sulphide nonahydrate (Na2S $9H_2O$, Sigma,240.18 g/mol)
- Copper(II) chloride dihydrate ($CuCl_2$ $2H_2O$, Sigma, 99%,170.48 g/mol)
- Sodium citrate dihydrate ($Na_3C_6H_5O_7$ $2H_2O$,Sigma 99%,294.10 g/mol)
- Oleylamine (C18H35NH2 ,Sigma,70%,267.49 g/mol)
- 1-Octadecene ($C_{18}H_{36}$,Sigma, 85%, 252.48 g/mol)
- Copper(I) Chloride (CuCl, Sigma, 99.99%, 99g/mol)
- Poly(acrilic acid) (Sigma,molecular weigth 450 000)

Nanodisks

The term nanodisk is referred to a nanocrystal with two-dimensional disk-like shape.

In this work $Cu_{2-x}S$ nanodisks have been obtained through heat up method. Based on the concepts of this method a copper and a sulphur precursors are formed during the synthesis steps. As a source of copper, CuCl and $CuCl_2$ have been used while sulphur powder has been used for obtaining the sulphur precursor. Solvents used for the synthesis are oleylammine OLAM and 1-octadecene ODE.

Heat up nanodisks synthesis

Copper precursor

The interaction between copper and ligands can be evaluated with the hard and soft acid and base (HSAB) principle[4]. Hard metals associate more strongly with hard ligand than with a soft one and vice versa for soft metals.

	Character
Cu (II)	borderline
Cu(I)	soft
OLAM	hard
Cl	hard
ODE	soft
Sulphur ligands	soft

Since Cu(II) and Cu(I) have different HSAB character their interactions with the possible ligands present in solution have different strengths. This influence the precursors reactivity and therefore the rate with which they convert into monomers. Hence, the nucleation process which depends on the monomers concentration, is also influenced by the HSAB character of the precursors. During the growth stage the strength of the copper-ligand bond influences the ligand coordination on the surface of nuclei. The ligand coordination on the nuclei surface is essential to form a stabilizing monolayer. This monolayer prevents the uncontrolled growth and aggregation. Furthermore, the monolayer influences the anisotropic development into disk shape. The bond between ligands and nuclei surface has to be labile enough to allow the permeation of monomers from solution to the growing surface. Moreover, the affinity between ligands and metal influences the final composition of the nanodisk.

Based on what is reported in literature (Xie, Carbone, et al. 2013), in the mixture of OLAM, ODE CuCl is present as neutral complex of Cu(I) whit all the others components of the mixture as ligands $Cu_x(OLAM)_y(ODE)_zCl_x$ with stoichiometry dependent on reaction composition. OLAM coordinates the metallic ion through its amino group while ODE coordinates through the electronic clouds double bound. The same is expected for Cu(II).

Sulfur precursor

As widely reported in literature (He et al. 2018)(Xie, Carbone, et al. 2013)(Xie, Riedinger, et al. 2013)(Wolf, Kodanek, and Dorfs 2015) sulphur precursor is often prepared with OLAM (or other alkylamines) and sulphur powder which exists as S_8 rings in its standard state. As reported by (Thomson et al. 2011) in OLAM sulphur rings opens to form oleylammonium polysulphides. When the sulphur precursor is heated for the crystals' growth the excess of OLAM reacts with the polysulfides and generate H_2S, as shown in Figure 16. Further formation of H_2S is due to the by-products of the initial reaction. H_2S likely exists as oleylammonium hydrosulfide due to partial neutralization with OLAM. Hence, in situ oleylammonium hydrosulfide is the specie that reacts with metallic ion in the metal complex and forms CuS nanocrystals. The kinetic of copper

[4] This principle considers the interaction between metals (Lewis acids) and ligands (Lewis bases) basing on the concept of hard and soft character. An acid or a base is defined as hard if it is weakly polarizable and vice versa it is defined soft if it is highly polarizable.

sulphide nanocrystals formation is slower using sulphur powder in OLAM with respect to other possible precursors such as the ones phosphine-based. This slow reaction rate can be useful for obtaining nanocrystals with specific structures and also it is a way to avoid the formation of very small nanocrystals; very small size nanocrystals can be produced by using more reactive sulphur precursor that produces a larger number of nuclei. Furthermore, the reaction by-products of the reaction in the sulphur production, like amidines[5], can act as stabilizing ligand during the nanocrystals synthesis and help in the formation of anisotropic structures.
.

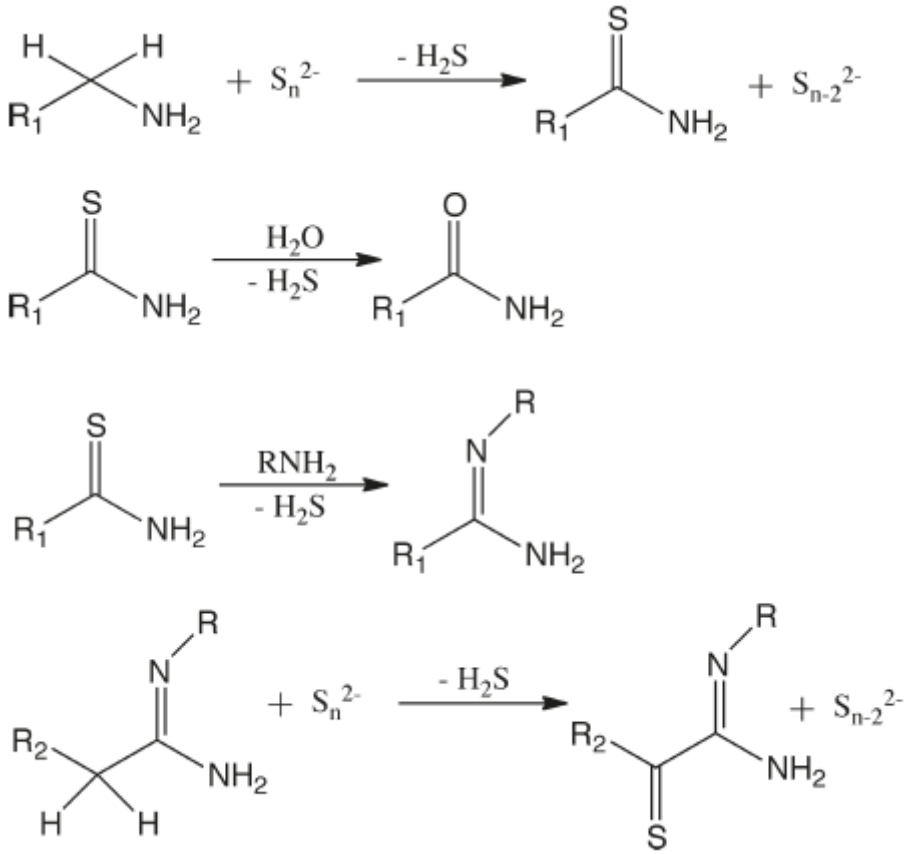

Figure 16: Reaction pathways of sulfur precursor in OLAM heated to 130°C. R=$C_{17}H_{33}$, R1=$C_{16}H_{31}$, R2= $C_{15}H_{29}$. the oleylamonium polysulphides react with the excess of OLAM producing hydrogen sulphide. (Thomson et al. 2011)

Sulphur can react also with ODE thanks to its alkene group whose oxidation can be thermally activated by sulphur. This oxidation produces H_2S and 2-Tetradecylthiophene.

[5] The reaction that leads to the production of amidines may occur at lower temperature in presence of Lewis acid such as Cu(I).

Growth

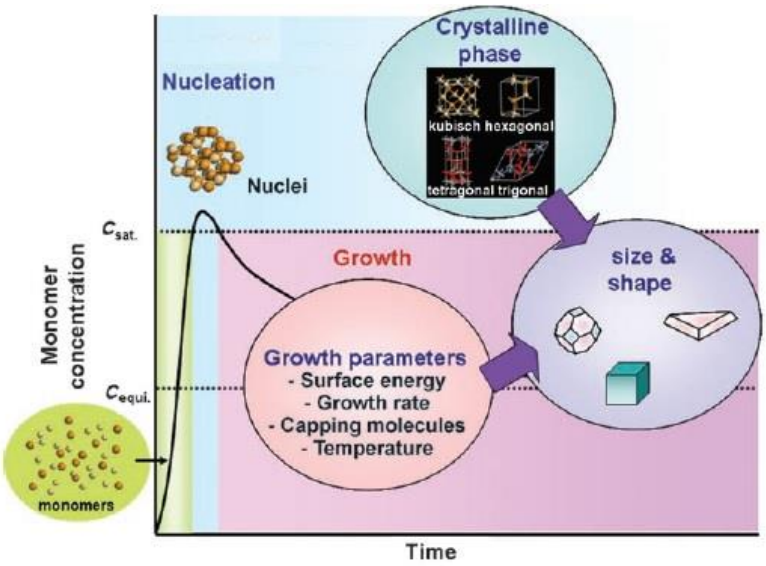

Figure 17: Illustration of nanocrystals formation steps (Jun, Choi, and Cheon 2006)

As can be seen in Figure 17, nucleation is an important step since during it the phase is formed but is the growth of embryos which allows to obtain nanocrystals with disk-like shape. This is possible thanks to an intrinsic propensity of hexagonal covellite to develop anisotropically along or perpendicular to c axis (Xie, Carbone, et al. 2013). Hence, for the 2D growth, the lateral growth directions are perpendicular to the c-axis of the hexagonal crystal, and the preferable cleavage plane[6] would be the one containing the S–Cu bonds(Lesyuk et al. 2018). This is due to difference among surfaces energy since the growth rate is exponentially correlated to the surface energy. The anisotropic growth is further promoted by OLAM thanks to the stabilization of the (001) face by its selective adhesion that goes to accentuate the growth rate difference between different direction.(Lesyuk et al. 2018; Jun, Choi, and Cheon 2006). The selective stabilization of OLAM of (001) face has been widely report in literature for different reaction conditions (Zhang et al. 2008; M. Liu et al. 2015; Xie, Carbone, et al. 2013).

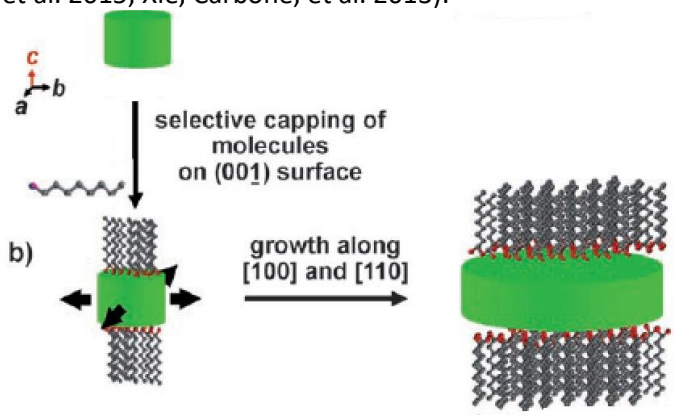

Figure 18:anisotropic growth promoted by surface selective surfactant

Further information will be given in the following paragraph “TEM and SEM”.

[6] A crystal tends to break along specific flat planar surfaces called cleavage planes. A cleavage plane is a 2D surface characterized by the weaker bonds between atoms in the crystal lattice.

Organic shell

The nanocrystals obtained have a organic primary shell of OLAM directly bounded to the nanodisk, this has been proved by the analysis of FT-IR spectra. This confirms OLAM influence on the nanocrystal growth as already reported. ODE is a non-coordinating ligand for $Cu_{2-x}S$ nanocrystals and therefore it can be present only in the outer part of the organic shell due to hydrophobic attraction with OLAM (Zhu et al. 2015a).

CuS nanodisk protocols

In this work two different protocols have been employed to obtain CuS nanodisks both via a surfactant-assisted nonaqueous route.

1) Heating-up synthesis. First of all, a clear yellow sulphur precursor (sulphur powder 1mmol) is prepared under vacuum in a three neck round bottom flask with 5 ml of OLAM and 5mL of ODE previously degassed at 130°C for 30 minutes. After the cooling to room temperature under nitrogen 0.5 mmol of CuCl or $CuCl_2$ are added to the solution which is then kept under stirring in vacuum for 1 hour and then heated up to 200°C (8°C/min); the solution was then maintained for 30 minutes at this temperature. The obtained green solution is rapidly cooled down to room temperature and then purified.

2) Heating up synthesis with sulphur precursor injection. Two solutions are separately prepared; a sulphur precursor solution (1 mmol of S powder) is prepared in 2 mL of oleylamine (OLAM) while in a three-neck round bottom flask the second solution is prepared with CuCl (0.5 mmol), 3 mL of OLAM and 5 mL of 1-octadecene (ODE) and maintained under inert atmosphere. The flask is heated up to 130°C for 30 minutes in order to obtain a clear yellow solution and then cooled down to 100°C in inert atmosphere. The sulphur precursor is now quickly injected in the flask followed by heating up to 180°C for 30 minutes (the solution has to become green). Finally, the solution is quickly cooled down to room temperature.

Both syntheses have been followed by a purification step: the dark green solution is washed 3 times with 5ml of ethanol and centrifuged at 3700rcf for 20 minutes. The resulting solution is finally dissolved in 3.5ml of toluene and centrifuged at 100rcf for 2 minutes to remove the larger particles.

The total amount of reagents and solvent are identical in both syntheses.

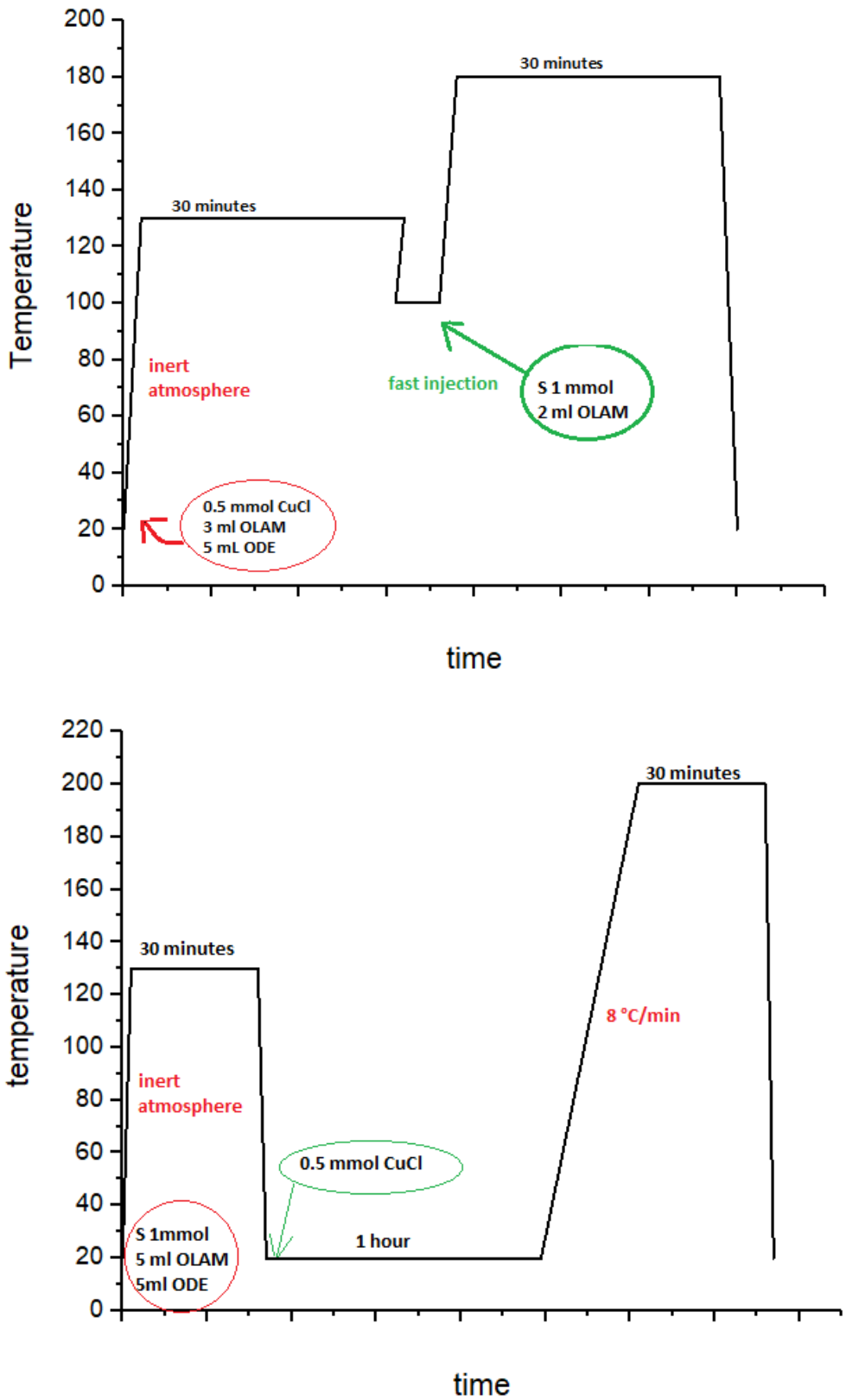

Figure 19: graphical illustration of the two synthetic approach for obtaining CuS nanodisks, above number 2 below number 1.

The first heating step is provided to solubilize sulphur (number 1) and $CuCl_1/CuCl_2$ (number 2) obtaining respectively sulphur and copper precursor. For sulphur precursor, based on what is reported in literature (Thomson et al. 2011) at 130°C the production of H_2S can occur but it can be assumed that this production is not completed and that a consistent part of sulphur is still present as oleylammonium polysulphides. In the

case of ODE the production of H_2S significantly occurs at higher temperature than OLAM (after 50 minutes at 200°C less than the 0.3% of sulphur is transformed)(McPhail and Weiss 2014). This hypothesis is sustained by the required step of controlled heating and by literature where the production of H_2S has been studied after 2h at 130°C.

After the addition of the second reagent the two protocols require different length of time of mixing to obtain a homogeneous solution before proceeding with the heating stage. In the second protocol the sulphur is added trough the injection of a solution and therefore the mixing is fast. This adding of a room temperature solution causes the temperature drop and, consequently in this case, the H_2S production occurs only during the heating stage. In the first protocol, for the addition of Cu(I)/(II) an hour of mixing is needed to solubilize the salt.

In the second protocol the copper precursor has to be a $Cu_x(OLAM)_y(ODE)_zCl_x$ complex produced at 130°C as reported in literature (Xie, Carbone, et al. 2013) characterized by a light yellow colour. The sulphur precursor added to copper precursor contains oleylammonium polysulphides. Cu(I) has a good affinity for sulphur ligands(Cotton and Wilkinson 1988). As reported in literature (Wilcox and Hirshkowitz 2015) copper sulphide complexes with N-donor ligands can be obtained with different copper nuclearities and sulphur oxidation levels based on the specific N-donor ligand, sulphur source, copper salt, and reaction conditions used. This copper affinity for sulphur ligands suggest that the addition of the sulphur precursor modifies the complex formed in the copper precursor solution changing its colour from yellow to black. When the sulphur precursor is added complexes with also sulphur ligands have to be formed in the solution.

Similarly, in the first protocol, after the copper salt addition at room temperature complexes with sulphur ligands have to be obtained in solution. Indeed, the solution colour gets black with the salt solubilization. In the case of this protocol also a fraction of oleylammonium polysulphides is probably already converted in oleylammonium hydrosulphide and therefore the complex obtained is different from the one obtained with the first protocol and the start of nucleation cannot be excluded. Furthermore, also the oxidation state of the copper has to strongly affect the nature of the complex since Cu(II) affinity for sulphur ligands is lower than Cu(I) and for non-chelating amines complex with Cu(I) are more stable than complex with Cu(II) (in aqueous solution) (Cotton and Wilkinson 1988). The diverse nature and reactivity of the complexes obtained in the different conditions are difficult to assess but they influence the shape, size and composition of the final products.

The colour of the solution turns from dark to dark green when covellite nanodisks are obtained while when the obtained nanodisks have a higher Cu content ($Cu_{2-x}S$ with $x<<1$) the colour of the solution is dark yellowish brown. The dark green colour is reported also as proof of the formation of nanocrystals in hot injection method (Xie, Carbone, et al. 2013) but in this case this colour is obtained just after the injection.

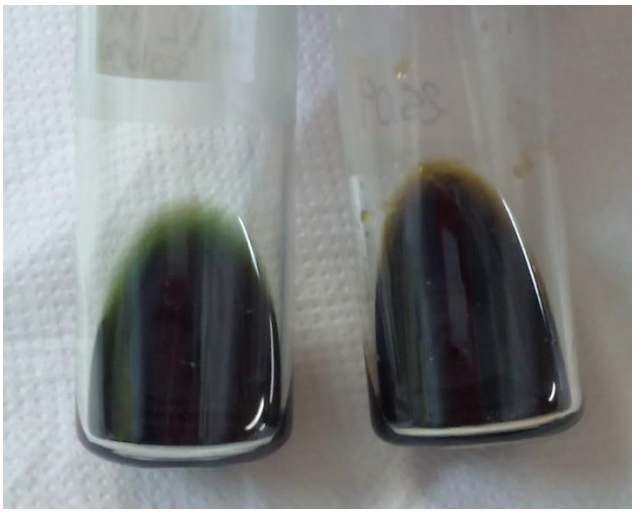

Figure 20: picture of covellite nanodisks solution on the left and $Cu_{2-x}S$ (with $x<<1$) nanodisks solution on the right

Materials

Sample name	Synthetic protocol	Copper oxidation state	Heating system
A	1	(I) CuCl	Oil bath
B	1	(I) CuCl	Oil bath
C	1	(II)$CuCl_2$	Heating mantle with (internal) thermocouple
D	2	(I) CuCl	Oil bath
E	1	(II) $CuCl_2$	Oil bath

Results and discussion

XRD

Sample A

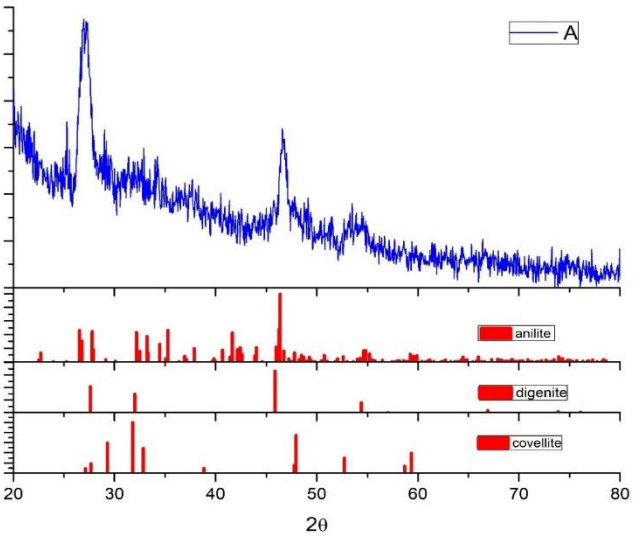

Figure 21: X-ray diffraction pattern of sample A and reference sticks of anilite, high syn digenite, hexagonal covellite

Figure 20 shows the diffraction pattern of sample A where two intense and sharp peaks at 27° and 46.7° are present, broader and weak peaks are visible at about 54°, 32°, there is also a shoulder at 29°. The peak at 27° may be attributed to digenite as also the one at 46.7° but the latter is well matched also by anilite. The peak at 54° may be attributed both to anilite and digenite but its large width may be a signal of a contribution of another phase, namely covellite, two broad peaks of covellite are visible at 47.7° and 47.9°.
In conclusion, the sample A is a mixture of phases, probably containing covellite, anilite ($Cu_{1.75}S$), digenite ($Cu_{1.8}S$), in any case the final characterization of the phases cannot be completed due to the poor quality of the x-ray patterns as a consequence of very broad peaks.

Sample B

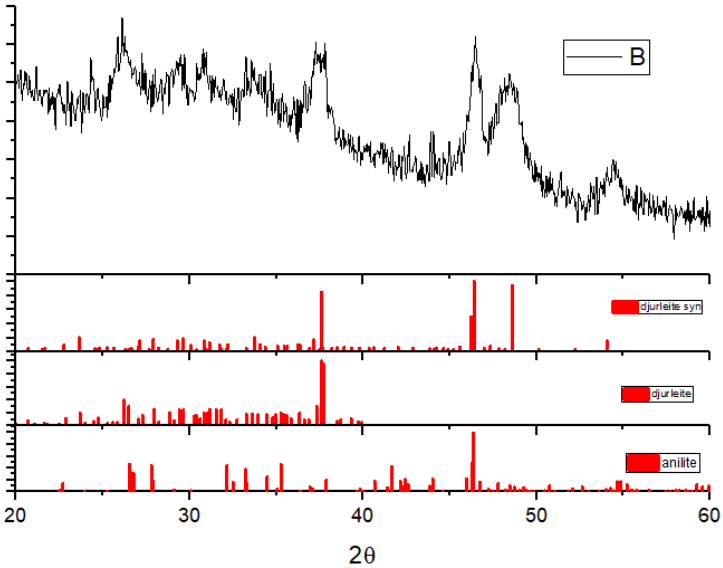

Figure 22: diffraction pattern of sample B and reference sticks of djurleite and high syn anilite

The most intense peaks in the X-ray pattern of sample B at about 26°, 37°, 46°,48°and 54° match with the expected diffraction pattern of monoclinic djurleite ($Cu_{1.96}S$). The two reported patterns of djurleite[7] show some different expected peaks but their combination match the x-ray pattern of sample B.
In conclusion, sample B contains djurleite but there are less intense peaks which cannot be clearly assigned, and it is not possible to exclude the presence of other phases in particular anilite.

Nonetheless, XRD is normally a powerful characterization method, for $Cu_{2-x}S$ system often it is difficult to assign the phase. This is due to the fact that $Cu_{2-x}S$ have 86 reported XRD patterns; these patterns are very similar and correspond to materials with small differences in stoichiometric composition. The assignation can be supported by phase diagrams since $Cu_{2-x}S$ materials with diverse composition have different stability related to temperature and phase space.
Based on phase diagram and taking into account that the nanodisks have been synthetized at 200°C, sample A should be composed by only covellite and digenite since they have a wide range of stability, while anilite shouldn't be present since, as pure phase and mixed with covellite, it is stable at lower temperature (Blachnik and Müller 2001). On the other hand, the fact that sample B contains djurleite which is stable at low temperature suggest that nanodisks, or the first nuclei, may form also at low temperature and therefore anilite could be present in sample A. Since djurleite has a narrow phase space it is highly probable that sample B contains also others $Cu_{2-x}S$ compounds and the possible presence of anilite is supported by the fact that djurleite can be obtained by the conversion of digenite which at 93°C is in equilibrium with anilite and djurleite (D.J. Chakrabarti and Laughlin 1983).
Some other problems that can affect the assignment in XRD patterns are the presence of metastable phases which cannot be found in libraries and the fact that the disk-like shape alters peak intensities and widths in the XRD pattern. For all these reasons, sometimes in literature the obtained compounds are defined as generic $Cu_{2-x}S$ or the stoichiometric composition is determined via ICP method.

[7]The only difference between the two djurleite patterns reported are that "djurleite syn" pattern has been obtained through experimental measure while "djurleite" pattern has been calculated.

Sample C, D, E

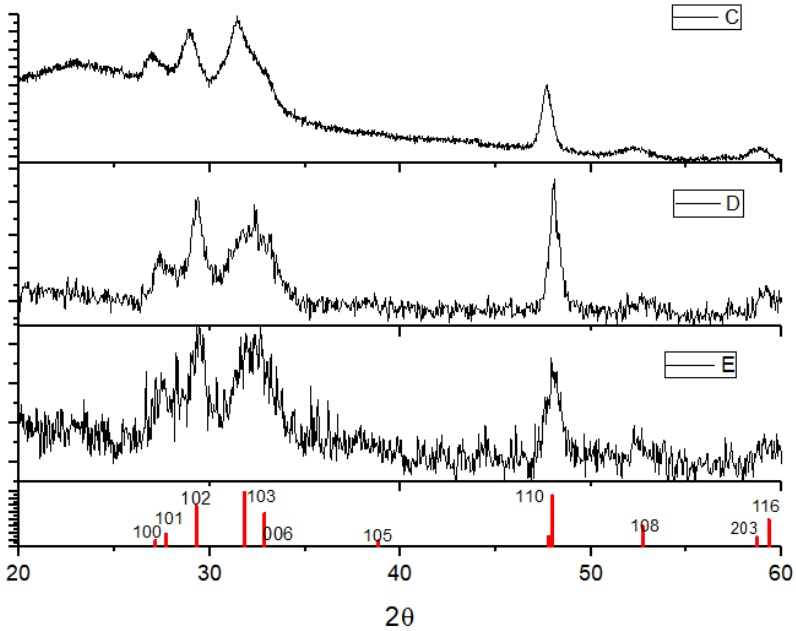

Figure 23: diffraction patterns of sample C, D, E and reference pattern of covellite reporting hkl indices

Reference pattern of covellite matches all the peaks of the experimental patterns and therefore samples C, D, E are constituted of hexagonal covellite.
XRD patterns of the three samples C, D, E are different from the bulk covellite pattern. Indeed, in these samples the XRD peak intensities and widths are altered by the nanometric dimensions of nanocrystals. As reported in literature (Xie, Carbone, et al. 2013) the (110) reflection becomes more prominent and sharp if the average volume and aspect ratio of the nanocrystals increase; this happens in less perceivable extent also to (100) and (102) reflections. The other signals, instead, are attenuated by the increase of these parameters of the nanodisks. With the analysis of the (110) and (100) reflections it is possible to estimate the nanodisk diameter while with (006) reflection the nanodisk thickness is determinable.
In the synthetized samples the XRD patterns show that the (110) reflection is the only clearly discernible one and therefore only diameters can be estimated.

sample	$D_{(110)}$ (nm)
C	14.7 ± 0.2
D	12.97 ± 0.4
E	11.37 ± 0.7

Nanodisks (NDs) final composition

In nanocrystals formation their composition is determined during the nucleation step (Jun, Choi, and Cheon 2006). Detailed mechanisms for $Cu_{2-x}S$ NDs nucleation and growth are not present in literature. Some studies of the reactions between copper and sulphur in colloidal aqueous solution can be found in literature but the still unclear ionic composition of covellite affects these works. Nevertheless, based on the work of Luther et al. 2002 in the presence of sulphide and a cupric salt a six membered ring Cu_3S_3 consisting of Cu(II) and S^{2-} should be the product of the nucleation step. The following collisions between these rings lead to covellite with the copper reduction and the formation of disulphide bonds. What reported by Luther et al.(2002) has been considered valid also using OLAM as solvent (M. Liu et al. 2015). In hot injection method the ratio between the amount of copper and sulphur sources in the reaction environment after the injection strongly influences the final NDs composition (Xie, Carbone, et al. 2013; Lesyuk et al. 2018). In heat up method, instead, the mutual reactivity of precursors influences the final ND composition. This is due to the fact that the more reactive a precursor is, the higher its monomer concentration would be, which is the actual reagent concentration. Thus, the ratio which influences the final ND composition is the ratio between monomers.

Monomers concentration changes during the heating step along with their reactivity which is influenced by temperature. Hence, the temperature range at which nucleation occurs influences the final NDs composition. From another point of view, a volume energy term and a surface-energy term contribute to the total free energy for the nanocrystal formation. The volume energy term depends on the chemical potential of the solution while the surface energy term on the geometry of the nanocrystal and on the presence of coordinating ligands. Hence, in order to obtain covellite its phase-specific chemical potential and surface-energy domain has to be identified by adjustment of a large number of factors such as temperature, solvents, oxidation states of copper and kinds of ligands present in the reaction environment.

Xie, Carbone, et al.(2013) reported that for their synthesis of covellite NDs with hot injection approach, CuCl, S powder and OLAM ODE and oleic acid as solvents, the phase stability order is the same as the calculated one for bulk Cu-S system at ambient pressure. Accordingly, at temperatures between 120°C and 500°C in a sulphur rich region covellite is the equilibrium phase with liquid S. Due to nanometric dimension of the materials the differences in thermodynamic stability among possible $Cu_{2-x}S$ are lower than for bulk phases and therefore reaction temperature is the most influential phase-discriminating synthesis parameter. M. Liu et al. (2015) reported that in their work conditions i.e. ammonium sulphide as sulphur source and OLAM as solvent the oxidation state of the copper precursor is the factor that determines the phase adopted by NDs and the use of Cu(I) instead of Cu(II) leads to much higher Cu/S ratio in the final product.

The conclusions of M. Liu et al. are valid also for samples A, B in comparison with E (which differs only in the oxidation state of copper ion used) despite what it is reported in literature the synthesis occurs at room temperature. This could be a confirmation of the presence of sulphides as oleylammonium hydrosulphide after the first heating stage at 130°C. A, B and E samples have been prepared in oil bath which doesn't allow a good temperature control but, anyway, only when copper (II) is used NDs show the XRD patterns of covellite. Furthermore, sample C which has been synthetized with a better temperature control than sample E is characterized by a narrower diameter distribution, but its NDs phase is the same. This suggest that in the first protocol conditions copper oxidation state is the key factor to obtain covellite NDs.

It Is hard to postulate the difference between Cu(I) and Cu(II) according to HSAB; Cu(I) being a soft acid should have a good affinity with double bonds in ODE, with sulphur ligands and OLAM. In particular, the non-chelating primary amino groups of OLAM despite being an hard base shows a higher affinity for Cu(I) than for Cu(II) (in water) (Cotton and Wilkinson 1988). This means that Cu(I) should be strongly bounded as required for a low ratio Cu/S in the final composition of NDs based on what it is reported by Lesyuk et al. (2018) but this is in contrast with our data. The higher Cu/S ratio in NDs in samples A and B may be due to the complexes that Cu(I) forms with the sulphur precursor after its heating. These complexes can be a first step toward nucleation of nanocrystals which might occur, in some extent, also before the heating.

TEM-SEM

TEM and SEM samples have been prepared by further purification of small sample aliquots by centrifugation with ethanol for 30 minutes at 14000rpm. Then, the obtained precipitate has been re-dispersed in toluene and SEM and TEM samples have been prepared by drop casting this solution, onto a substrate. Specimens for SEM analysis have been dropped onto a Silicon wafer which was mounted on an Aluminium stub by using a conductive carbon tape. For TEM analysis, a drop of the specimen solution was deposited on a Ni holey carbon grid, then the solvent was left to evaporate at room temperature.

In the following section, results obtained from the analysis of SEM images of A and B samples and TEM images of C, D, E samples are reported. The presence of the nanodisks is proved by TEM and SEM images where particles are disposed with random orientation. The nanodisks that lay flat have shapes that range from round to near-equilateral hexagons and also truncate triangles shaped nanocrystals are visible. Nanodisks show the natural tendency to organize into superlattices as a consequence of interparticle attractive forces. Hence, in all the samples, nanodisks self-assemble into chains where they stake face-to-face perpendicular to the substrate, sitting on their edges. Thanks to this orientation of the nanodisks, it has been possible to measure both their diameters (d) and their thickness (t) and therefore their aspect ratio (r = diameter/thickness) has been calculated. Besides nanodisks that sit on their edge forming nanoribbons also nanodisks lying flat over the substrate are visible in images and their diameter have been measured (f).

Sample E after the same purification steps to which the other samples were also subjected shows a wide polydisperse population of nanoparticles whose strong aggregation makes it difficult to obtain useful TEM

images (Figure 30). After an additional centrifugation step (6 minutes at 100rcf) a dark precipitate was present, and the supernatant has been analysed with TEM (Figure 30). The value of parameters reported for sample E have been obtained measuring nanodisks left in the supernatant.
As can be seen from Figure 24 nanodisks of sample A and sample B have similar average size and distribution widths. Samples E and D have the same diameter[8] d and it is the smallest value among the d values obtained for all the samples. Sample D shows the smallest average thickness while t value of sample E is the higher among covellite NDs samples with a small fraction of population present in both the tails of its distribution. As a consequence, sample E has the smallest ratio of covellite samples. The ratio distribution of sample D shows the lack of the smallest population and the same applies to sample C ratio distribution. Sample C has the highest average diameter and ratio values.
The smallest dimensions of sample D (which unlike sample E, it is the direct product obtained after the (standard) purification step) are explained taking into account that particle size depends on the passivation of the growing crystal by surface protecting ligand and therefore in this case by OLAM. Packing of ligands are much destroyed at higher temperature and this easier loss of protecting ligands from the semiconductor core surface leads to a faster growth of the semiconductor nanocrystals (Wu and Chen 2011).
Ratio distribution widths are more similar than the widths of other parameters, with exception of sample C that besides showing the largest ratio medium value has also the largest distribution of r. Moreover, the difference between sample C and the other samples ratio distribution widths is the most important among all. Indeed, higher reaction temperature (and longer duration) tend to produce higher aspect ratio (Hsu, Bryks, and Tao 2012), after all, also sample E included higher aspect ratio particles that have been removed by centrifugation.

Table 3: parameters of sample A,B,C,D, obtained measuring nanodisks sitting on their edge, diameters obtained measuring nanodisks lying flat and approximate diameter of sample E

Sample	parameter	value	Minimum value	Maximum value
A	Diameter d (nm)	15.0 ± 0.5	10.837	22.582
	Thickness t (nm)	7.3 ± 0.3	4.722	10.010
	Ratio d/t	2.1 ± 0.9	1.415	3.369
	Flat diameter f (nm)	14.0 ± 0.5	8.810	20.137
B	Diameter d (nm)	15.3 ± 0.8	10.237	22.015
	Thickness t (nm)	6.7 ± 0.4	3.898	8.804
	Ratio d/t	2.3 ± 0.2	1.320	3.571
	Flat diameter f (nm)	14 ± 1	8.503	19.209
C	Diameter d (nm)	16.5 ± 0.9	11.538	22.050
	Thickness t (nm)	4.9 ± 0.3	2.457	6.805
	Ratio d/t	3.4 ± 0.3	1.997	7.003
	Flat diameter f (nm)	14.5 ± 0.5	11.448	18.787
D	Diameter d (nm)	11.9 ± 0.7	6.973	16.458
	Thickness t (nm)	4.5 ± 0.2	3.245	6.173
	Ratio d/t	2.6 ± 0.2	1.889	4.214
	Flat diameter f (nm)	11.5 ± 0.7	8.472	14.195
E	Diameter d (nm)	12.1 ± 0.7	9.661	16.009
	Thickness t (nm)	5.6 ± 0.3	3.975	7.291
	Ratio d/t	2.1 ± 0.1	1.604	3.031
	Flat diameter f (nm)	11.1 ± 0.7	8.668	14.976

[8] This has been proved by performing T test on d values for E and D with $\propto = 0.01$, p value 0.5419

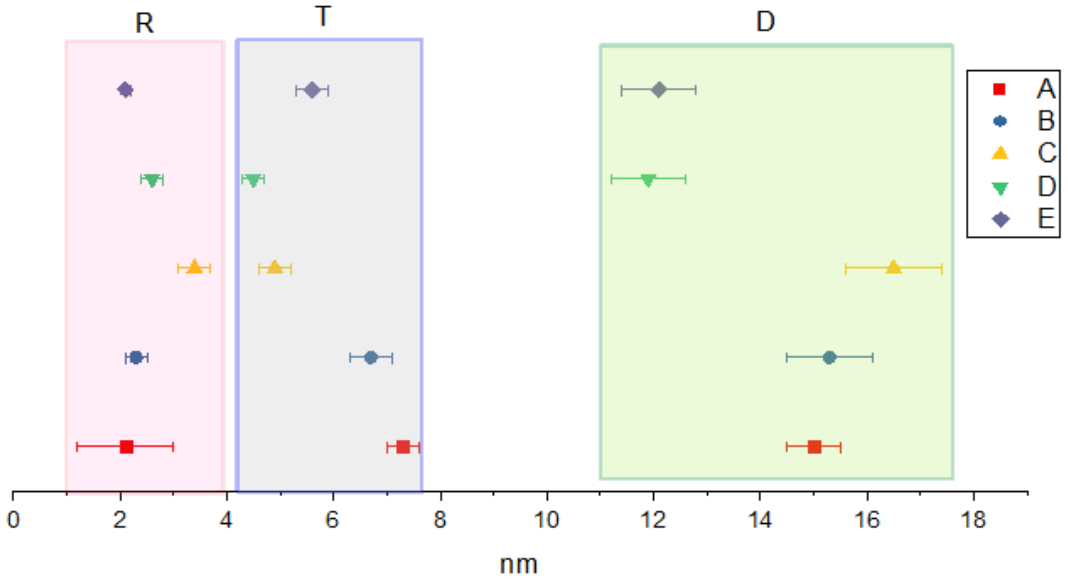

Figure 24: graphical illustration of the values reported in Table 3. D, diameters are reported inside the green box, T thicknesses are reported inside the blue box and R ratios are reported inside the violet box

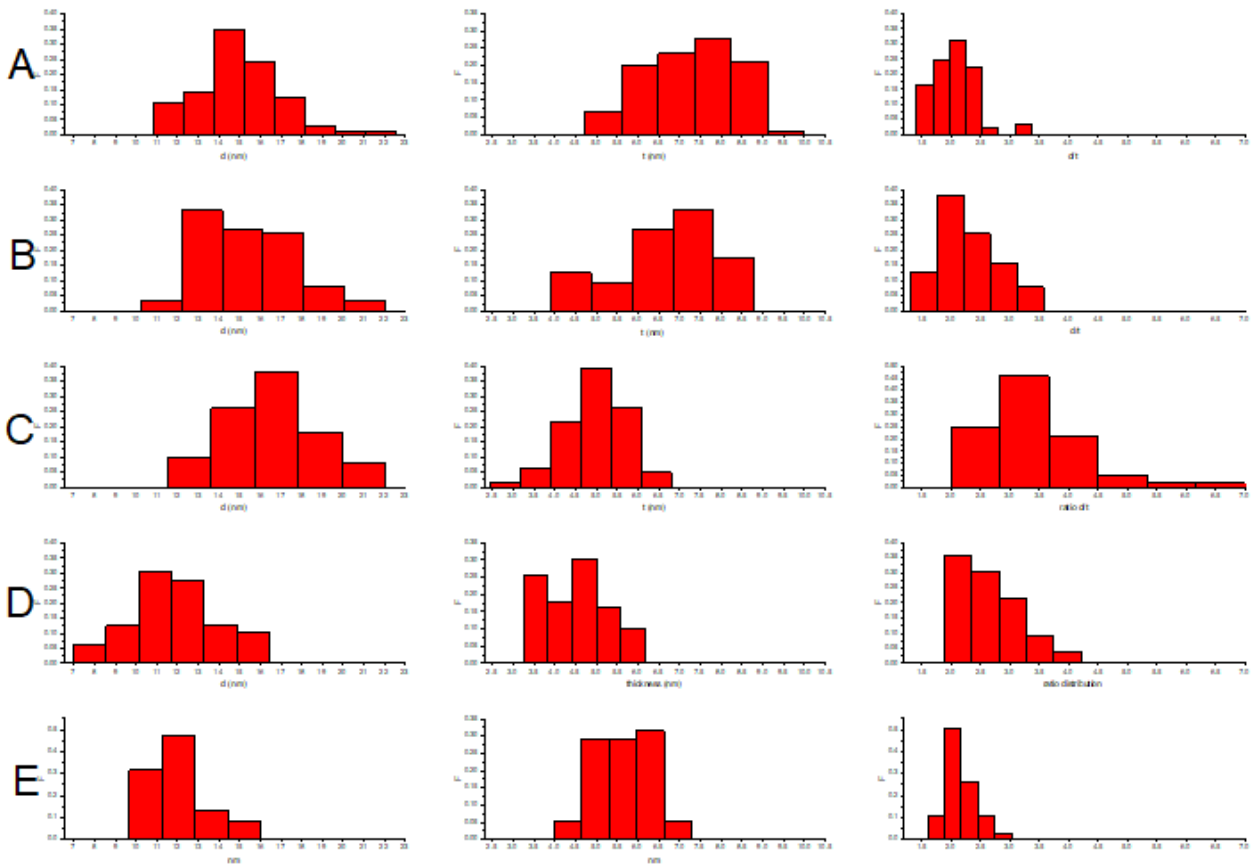

Figure 25: Distributions of the parameters determined from the measure of nanodisks sitting on their edges. From right to left: diameter d, thickness t and ratio r distributions for sample A, B, C, D, E.

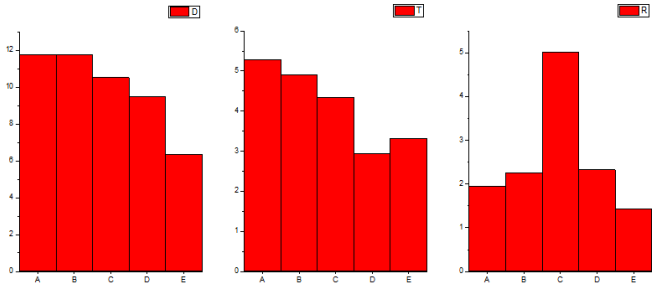

Figure 26: graphical illustration of distribution widths of values reported in Table 3 from right to left: d diameters, t thicknesses and r ratios.

The comparison between d and f distributions is reported in Figure 28. The bigger population in d distributions (first row in the left image) is not present in f distributions (second row in the left image). For non-round shaped NDs diameters values can be slightly different when measured along different axes[9]. If NDs, which are oriented edge-on, sat on their longest dimension, this dimension would be always the one measured influencing the difference between d and f distribution.

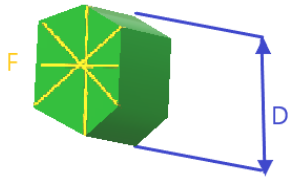

Figure 27: illustration of some of the diverse possible measure directions in a multi-facet ND.

In order to evaluate the possible effect of measuring the dimension along different axes, that can affect f but might not affect d, for sample E, where TEM images show well-defined multi-faceted NDs, the largest dimension of a selection of clearly visible NDs lying flat has been measured and reported in Figure 28 (second row in the right image). The distribution of the longer dimensions presents the lack of the bigger population and therefore this confirms that the difference of d and f distributions are not due to the measure along diverse axes, but it is due to the actual tendency of bigger NDs to sit on their edges and form nanochains.

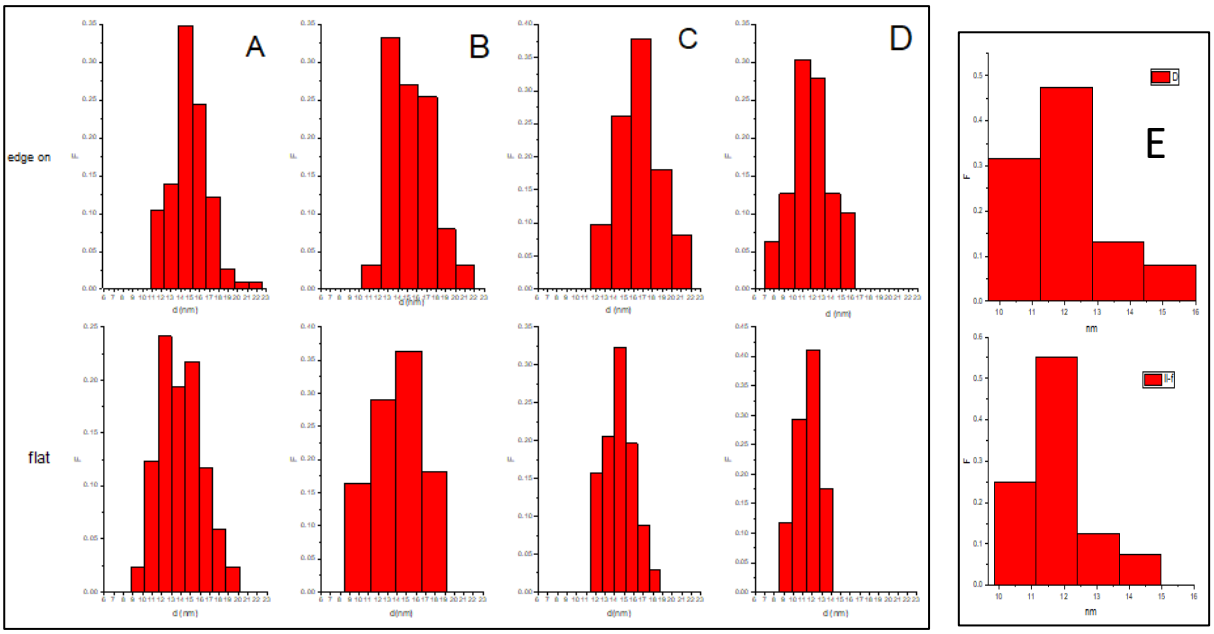

Figure 28:Left: diameter distributions obtained by measuring nanodisks sitting on their edges d (above) and lying flat f (below) for sample A,B,C,D. Right: sample E distributions of d (above) and ll-f longer diameter of multi-facet NDs lying flat (below)

[9] For clearly visible multi-faceted NDs the longer dimension has been measured but, in some cases, it was not possible to clearly distinguish between the diverse dimensions of the ND and therefore it is not excluded that shorter axes have been sometimes measured.

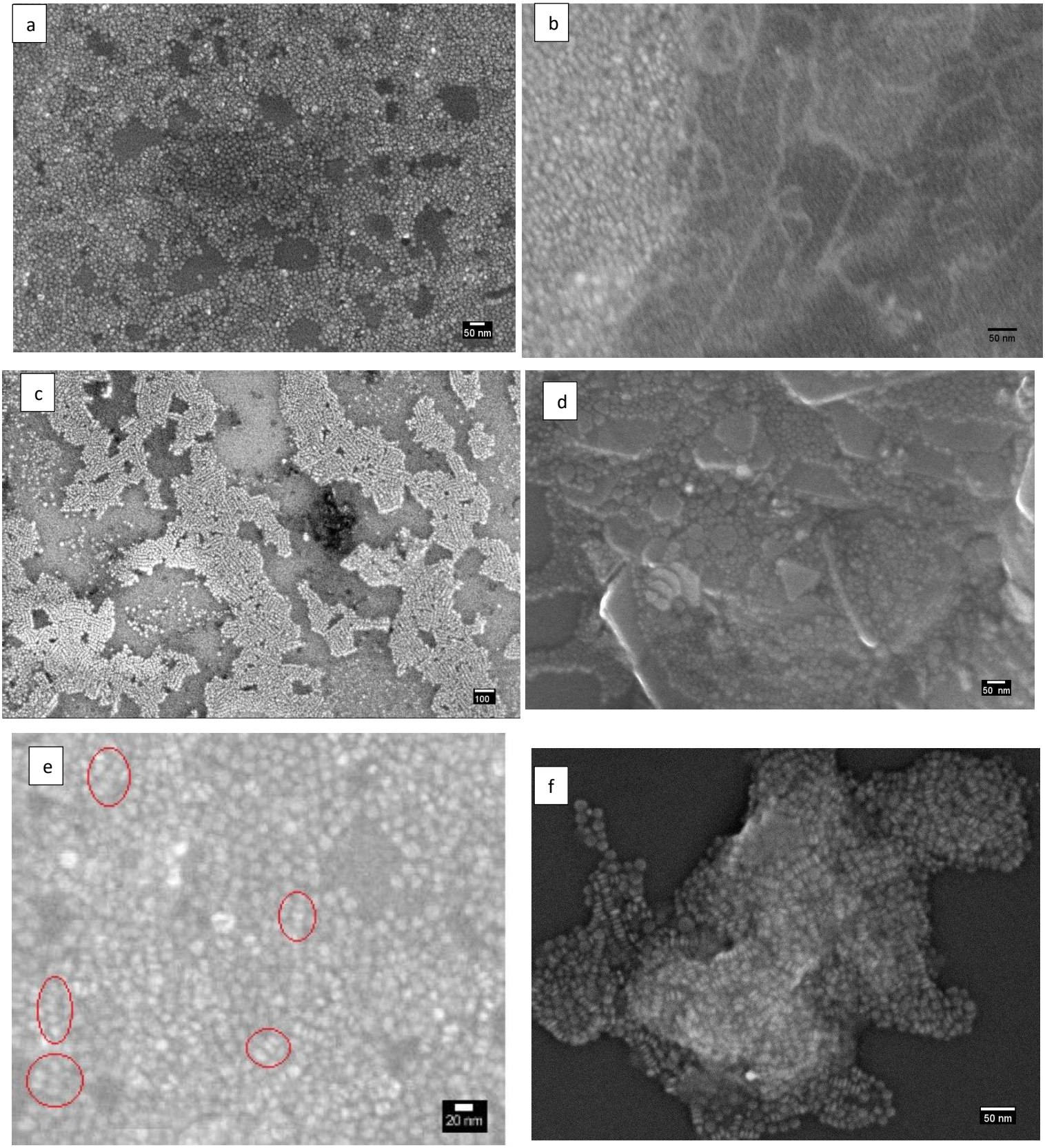
a
50 nm
b
50 nm
c
100
d
50 nm
e
20 nm
f
50 nm

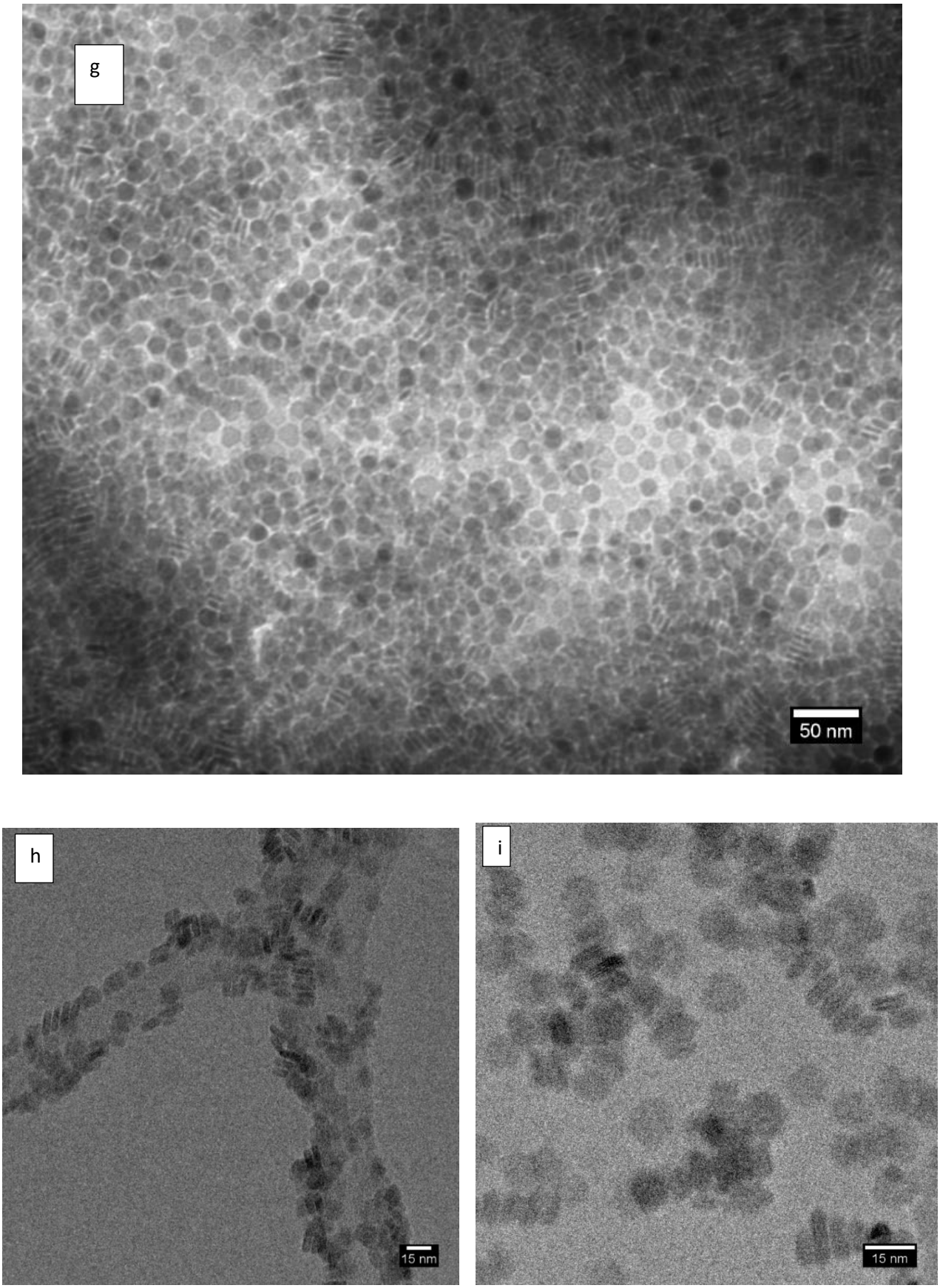

Figure 29: a,b,c,d SEM images of sample A obtained from further centrifugation of the initial solution; d is the precipitate obtained in the last centrifugation step (100g, 2 minutes) during purification. The supernatant subsequently centrifuged at 3700rcf for 20 minutes divided in supernatant showed in a,b and e images, and in the precipitate showed in image c. f SEM image of sample B, g TEM image of sample C, h and i TEM images of sample D

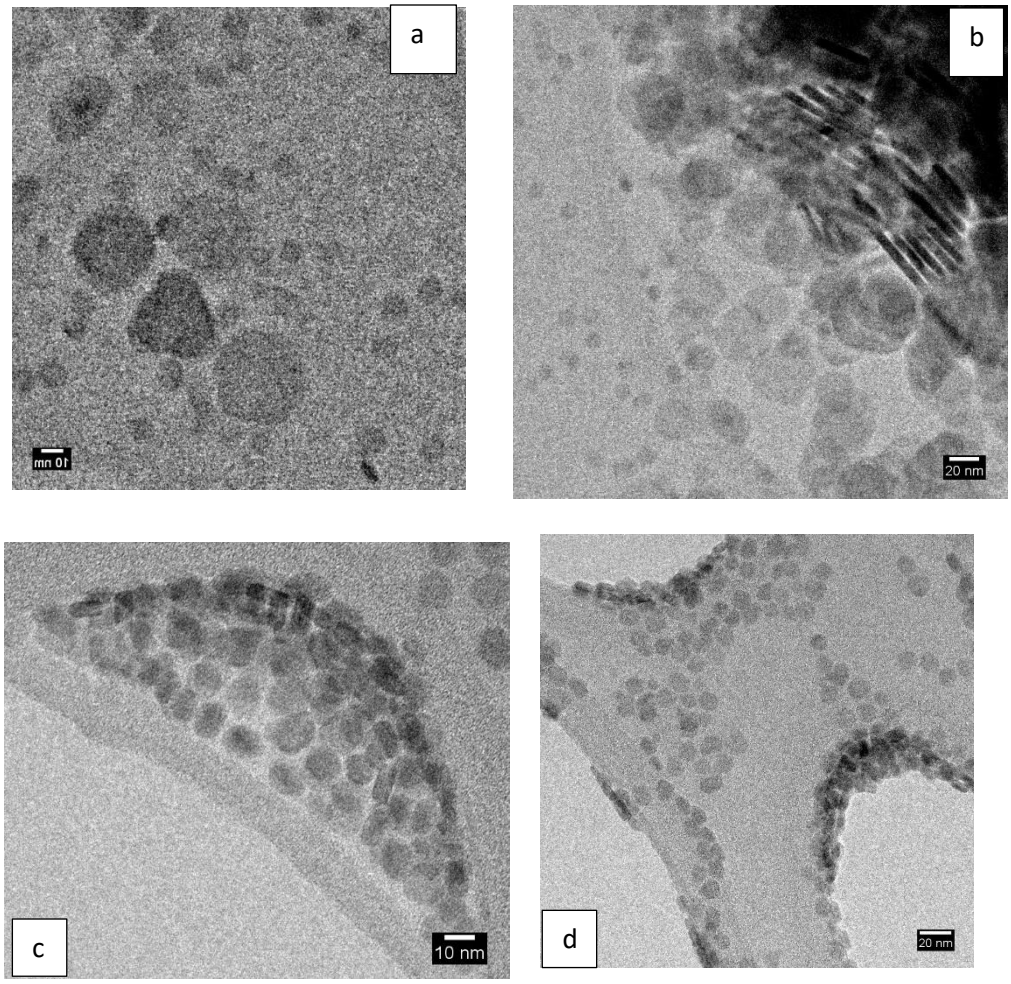

Figure 30: TEM images of sample E a,b before and c,d after the further centrifugation step

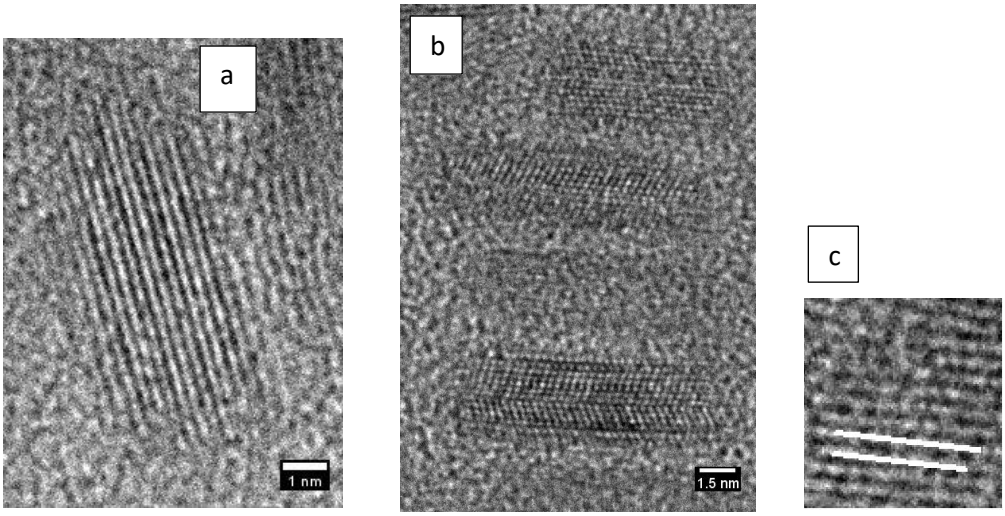

Figure 31: HRTEM images of sample D: a nanodisk edge view, b face to face stackings of nanodisks, c enlargement of a HRTEM image of a nanodisk lying flat

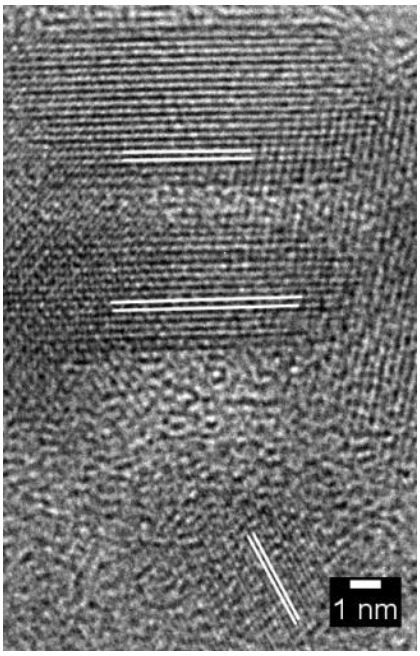

Figure 32: HRTEM image of sample E

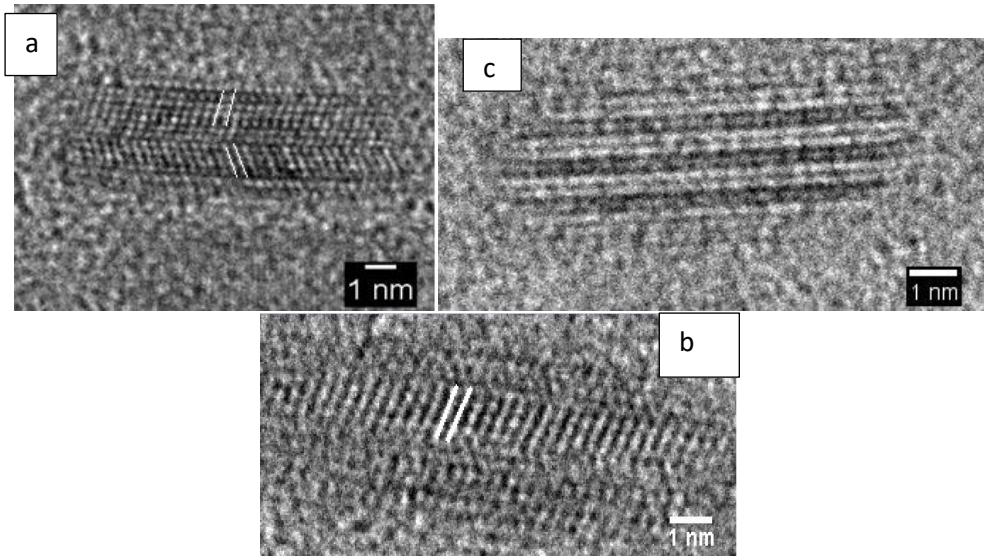

Figure 33: HRTEM images of sample D showing defects

Sample A

SEM images a, b, c, d, e, reported in Figure 29 have been obtained analysing different fractions of sample A separated by means of centrifugation. The larger particles precipitated in the last centrifugation step foreseen in the purification, at 100g for 2 minutes, are visible in image d. In image d there are big triangular, truncate triangular and hexagonal shaped 2D particles with diameters around 110nm and high aspect ratio, along with smaller disk-like particles. Nanodisks in images a ,b, c seem to have round shape but this is hard to establish from SEM images and therefore, it is not possible to exclude the hexagonal shape.

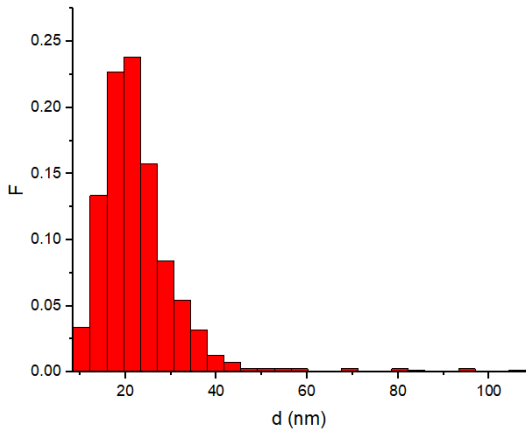

Figure 34: diameter distribution of particles in image d. Tthe average diameter is 23±1nm.

An aliquot of sample A solution, namely the supernatant obtained after the centrifugation step foreseen during purification, has been further centrifuged for 20 minutes at 3600g. Images a,b,e show the supernatant S while image c shows the precipitate P. The precipitated nanodisks show a strong tendency to stake face to face and therefore the majority of the substrate, showed in image c, is covered by nanodisks sitting on their edges, despite this also areas of nanodisks lying flat are present (nanodisks lying flat get separated from nanodisks staking face to face). Vice versa nanodisks in the supernatant tends to orientate flat over the substrate but, among these flat oriented nanodisk, chains of nanodisk stacking face to face can be seen Figure 29,a. In particular, in the left side of image b in Figure 29 long nanoribbons are clearly visible.

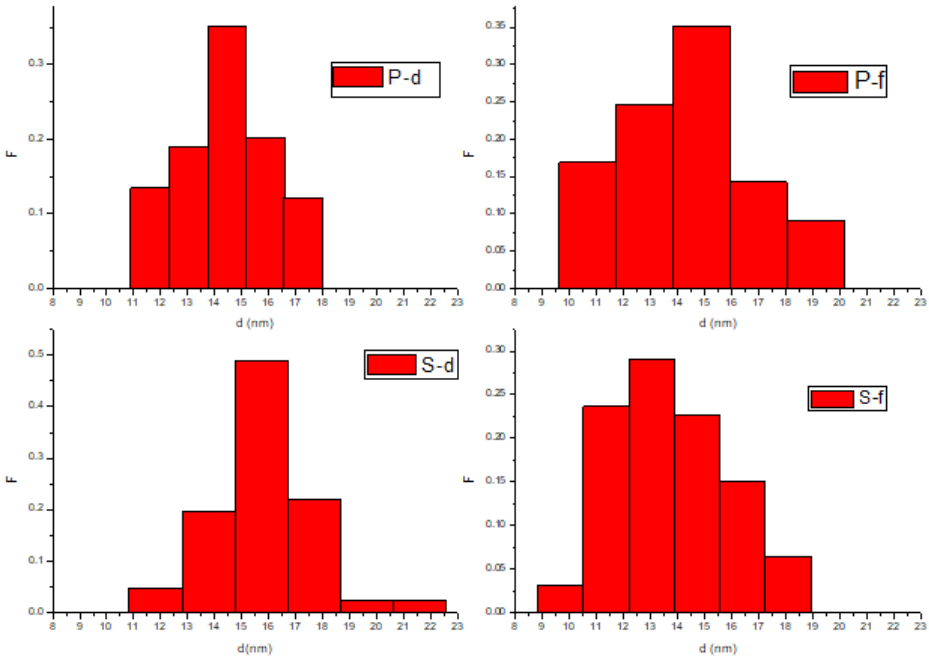

Figure 35:diameter (d left and f right) distribution of P precipitated nanodisks from sample A and nanodisk in the supernatant S.

As can be expected, the smallest population of sample A is in S where it lies flat. The larger population (20-23 nm) of sample A is unexpectedly present in the supernatant where these NDs form nanochains (they are part of the population of S-d). Differently from all the other cases, the larger population in P lies flat. On the other hand, nanodisks with size until about 20nm are present in f distributions for all the samples that have nanodisks with these dimensions (C, B, A) Figure 28. Moreover, nanodisks with diameter around 19-20 nm lie flat in P and stack face to face in S. This can suggest that the nanoribbons formation occurs also in the solution (and not only during solvent evaporation over the substrate occurring for SEM (and TEM) samples preparation) gaining a certain stability.

As it can be seen in Figure 29,e nanodisks stacking face to face can be oriented both perfectly perpendicular and tilted (evidenced inside the red circles) with respect to the substrate. These titled structures are a proof of the fact that the chains are actually composed by nanodisks and not by rods.

Sample B

Image f in Figure 29 is a SEM image of sample B. The strong aggregation of this sample is due to the different solvent in which nanodisks has been re-dispersed after the centrifugation, ethanol (which is an anti-solvent) instead of toluene. Other SEM images of aliquot of sample B treated as the other samples show the usual distribution over the substrate. However, in image f nanodisks are both oriented flat and edge on over the substrate, despite being aggregate. As reported for sample A, from SEM images it is difficult to understand the nanodisks shape but probably it ranges from round to near-equilateral hexagon while nether triangle nor truncate triangle are visible. The clearest part in the centre of the image is due to the presence of OLAM. Aliquots of samples are subjected to a further purification step precisely for reducing OLAM presence.

Sample C

Image g in Figure 29 shows nanodisks of sample C. In this case it can been clearly seen that nanodisks have round, hexagonal and truncate triangular shape. In the centre nanodisks lies flat forming more than one layer, in this area few chains of nanodisks sitting on their edges can be seen. Vice versa towards the edges of the image the majority of nanodisks form chains while few layers of nanodisks flat oriented are intercalated among them.

Sample D

Images g and h in Figure 29 are TEM images of sample D. Nanodisks showed in images g and h have round to hexagonal shape and are oriented both flat and edge on over the substrate. In Figure 31,a HRTEM image of an edge view of sample D nanodisk is reported. In this image the crystal lattice is clearly visible and a 0.27 nm lattice spacing have been measured assigning it to the (006) plane(M. Liu et al. 2015). Image c in Figure 31 is an enlargement of a HRTEM images of a nanodisk lying flat; the lattice fringes, highlighted in white, are characterized by 0.33nm lattice spacing corresponding to the (100) planes of covellite. This suggest the nanocrystal grows along the c axis along with the fact that the average dimension calculated with the (110) reflection in XRD patterns actually are in good agreement with the average diameters calculated with TEM (and SEM) images. An HRTEM image of nanodisks staking face to face is reported in Figure 31, b. The distance between nanodisks in the chain is about 1.4-1.5nm which is close to the length of OLAM (Wang et al. 2010)(Zhang et al. 2008).

In Figure 33, HRTEM images of nanodisks with defects in their crystalline lattice are shown. The white lines evidence lattices fringes with 0.27nm of lattice spacing.

Sample E

TEM images in Figure 30, a,b and d show nanodisks in sample E which have hexagonal, spherical and truncated triangular shape. As reported for the other samples, some NDs lie flat while others are sitting on their edges in particular in the perimeter of the holes in the carbon film covering the TEM grid, where NDs are more concentrated.

The HRTEM image reported in Figure 32 shows two NDs sitting on their edges and one lying flat. The white lines evidence lattices fringes with 0.27nm of lattice spacing for the edge-on oriented NDs and 0.33nm for the flat one. Accordingly, the same growth of sample D has to be occurred.

Self-assembly of NDs

NDs tend to self-assemble into chain like structures as result of Van der Waals attractive forces in equilibrium with steric repulsive forces involving the organic shell. Face-to-face orientation allows a higher interfacial contact area than edge-to-edge orientation. (Wu and Chen 2011) Self-assembly is favoured by narrow distribution, by thicker organic layer around the particles and it is more probable for large NDs as has been verified by the comparison between f and d. On this basis, sample D should have the highest propensity to

self-assemble since it has the narrowest distributions and has been synthetized at the lowest temperature and therefore it should have the thicker OLAM layer.
The superlattice structures visible in TEM and SEM images are formed by drying mediated assembly of NDs. During solvent evaporation the possible interactions between particles drive the organization. The factors that controls the process are the solvent dielectric constant, its volatility, polarity and temperature, furthermore also NDs size distribution and concentration give their contribution. Considering that the preparation procedure of TEM and SEM samples affects these parameters and that it is not fully reproducible, for example it is not possible to have a control on the temperature, it is not feasible to compare samples tendency to aggregate from TEM and SEM images.

Shapes

The fact that copper suphides 2D nanocrystals can be obtained with different shapes: round, hexagonal, triangular and truncate triangular is reported in literature(Lesyuk et al. 2018)(M. Liu et al. 2015)(Zhang et al. 2008; Xie, Carbone, et al. 2013)(Wu and Chen 2011) and their simultaneous presence in colloidal approach is common.
The obtaining of NDs with different shapes can be explained with the kinetic and thermodynamic mode of growth. Nanocrystals grow through a series of sequential reactions each of which brings to a product with a determinate shape, only the product with the minimum of energy is the thermodynamic product. Hence the control of shape is achieved by the control of the kinetic and thermodynamic mode of the growth.

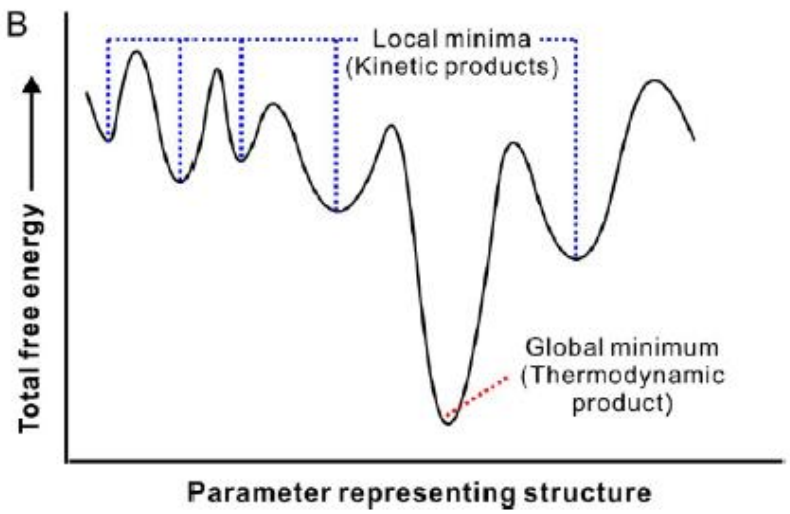

Figure 36: illustration of thermodynamic versus kinetic control for a series of sequential reactions(Xia, Xia, and Peng 2015)

Besides the thermodynamic product that should be the expected one, other products deriving from growth controlled by kinetic, can be trapped in many states and therefore shapes that correspond to others local minima of energy can be found. Kinetic or thermodynamic modes of growth are determined by reaction conditions such as temperature, pressure and reaction environment. The obtaining of the thermodynamic product can be favoured by higher temperature and by aging the sample for long period of time. The shape of the thermodynamic product can be oriented toward the desired shape by introducing ligands showing selective adhesion to a particular facet of the growing crystal, as is done by OLAM. Through the binding of the ligand to a particular facet its specific surface free energy decreases, and the final crystal shape will maximize that facet. Knowing that the thermodynamic mode refers to the final product, but it doesn't give any information about the reactions that bring to this, the role of the active ligand can be also understood by kinetic perspective and therefore when the ligand is absorbed to a specific facet the growth along that it is slowed down giving rise to the formation of a shape that maximize that facet. The thermodynamically less favourable products are obtained when atoms that initially added to the most active site in the crystal, are not able to migrate toward sites with lower surface energy. In this way products are trapped to the kinetic controlled shapes. The kinetic parameters relative to the rate of atom deposition and surface diffusion are the ones that influence atoms ability to migrate after deposition and therefore they are the ones to control

for obtaining kinetic products. The deposition rate is mainly influenced by monomers supply rate at the surface and therefore by monomers concentration, temperature, and coordinating ligands present. Surface diffusion rate is influenced by temperature, strength of bond between the surface atom and the adatom, the crystallographic plane of the surface, the accessibility of the surface (e.g., passivation by a capping agent), and the chemical potential gradient.

The obtaining of different shapes has been studied for hot injection synthesis of covellite nanocrystals (Lesyuk et al. 2018). In the case of hot injection method, the ratio between copper and sulphur is a key factor for achieving the desired shape of nanodisks (as well as their desired composition) and therefore for heat up synthesis the mutual conversion rate from precursors to monomers has to play an important role.

Triangles are kinetic products and therefore are promoted by high local concentration of monomers. As already reported, when OLAM binds to a growing crystal, it modifies the growth rate of different facets favouring the thermodynamic product shape. OLAM attitude for binding to the diverse facets can be understood by considering its absorption energy on them. The selective adhesion of OLAM occurs on (001) facet, as already reported, but it can bind also to other facets. The absorption energy calculated for Cu-rich (100) facet is larger than for (110). This means that the (100) grows slower and this results in truncated triangles and hexagons with (100)-like edge facets. Furthermore for (100) facets the absorption energy is lower for S-terminated that for Cu-terminated and therefore OLAM passivates preferentially Cu-rich facets slowing down their growth. Vice versa, if there is a sulphur rich environment the monomer addition is promoted and so the growth will be under kinetic control thus leading to the formation of triangles.

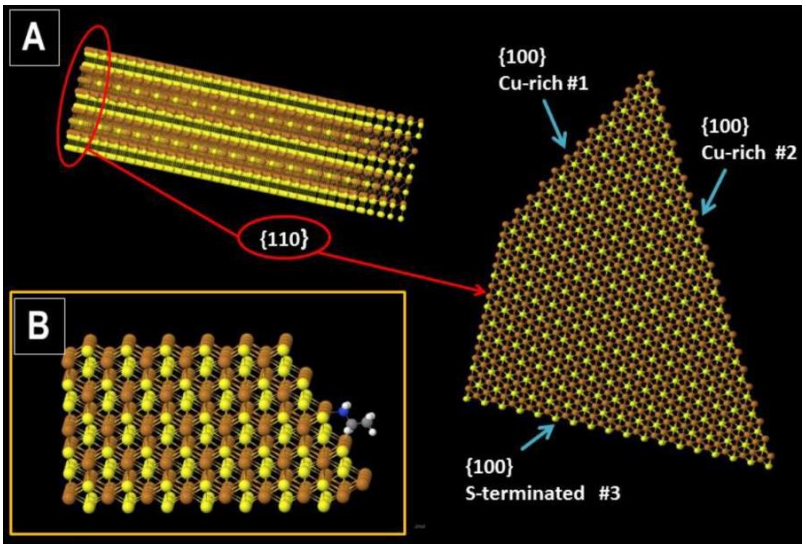

Figure 37: Atomic models: a. CuS faceting and b. amine group of OLAM absorbed at the (100) facet (Lesyuk et al. 2018)

The most reactive sites are the triangle tips, and those can be occupied in the case of a sufficient supply of sulphur. Kinetics products are characterized by the maximization of the surface area, while when growth is thermodynamically controlled, particles develop 6 facets to minimize the surface energy. With the dissolution of the smaller particles also triangular tips dissolve since these are instable having the largest curvature radius. To retain the triangular shape, monomers have to react at positions near and at the vertices and this is possible only with a sufficient monomer supply rate. When this rate decreases the growth occurs at the side facets (orange arrows) leading to the development of other 3 facets from the corner with the formation of truncated triangles and hexagons.

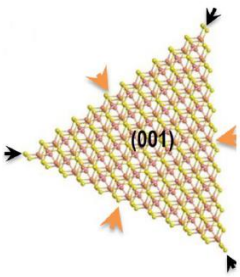

Figure 38: triangle of CuS with sulphur terminations (Lesyuk et al. 2018)

The illustration in Figure 39 is referred to a hot injection approach and therefore in that case the ratio between copper and sulphur can be assumed as the precursor ratio since the conversion to monomers is total after the injection. Nevertheless, also for hot injection method it has been reported (Lesyuk et al. 2018) that ligands present in the reaction environment can influence the reactivity of precursors. In the case of heat up synthesis precursor reactivity defines their conversion and therefore monomer concentration and the temperature at which they are obtained. For these reasons it is not possible to compare the hot injection results with the ones of heat up methods.

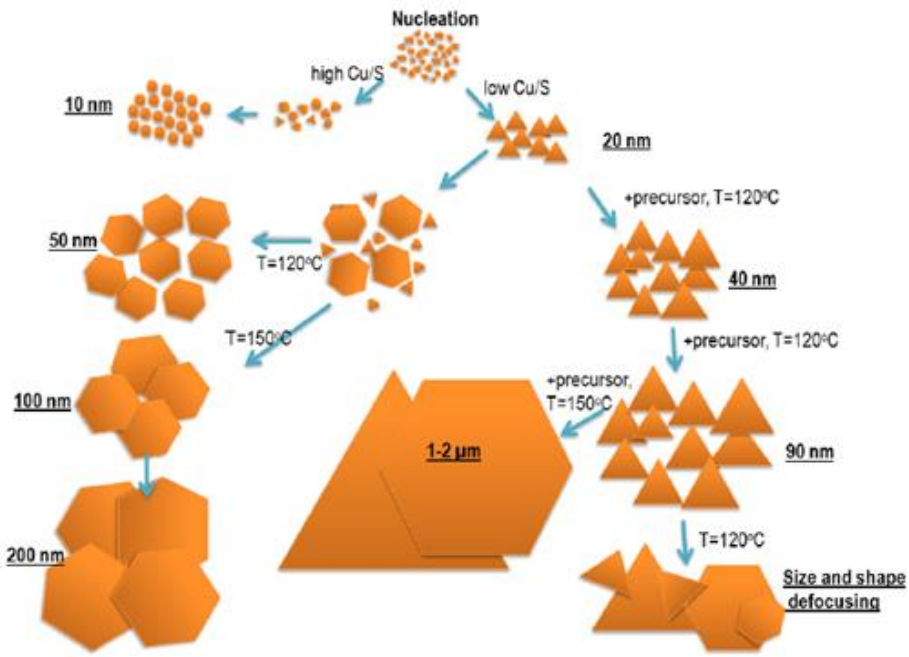

Figure 39: Scheme of the shape transformations during OLAM-S based hot-injection Cu_xS synthesis depicting ways to control the shape. Blue arrows denote time flow.(Lesyuk et al. 2018)

In the 2 protocols utilized in this work for the nanodisks synthesis, the ratio between copper and sulphur is in both cases 1:2. Nevertheless, in the first protocol the sulphur precursor is heated to 130°C for 30 minutes before the copper addition and therefore a certain fraction of sulphur should be present as oleylammonium hydrosulfide thus increasing the concentration of sulphur monomers in the reaction environment; vice versa in the second protocol the sulphur precursor is added to a copper precursor solution without any former heating step and therefore the ratio Cu monomers/ S monomer should be higher than in the first case. The size distribution for sample D is the narrowest among the other sample size distributions (taking into account sample E before the additional centrifugation step) and also, its NDs shapes are quite homogeneous going from round to almost hexagonal, without triangles or truncate triangles. This may suggest that, beside the lower temperature, nanodisks of sample D are the result of a high ratio Cu/S characterizing the environment reaction during the synthesis. Based on the presence of different shapes in sample C it can be said that the kinetic mode has been more important for that sample and therefore this finding sustains the hypothesis of a higher concentration of sulphur monomer. As regard to sample E, it is characterized by triangles and hexagons with huge dimensions (before the additional centrifugation step) suggesting beside the low ratio Cu/S also the progressive formation of monomers. After the purification, the smaller population characterizing sample E, as shown by TEM images, have NDs with shape similar to the ones of sample C and this is a further confirmation of the greater importance of kinetic growth in the first protocol than in the

second one[10]. The comparison between sample E and C is an example of the temperature role during the synthesis since the difference between them is the heating system used. Hence, in the case of sample E, which has been obtained using an oil bath as the heating source, the heating rate has been slower that the 8°C/min required; the effect of this slower heating rate was the formation of a lower number of nuclei and of many crystals having big dimensions. The resulting size distribution was broad enough to prevent the separation between the smaller and bigger NDs population through the centrifugation in the purification step.
In order to clarify precursors conversion rate and concentration during the reactions, samples collected at different reaction times are needed.

FT-IR

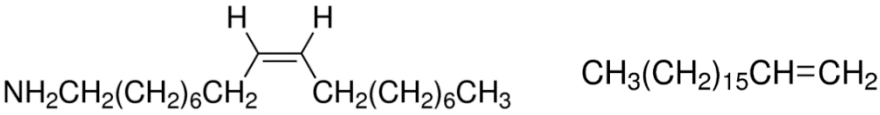

Figure 40:a. oleylamine structural formula b. 1-octadecene structural formula

Table 4: positions of the most important ligands groups bands (Silverstein, Webster, and Kiemle 2015)

Primary aliphatic amine groups	band position (cm-1)	Unsaturated carbon chain groups	Band Position (cm-1)
Stretching N-H	3300-3400 two weak	Stretching =C-H	3008
Bending N-H	1650-1580	Bending C-H	~1647 and ~1642
Stretching C-N	1250-1020	stretching C-H.	3000-2840
		Bending ⊥ =C-H	~915

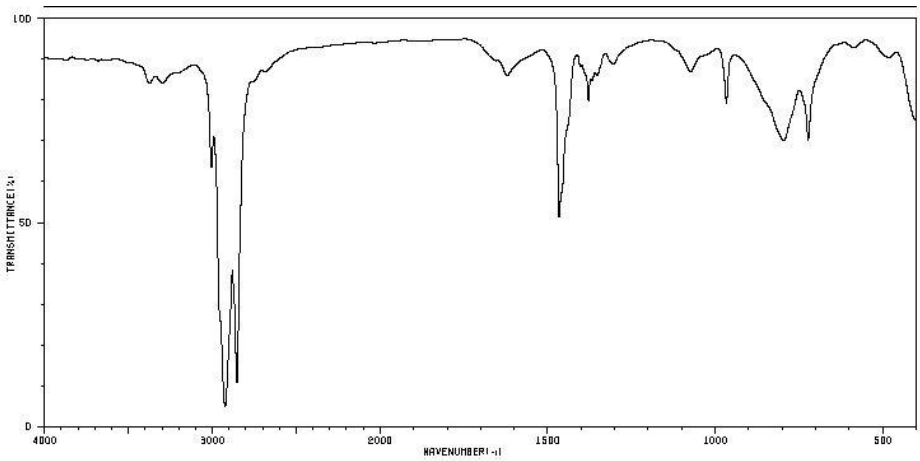

Figure 41: FT-IR spectrum of pure OLAM

[10] As regard as sample A and B, only SEM images are available and from these is hard to establish if triangular or truncated triangular shaped NDs are present in the smallest population but these shape are clearly visible in the bigger population

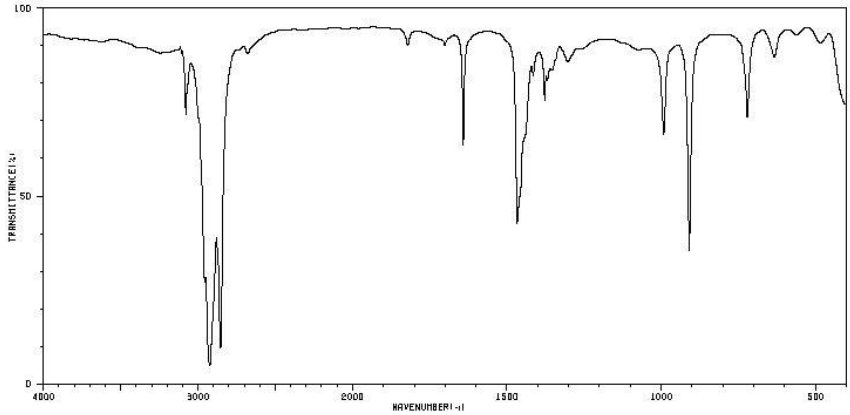

Figure 42: FT-IR spectrum of pure ODE

The FT-IR spectra of sample A, B, C, D, E have been collected in the 600-5000 cm^{-1} range.

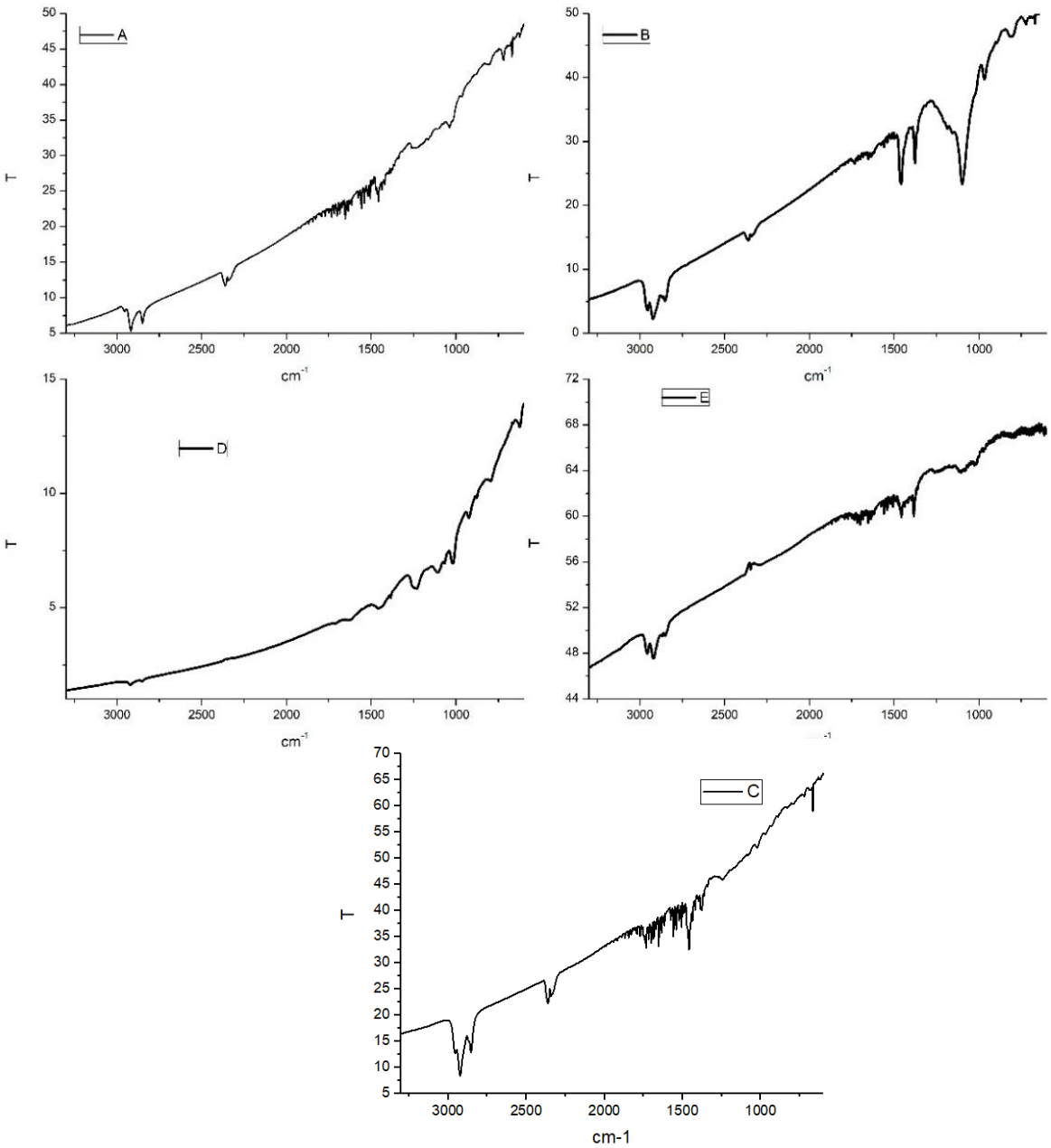

Figure 43: FT-IR spectra of sample A, B, D, E, B and (below) C.

In order to clearly identify bands and to compare the samples, FT-IR spectra have been separated into two acquisition ranges; the two ranges, 3100-2750cm^{-1} and 2000-600 cm^{-1}, cover the regions where bands are present.

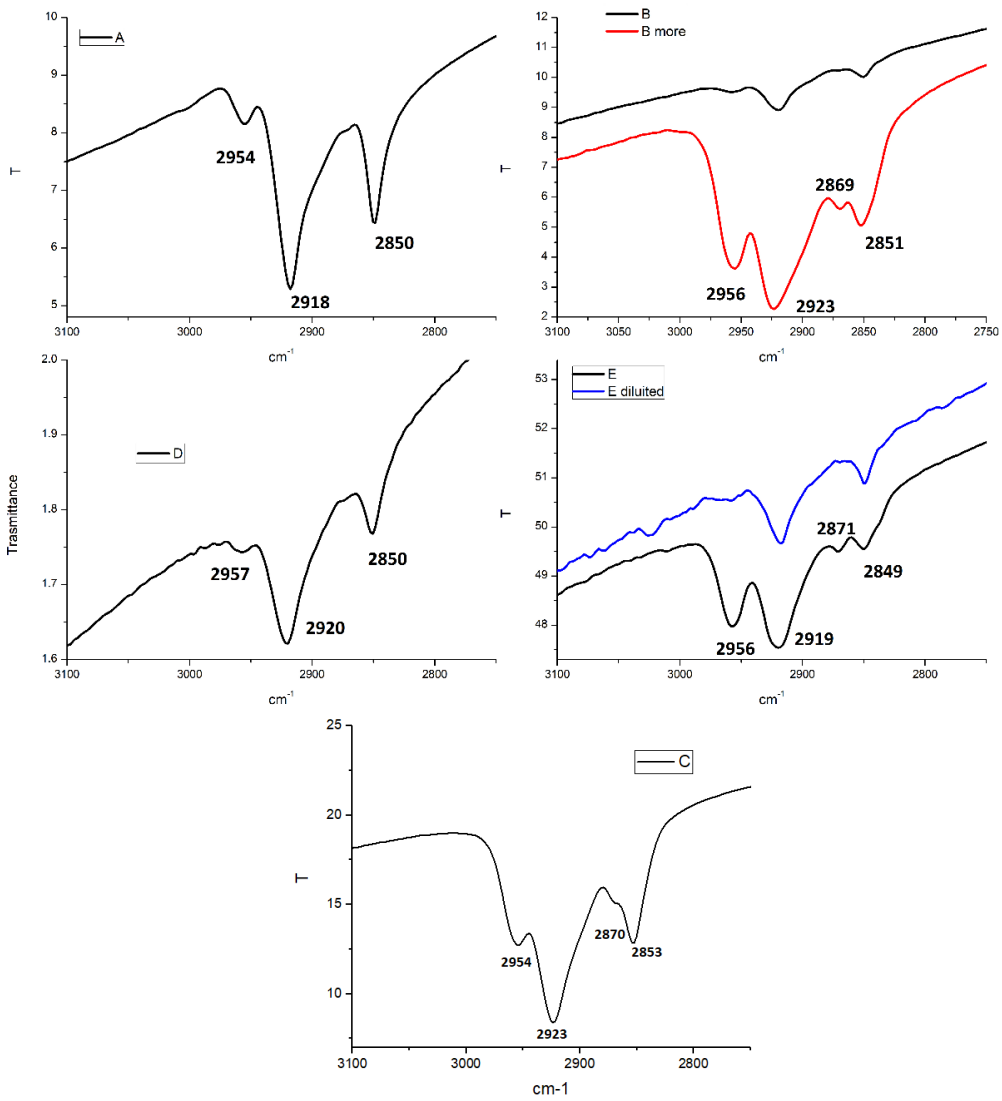

Figure 44: First part of FT-IR spectra of sample A, B, D, E and C (below). "B more" (red line) is the spectra of sample B with an increased amount of nanodisks in the KBr pellet. "E diluted" (blue line) is produced from a dilute solution of sample E.

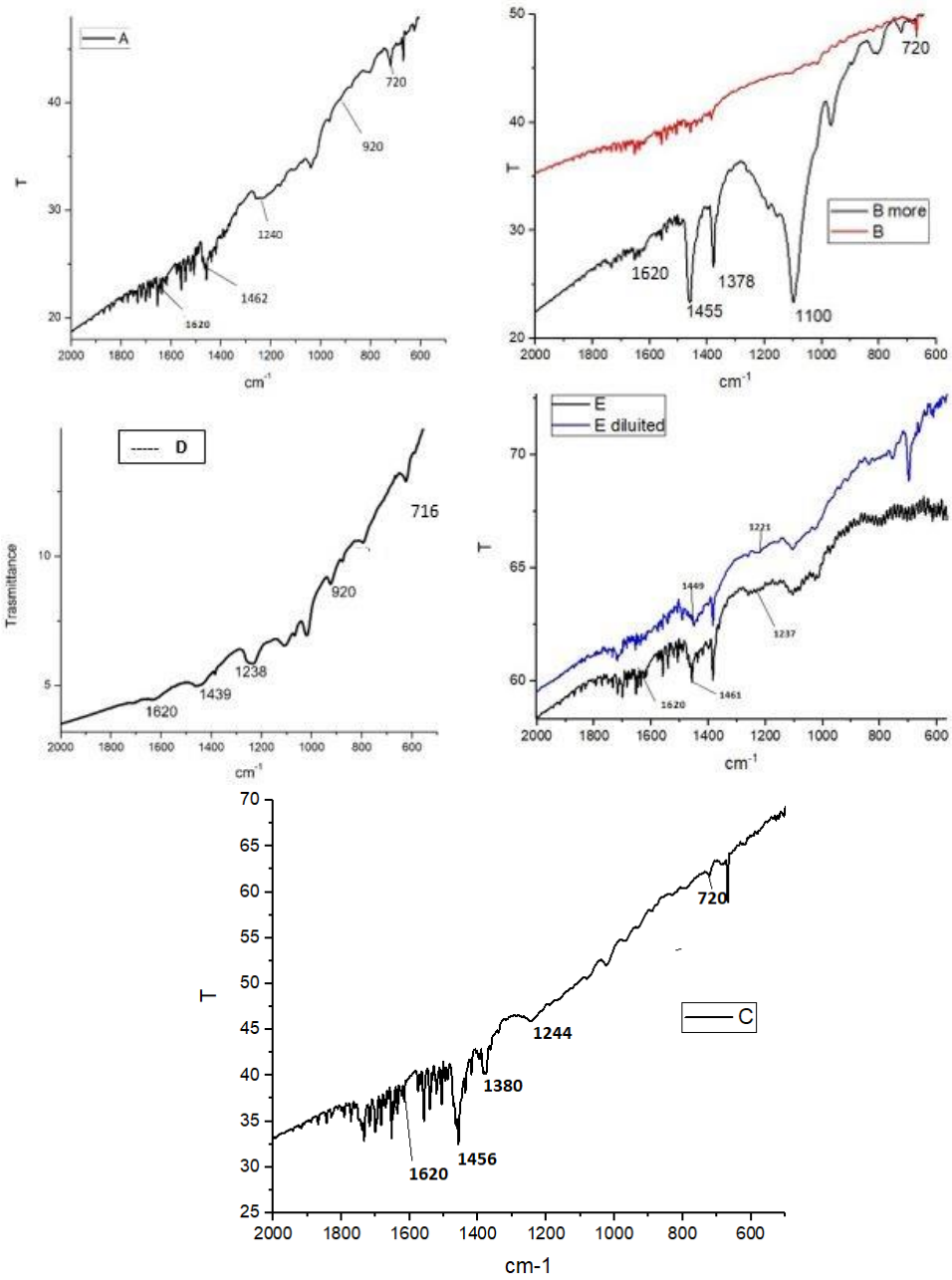

Figure 45: Second part of FT-IR spectra of sample A, B, D,C, E. "B more" (red line) is the spectra of sample B with an increased amount of nanodisks in the KBr pellet. "E diluted" (blue line) is produced from a dilute solution of sample E.

The spectra are influenced by the amount of NDs presents in the KBr pellet analysed. In order to understand how the ND concentration influences the spectra and to evaluate if the organic layer of NDs changes with dilution (of their solution), spectra of "B-more", namely the spectra of sample B with an increased amount of nanodisks in the KBr pellet, and of "E-diluted", produced from a dilute solution of sample E, have been reported.

In Figure 44 the differences between "B-more" and B and between "E-diluted" and E are comparable. This means that the difference between spectra of samples E cannot be attribute to any variation in the organic shell due to the dilution but only to the smaller quantity of nanodisks in the KBr pellet. This is confirmed by the fact that sample E and "E-dilute" have the same band positions and same ratio between band intensities. Consequently, the organic shell doesn't modify with dilution or at least possible changes can't be indagate with the IR spectra.

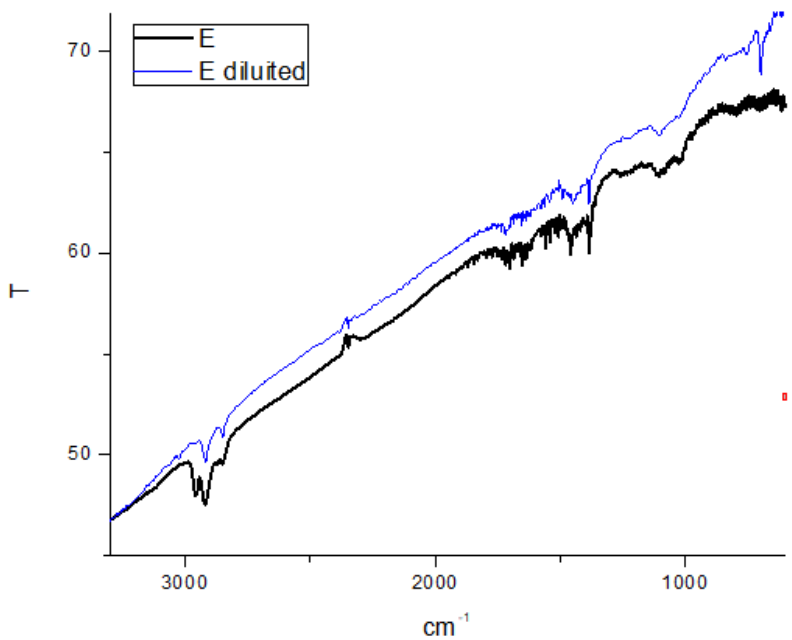

Figure 46: comparison between the spectra of E and E diluted

From the comparison between "B more" and B and E and "E dilute" it results that when the signal is due to a less concentrated pellet the band at ~2870 cm^{-1} is less intense and appears like a really weak shoulder. However, sample D is the exception, in fact despite having been obtained from a concentrated KBr pellet (this can be understood from its second part of the spectra where bands are clearly distinguishable) it has a weak shoulder at ~2870 cm^{-1}. Indeed, Sample D IR spectrum is different from the spectra of all the other samples since it doesn't show multiple narrow peaks between ~1800-1400 cm^{-1}; bands intensities between 300-2800 cm^{-1} are lower than for the other samples.
The samples spectra compared to the spectra of pure ligands are different. The N-H stretching band is weaker and its frequency is shifted to smaller wavenumbers (~2956cm^{-1}) based on what it is reported by Xie, Carbone, et al.(2013). Nevertheless, peaks present between 2840-3000 cm^{-1} should be assigned to C-H stretching vibrations and therefore the band of N-H stretching could be completely quenched and therefore not present in the spectrum. Anyway, both cases suggest that the amino group is linked to the CuS surface. Another characteristic band of the amino group is the N-H bending band which is weak and broad at ~1620 cm^{-1} and it is clearly visible in the spectra of sample B and D. In the spectra of samples A, C, E this band is hardly visible but it is present in the multiple narrow signals region. The band of C-N stretching is visible as a weak and broad band at around 1238 cm^{-1} and it is present in samples D, C, E and A (in particular taking into account the weakness of the signal) while it is not visible in sample B where it is probably covered by the strong band at 1100 cm^{-1}. This band at 1100cm^{-1} could be assigned to the C-N stretching which can occur in this position. On the other hand, since the IR spectra of different CuS particles (reported in the following chapter) show this band without containing C-N bounds this band has to be due to the particles. This band is visible also in the spectra of the other samples but its intensity is really low. The other 2 sharp and intense bands at 1455 (CH2 bending) and 1378 (asymmetric bending CH3) cm^{-1} present in the spectrum of sample B are visible also in the spectra of samples E and C. Only the band at 1455 cm^{-1} is present in the spectrum of sample A and both bands in the spectrum of sample D where the band at 1455 cm^{-1} is broader than the band at 1378cm^{-1}. The spectra of sample D and, less clearly, sample A show a band due to ODE at 916cm^{-1}.
FT-IR spectra of all the samples suggest the presence of a first layer of OLAM linked to the CuS particles. A second layer composed of intercalated ODE and OLAM bonded via hydrophobic interactions is probably present in sample D and sample A.

Based on what it is reported by (Boey et al. 2007)(Dixit, Mahadeshwar, and Haram 1998), CuS should be IR inactive but, on the other hand, the multiple narrow signals between ~1800-1400 cm^{-1} and the band at ~110cm^{-1} that are present also in the IR spectra of different copper sulphides particles with different organic

ligands, have to be due to the particle core of $Cu_{2-x}S$. It can be said that when these bands are not present in the IR spectra the organic shell has to be thicker avoiding the interaction between light and the particles core. Thus, as it is expected from its lower temperature synthesis, sample B has the thicker organic layer. This suggests the higher tendency to self-assembly since this is favoured by the thick organic layer (further discussion will follow in the next paragraph). This is confirmed by what it is reported by Zhang et al. 2008 that experimentally established diverse IR spectra (reported in Figure 47) for nanodisks that don't tend to assemble and nanoribbons which vice versa show a strong tendency to form nanochains.

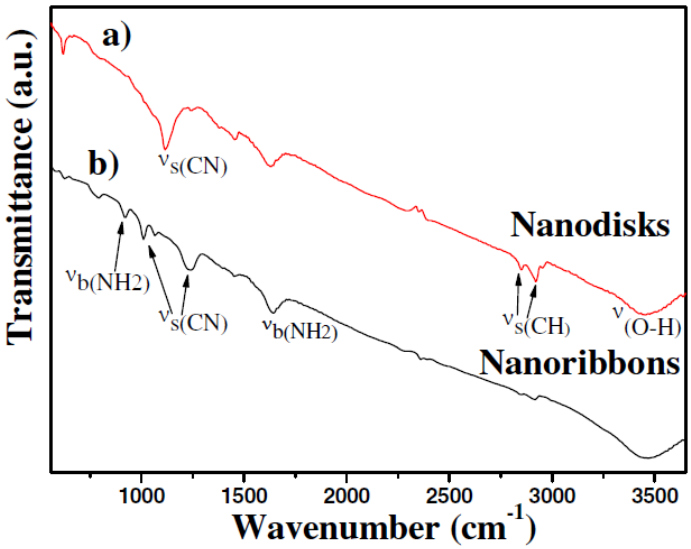

Figure 47: FT-IR spectra of covellite nanodisks and nanoribbons (Zhang et al. 2008)

Besides the diverse attribution to the band at ~110cm^{-1} the conclusions drawn by Zhang et al. are consistent with what was previously reported.

UV-VIS Spectroscopy

For copper sulphides nanocrystals the relationship among their structure, and composition and their optical properties are still poorly understood (Kriegel, Scotognella, and Manna 2017).Optical modelling through theoretical methods allows to predict and understand the optical response. A significant theory to approximate the dielectric properties is the Drude-Sommerfeld model.

Drude-Sommerfeld model

The Drude model (Dm) has been improved by Arnold Sommerfeld and the resulting model bearing the name of both scientists. In Drude-Sommerfeld model (DSm) electrons (for metals) are treated as quantum mechanical particles rather than classical particles. As in Dm also in DSm carriers (electron in the model) are not bounded to any atom in the lattice and, since the potential within the solid is assumed to be uniform, electrons haven't any preferred site and are free to move within the entire solid. In both models particles are identical but in DSm these are indistinguishable unlike in the Dm). Maxwell-Boltzmann statistics is used in Dm since it describes classical particles. Instead, since in DSm, particles obey to the Pauli's exclusion principle these are described with the Fermi-Dirac statistics. Hence, in DSm to each energy level are associate 2 states corresponding to the two spin orientations. If the total number of the particles at two energy levels remains the same, and a few particles from one energy level are simply swapped for the same number of particles from the other energy level, this does not count as a new microstate for the system unlike in Dm where particles are distinguishable. The Sommerfeld corrections allowed to address the anomalies in the estimation of specific heat and root-mean-square value of speed that occur using the Drude model. When the number of holes in the valence band or electrons in the conduction band is much smaller than the available states Pauli's principle can be ignored, and Maxwell-Boltzmann statistics can be used. For degenerated semiconductors and metals which have a larger number of carriers the Fermi-Dirac statistics has to be used.

With regard to the dielectric function ε(ω) and plasma frequency ω_p their equations derived from the assumptions of Dm are still valid and therefore, as reported in the introduction section, are:

$$\varepsilon(\omega) = \varepsilon\infty - \frac{{\omega_p}^2}{i\gamma\omega + \omega^2} \qquad \omega_P = \sqrt{\frac{N_h e^2}{\varepsilon_0 m_h}}$$

The theoretical modelling of CuS NDs NIR spectra

The theoretical modelling of NIR spectrum[11] of covellite ND LSPR has been reported by(Xie, Carbone, et al. 2013)[12] based on electrodynamic scattering simulations[13] performed within the frame of the discrete dipole approximation (DDA[14]) and using the DSm[15].

With this approach it has been possible to assign the multiple LSPR modes, due to shape anisotropy, finding theoretical curves that faithfully reproduce the experimental spectral features. The good agreement between experimental and modelled LSPR with DSm means that covellite NDs has to hold an actual metallic-like electronic structure that lead to inherently hole to behave like free carriers, delocalized within the valence band (Drude type carrier). This behaviour is different from other $Cu_{2-x}S$ where holes that give rise to LSPR are characterized by a substantial degree of localization. Indeed, the calculated hole number for covellite NDs is $N_h \approx 0.98 \times 10^{22}$ cm^{-3} ([16]) which is close to several metals values of free carrier concentration and 7 to 13 times higher than the value determined for $Cu_{2-x}S$ with $1.93 < 2-x < 2$. Since, based on what is reported by Xie, Carbone, et al. the plasma frequency for different dimension NDs is the same, the free carrier density does not depend on dimensions and therefore the tunability of the LSPR is due to the geometric features.

NDs as platelet-like nano-objects are expected to show two peaks one for the in-plane mode and a second for the out-of-plane mode. For covellite CuS usually, only one peak is present in the absorption spectra. Since, the wavelength values corresponding to the peaks maximum (λ_{max}) of the in-plane and the out-of plane modes are separated by a small energy and the fact that the out of plane LSPR mode has a low intensity this last can be hardly seen only in larger NDs as a high frequency shoulder of the in-plane peak. The different LSPR showed by the two modes can be understood remembering that covellite structure has metallic-like 2d sheets staked perpendicular to the c-axis. For covellite, indeed, the ω_p is strongly anisotropic and therefore its lower value for the out of plane mode implies that, compared to a same shaped noble-metal ND, its bands fall at longer wavelengths and have a further reduced intensity.

---

[11] The DSm can be applied only at λ higher than 500 nm. Indeed, at lower wavelengths interband transitions occur and in this situation the function of ε(ω) foreseen by the model is highly inaccurate.

[12] Cited and confirmed in literature for covellite CuS NDs (Hsu, Ngo, and Tao 2014; Lesyuk et al. 2018)

[13] Simulation technique for computing the scattering of an electromagnetic radiation by metallic nanostructures. The Mie theory is a simulation technique as well as the DDA and many other. These are methods for solving the Maxwell's equations. The choice of the technique to use depends on accuracy, computation time and the range of geometries to which it can be applied.

[14] In the DDA the particle that interacts with an incident light is modelled as an assembly of finite cubic elements. The object is, hence modelled as an array of interacting point dipoles whose polarizability is described by the ε(ω) of the bulk material. This allows to solve the Maxwell's equations and calculate the extinction coefficient C_{ext}. For small particles in a solution the extinction cross section can be considered as the absorption cross section since the scattering is limited. Thus, the Lambert-Beer equation results $A=C_{ext}$ *path length*Concentration. ($C_{ext}= C_{absorption}+ C_{scattering}$, if the scattering contribution it is not negligible it has to be determined by integrating sphere and the absorbance has to be corrected A=1-trasmittance-reflectance).

[15] The DSm has been used setting γ to change with the average diameter, imposing ωp to be independent of the ND volume and ε_∞ as 1. The ε_∞ represents the ion core polarization background and its real value is not known, under the assumption that only valence-band holes may affect the dielectric function it can be considered as 1.

[16] Similar value have been calculated by another group, 1.01×10^{22} cm^{-3}(Hsu, Ngo, and Tao 2014)

With the increase of the aspect ratio the λ_{max} red shifts, the peak width becomes narrower and the intensity grows. The peak width is influenced by size distribution width and by the compositional homogeneity of the ND population.

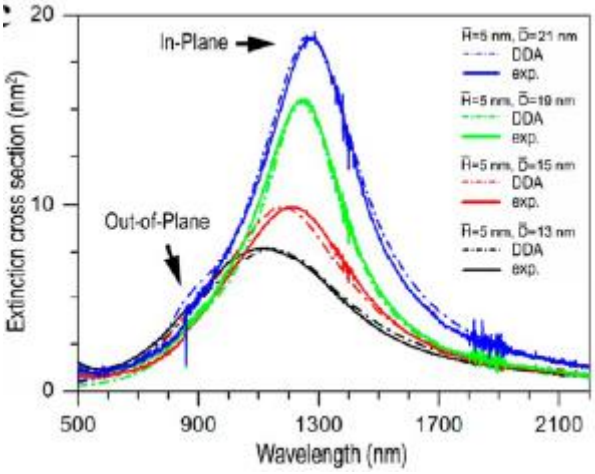

Figure 48: NIR extinction spectra of NDs in CCl4 (continuous lines), along with the corresponding DDA-based fits (dashed lines) (Xie, Carbone, et al. 2013)

<u>$Cu_{2-x}S$ ND LSPR</u>

In contrast with what it is above reported for covellite, which has lattice-constitutional free holes, for the other $Cu_{2-x}S$ species holes result from copper deficiency and are accommodated in crystal phases. Since holes in $Cu_{2-x}S$ experiment the effects of localization they cannot be considered as full free carriers. The result is that the DSm is not suitable to describe their LSPR response. Experimental approaches have been used to indagate the LSPR of $Cu_{2-x}S$ NDs. Chalcocite to digenite $Cu_{2-x}S$ NDs show two broad LSPRs peaks widely separated, the out-of-plane mode LSPR band can be found at lower λ than the in plane-mode band. The experimental results for $Cu_{2-x}S$ NDs have been reported (Hsu, Bryks, and Tao 2012; Hsu, Ngo, and Tao 2014) to follow the Mie theory and Dm expected trends :

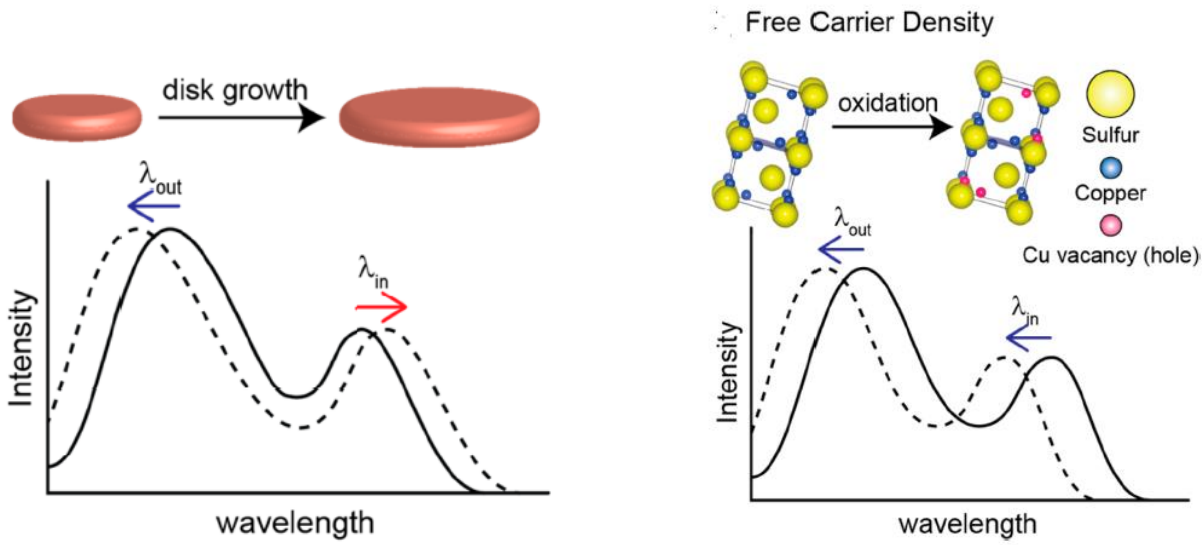

Figure 49: illustration of the expected change of LSPR maximum wavelength for the change of the aspect ratio and of the carrier density, basing on Mie theory and Drude model (Hsu, Bryks, and Tao 2012).

It has to be said that for $Cu_{2-x}S$ NDs the assignation of in plane and out of plane mode to the two peaks is still debated.

Particles interaction in solution

An interface is not necessary for assembly and particles can coalesce in solution for the same interactions that drives the drying mediate assembly. The superstructures formation followed the crystal growth phenomena (Coughlan et al. 2017). Hence, the first step is the formation of a small bundles of NDs that act as nucleation sites which grow for the addition of other NDs that reach them through Brownian motion. With the increase of the dispersion concentration and controlled transition of NCs between the solvents, equilibrium for the incoming NC (to find a site to attach on) can be achieved and stable superlattices can form in the solution. Nanocrystals assembly in solution is speeded up with the addition of an antisolvent (ethanol) but it can occur also in highly concentrated dispersion. Furthermore, the addition of additives as long-alkyl-chain amines led to the formation of complex nanostructures stable solution. This is possible when the size of the additive is larger than nanostructures separation. In this case depletion interactions come into play and when NDs move closer, excluding the additive from the space between them, the local concentration gradient changes, leading to an attractive osmotic pressure that induces the nucleation of NDs in solution followed by growth.

Based on what it is reported by Coughlan et al. NDs of CuS, Cu_2S and $Cu_{2-x}S$ can assembly in solution within a range of 100nm-2µm

Samples' spectra

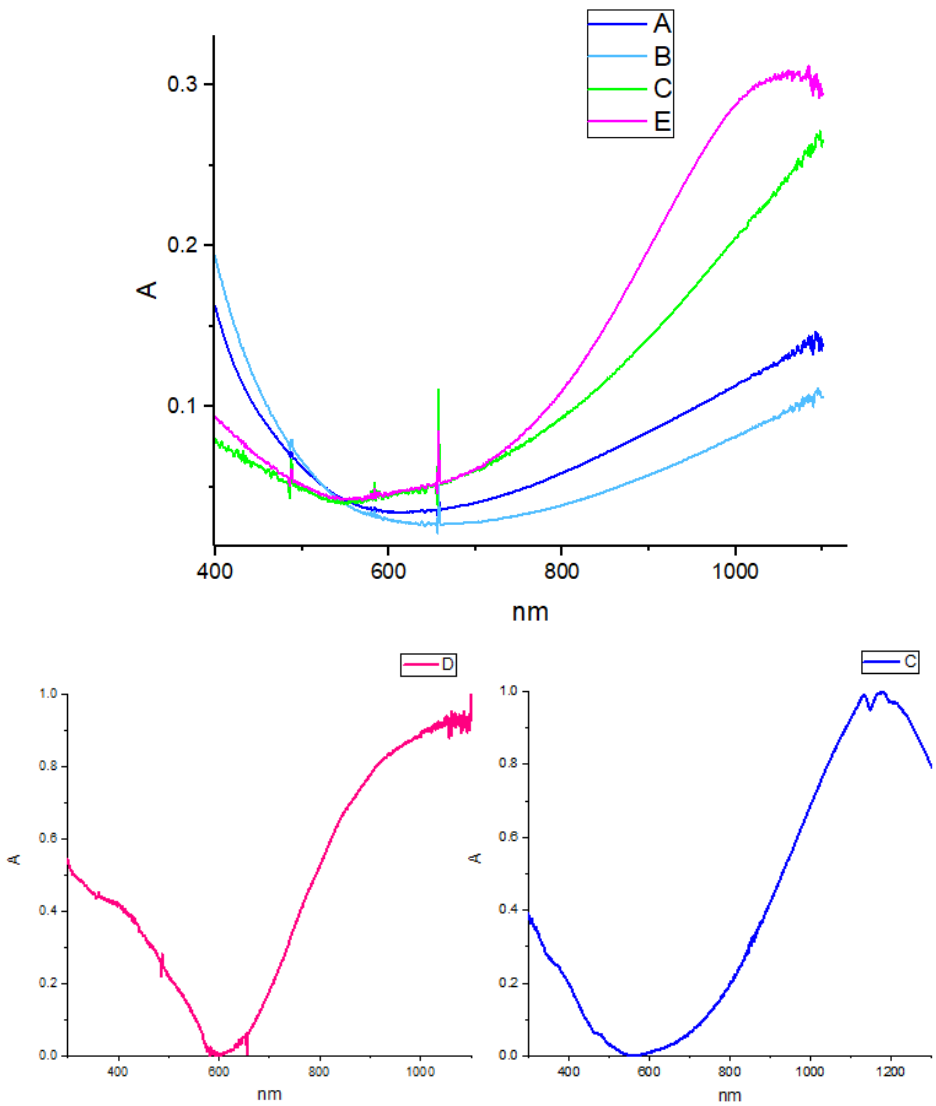

Figure 50: top absorption spectra of sample A,B,C,E at the same (low) concentration; bottom absorption spectra of sample D and full range spectra of sample C

The absorption that occurs in the UV-blue region (below 500 nm) is related to excitonic[17] transitions across a direct band gap which as reported in the introductive part, is influenced by the Moss-Brustein effect.
$Cu_{2-x}S$ with different compositions have different values of λmax of the LSPR band. This has been attributed mainly to the different value of the effective hole mass rather than to the diverse carrier density. With the increase of Cu content in the phase, the effective mass grows[18] and a small change of this value (smaller than carrier density variation) significantly increases the plasma frequency (Hsu, Ngo, and Tao 2014). In the spectra reported in Figure 50 the two LSPR bands of sample A and B are not completely visible in the spectral range achievable and, consequently it is not possible to indagate sample composition with peaks positions. Anyway, for sample A (anilite) and B (djurleite) the phases assigned with XRD patterns are supported by the absorption spectra since sample B shows a lower intensity above the 600nm and the intensity of this signal increases with the increase of x.
Sample C spectrum has been registrest on a wider range and it is fully reported in Figure 50 (bottom). The two bumps at the top of the band are due to the instrumental lamp shift. The LSPR λ_{max} is at 1170nm. It is not possible to compare band width of covellite samples since in the spectral ranges they are not complete, but sample C is expected to have the larger band width based on its larger ratio distribution width. Comparing the signals of sample E and sample C in the region above 500nm the larger width of sample C may be proved. Sample E LSPR band has the λ_{max} at 1059nm. The position of the band, at lower wavelenght than sample C, is in accordance with the lower aspect ratio of sample E.
Sample D spectrum has been reported separately since it is affected by particles aggregation. Since sample D aspect ratio value is smaller than sample C value and bigger than sample E value its LSPR λ_{max} should be between sample C and E. Sample D LSPR band is broad and its deconvolution shows that it is formed by different peaks as reported in Figure 51. Since sample D spectrum has been registered in the same range of sample E its LSPR band should not be completely showed, and the bands generated from the spectrum deconvolution has to be reasonably assigned to particle assembly with diverse dimensions. To investigate the size of the structures formed in solution, a DLS analysis is needed. However, based on what is reported in literature (Chen et al. 2015) when nanodisks form arrays a blue shift of the LSPR peak is expected. The larger is the number of coupled nanodisks in an array, the larger is the resulting blue shift of the LSPR band. Thus, it can be assumed that the large LSPR absorption is due to different contributions (showed in the deconvolution of the spectrum) which are originated from various size NDs arrays. This suggests that sample D has a strong tendency to form assemblies in solution and this is in accordance its IR spectra and narrow distribution.

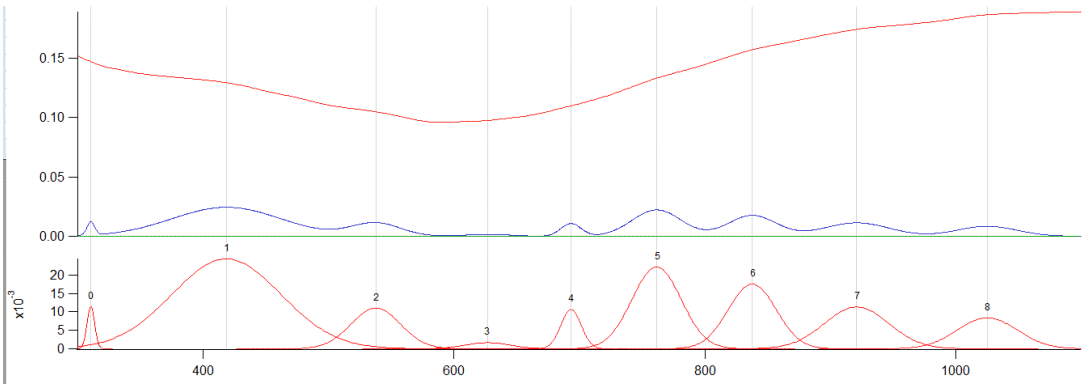

Figure 51: deconvolution of sample D spectra

[17] An exciton is an electrically neutral quasiparticle (as plasmons and phonons), a bound state of an electron and an electron hole which are attracted to each other by the electrostatic Coulomb force. It can transport energy without transporting electric charge.

[18] The effective mass is inversely proportional to the mobility of holes. For $Cu_{2-x}S$ holes that arise from copper vacancies, carrier effective mass is highly dependent on the vacancy density and this is a further complication for their optical modelling. Furthermore, when copper vacancies are responsible of hole density it is difficult to distinguish between contributions from shape effects and carrier density to the LSPR.

A comparable behaviour is showed for highly concentrated solutions for which, with the increase of the concentration, the LSPR peak shifts at lower λ and its intensity decreases, as it can be seen in Figure 52.This is reported for coupled nanodisks in arrays.

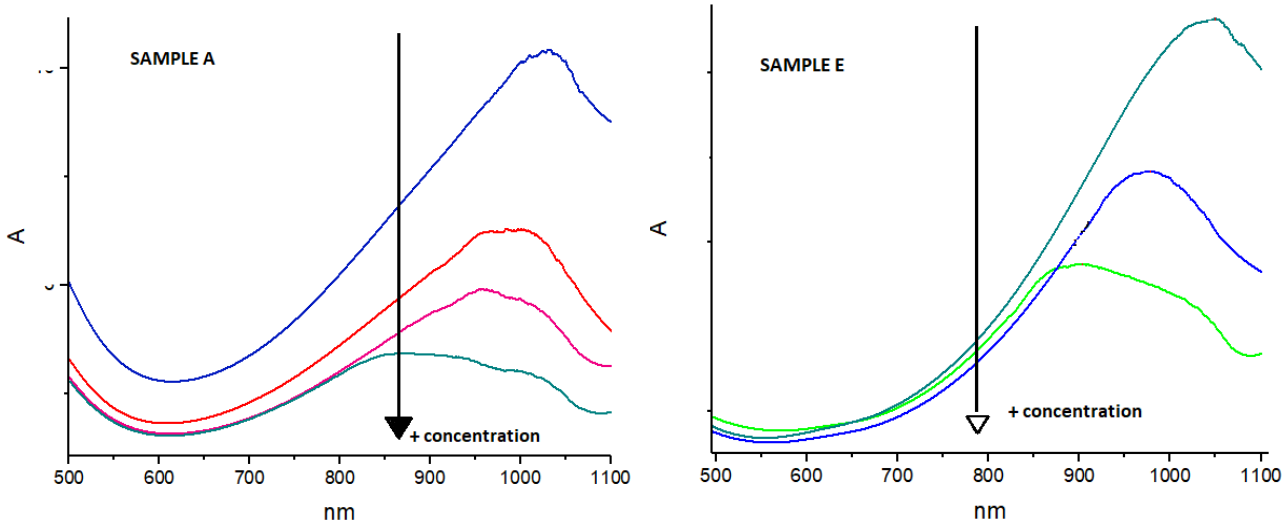

Figure 52: spectra of highly concentrated solutions of sample A and sample E. The curves are referred to a unitary concentration in order to highlight the intensity decrease.

These spectra highlight the importance of using diluted solutions to register the absorption spectra.

Synthesis of copper sulphides nanoparticles through a green approach

Nanoparticles of copper sulphides (CuS-NPs) with three different organic ligands: cetyl trimethylammonium bromide (CTAB), trisodium citrate (CIT) and poly acrylicacid (PAA), have been synthetized through a one-pot approach in aqueous solution. Indeed, in order to apply nanoparticles in biomedical applications a key challenge is to obtain reproducible, monodisperse and colloidal stable nanoparticles in the minimum number of steps. The use of water as solvent is in favour in many respects since it is low cost, widely available, environmental benign and it is the solvent of biochemical reaction in nature and therefore it is biocompatible. The acronym CuS-NPs is used to refer to particles obtained with this approach besides the fact that only using CTAB as organic ligand it has been possible to identify the particle phase which is covellite.
The CuS-NPs synthesis foresees 3 steps. At first $CuCl_2$ solution is mixed with organic ligand, then sodium sulphide is added producing a brown-yellowish solution that turned green with heating the reaction vessel.
The brown-yellowish solution owes its colour to the presence of $Cu_{2-x}S$ NPs which with heat (that speeds up the reaction) converts into CuS changing the colour into deep green.
The reaction that leads to the formation of copper rich NPs is:
$2\ Cu^{2+}_{(aq)} + 2S^{2-}_{(aq)} \longrightarrow Cu_2S{*}S^0_{(s)}$
Considering Cu_2S which is the first composition of NPs, and therefore it is considered to describe the reaction occurring in solution (Kore, Kulkarni, and Haram 2001; Silverstein, Webster, and Kiemle 2015).
The transformation from Cu_2S to CuS involves the disproportion of Cu^{+1} to Cu^0 and Cu^{2+} with an electron transfer between them through an empty available surface state, indicated as () (Kore, Kulkarni, and Haram 2001).
$Cu^{+1}Cu^{1+}S^{2-} + (\ ) \rightleftarrows Cu^{1+}\ Cu^{2+}S^{2-} + (e\text{-}) \rightarrow Cu^0Cu^{2+}S^{2-+} + ()$

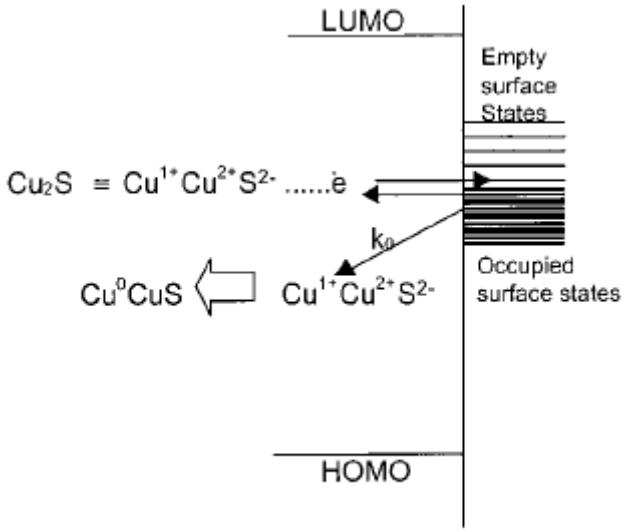

Figure 53: illustration of the reaction assisted by surface states

The presence of ligands influences the rate of the conversion into covellite since these molecules can absorb on the surface.

CuS-NPs synthetic protocols

Batch solutions

Batch solutions of $CuCl_2 \cdot 2H_2O$, 2 mM and $Na_2S \cdot 9H_2O$, 100 mM have been prepared in water. Sodium sulphide has been kept in the fridge and used within one week.

CuS-CIT citrate

25 mL of 2 mM copper solution is put into a 50 mL three neck round bottom flask alongside with 8.8 mg of trisodium citrate di-hydrate. The obtained solution is stirred at room temperature for 5 minutes and then 0.5 mL of a 100 mM Na_2S solution is added. The mixture turns brown-yellowish, it is stirred at room temperature for 10 minutes before rising the temperature to 90 °C and then leaving the reaction vessel at this temperature for 20 minutes: during this time the colour turns deep green. Finally, the heating and the stirring are stopped, and the reaction is quenched in cold water and then transferred to a vial and stored in fridge.

CuS-CTAB Cetyl trimethylammonium bromide

25 mL of 2 mM copper solution is putted in a 50 mL three neck round bottom flask alongside with 6.3 mg of CTAB. The obtained solution is stirred at room temperature for 5 minutes and then 0.5 mL of a 100 mM Na_2S solution is added. The mixture turns brown-yellowish, it is stirred at room temperature for 15 minutes purging the flask from air with a gentle argon flow before rising the temperature to 90 °C and then leaving the reaction vessel at this temperature for 60 minutes: during this time the colour turns deep green. Finally, the heating and the stirring are stopped, and the reaction is quenched in cold water and then transferred to a vial and stored in fridge.

CuS-PAA-Poly(acrylicacid)

25 mL of 2 mM copper solution is put in a 50 mL three neck round bottom flask alongside with 15 mg of PAA (MW=450'000). The obtained solution is stirred at room temperature for 10 minutes and then 0.5 mL of a 100 mM Na_2S solution is added. The mixture turns brown-yellowish, it is stirred at room temperature for 10 minutes before rising the temperature to 90 °C and then leaving the reaction vessel at this temperature for 20 minutes: during this time the colour turns deep green. Finally, the heating and the stirring are stopped, and the reaction is quenched in cold water and then transferred to a vial and stored in fridge.
Purification procedures are described below for each CuS- NP.

CuS-CIT ligand trisodiumcitrate

In order to evaluate the reproducibility of the protocols, three samples have been prepared and are reported as CIT1, CIT2, CIT3.For the DLS and FT-IR analysis only one sample has been measured.

XRD

XRD patterns have been obtained from purified NPs as described below in the purification paragraph. For CuS-CIT NPs there are not clearly visible peaks in the diffraction spectra. This is due to the presence of different diffraction domains within particles (which can be seen in HRTEM images) and therefore, since they are smaller than the whole particle the peaks, following Scherrer's equation, are broad. For this reason, from the patterns the phases of the crystals cannot be precisely allocate.

CIT1, CIT2, CIT3 have been measured with the Philips XPert diffractometer, only CIT2 has been measured with D8 Advance Bruker instrument in Bragg-Brentano mode. XRD calculated pattern of the hexagonal covellite, which is the expected phase, match two peaks at 2θ of 48 and 31, while the peak at 45 could be due to the presence of digenite as impurity phase as reported by Marin et al.

The Scherrer analysis performed on (110) reflection gave a crystallite diameter of 6.9±0.7 nm.

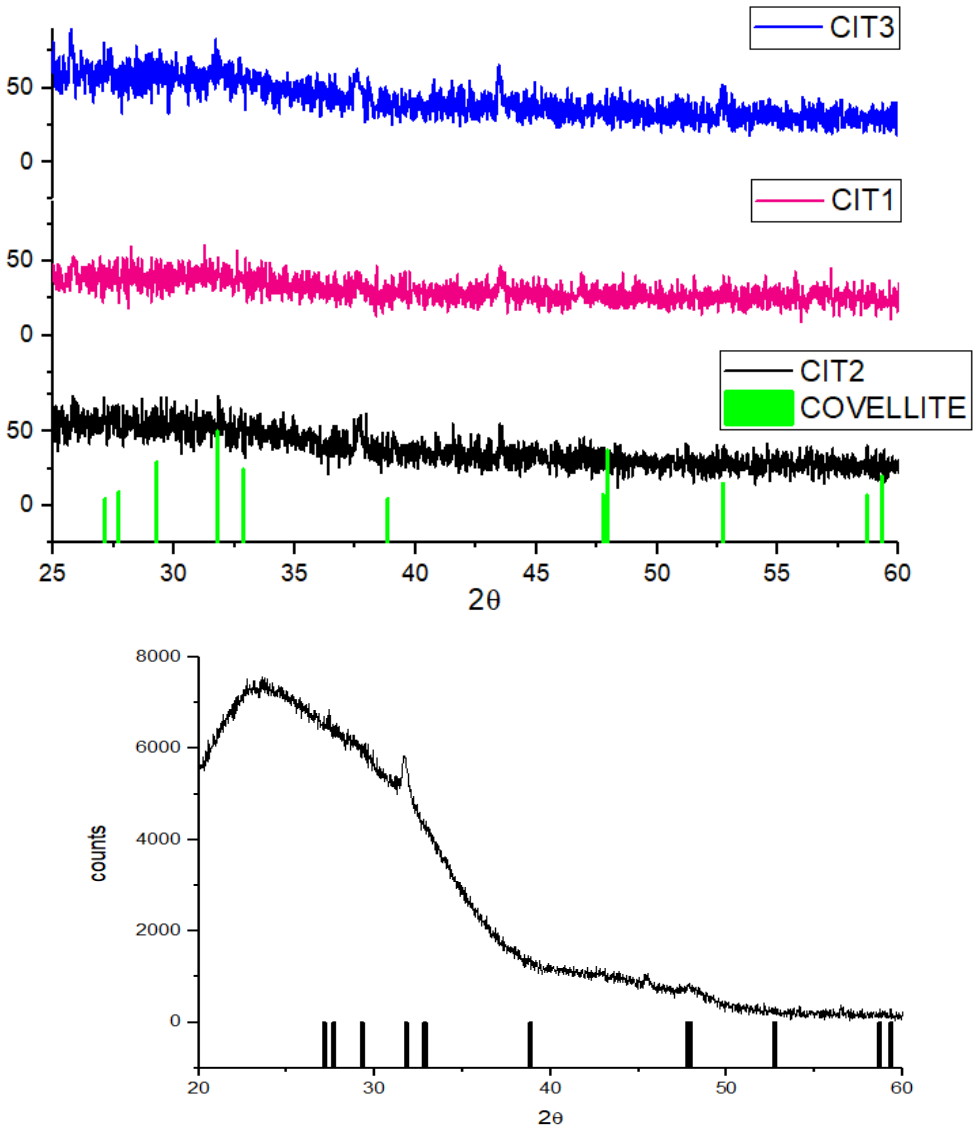

Figure 54: above, XRD patterns of CIT1, CIT2, CIT3 in comparison, below the most useful XRD pattern registered with D8 Advance Bruker instrument in bragg-brentano mode. Below sample XRD pattern reference sticks of hexagonal covellite are reported in black

TEM

The solution obtained as described in the CuS-CIT NPs protocol needs to be purified (as described below) for TEM grids preparation thought drop casting.

CuS-CIT NPs of CIT1, CIT2, CIT3 samples are showed in the following TEM images. From TEM images it can be said that for different samples, NPs have similar dimensions and morphology. In the samples there are small nearly-spherical particles with ~6nm of diameter, rod-like particles which are the nanodisks sitting on their edges. There are hexagonal nanoparticles with size of about 6 nm and few NDs having bigger sizes along with triangular shaped particles with rounded edges. There are hexagonal particles with size comparable with those of spherical nanoparticles and few bigger than these[19] along with triangular shaped particles with rounded edges.

For the determination of particle size, round and hexagonal particles have been considered, and since a large part of the population presents 2 different diameters (hereinafter referred to as longer and shorter lengths) due to the irregular hexagonal shape and to the more oval than round shape of particles, both have been measured.

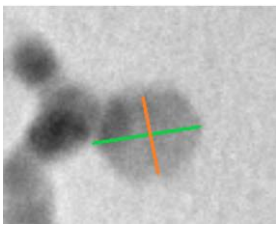

Figure 55: TEM image of an anisotropic particle. The green line is the longer length while the orange one is the shorter length

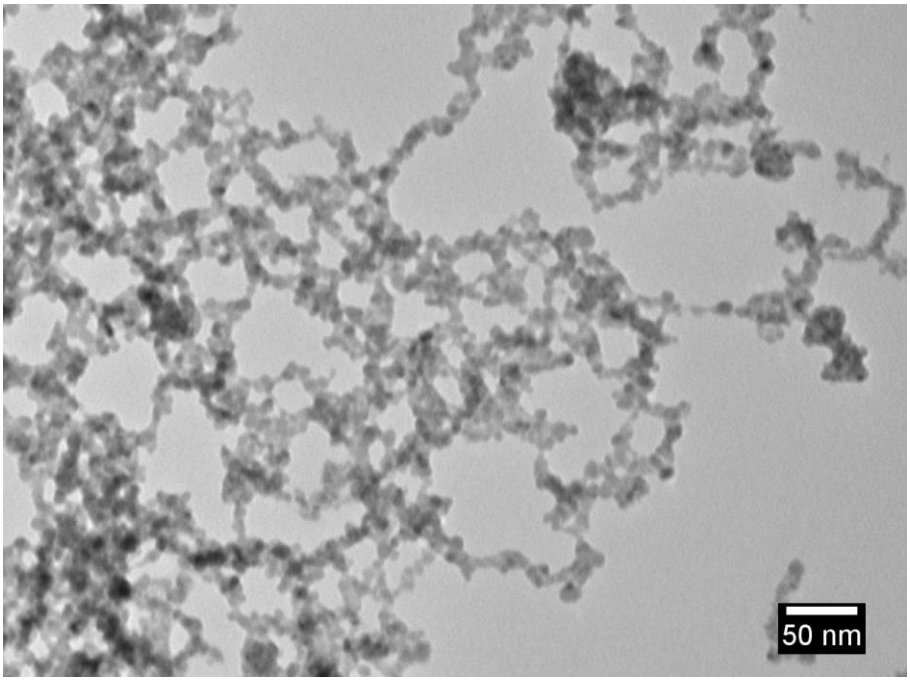

Figure 56: TEM image of CIT1

[19] Since the number and the dimension of the bigger particles is strongly affected by the area showed by the TEM images these have not been take into account during NPs dimension measurement.

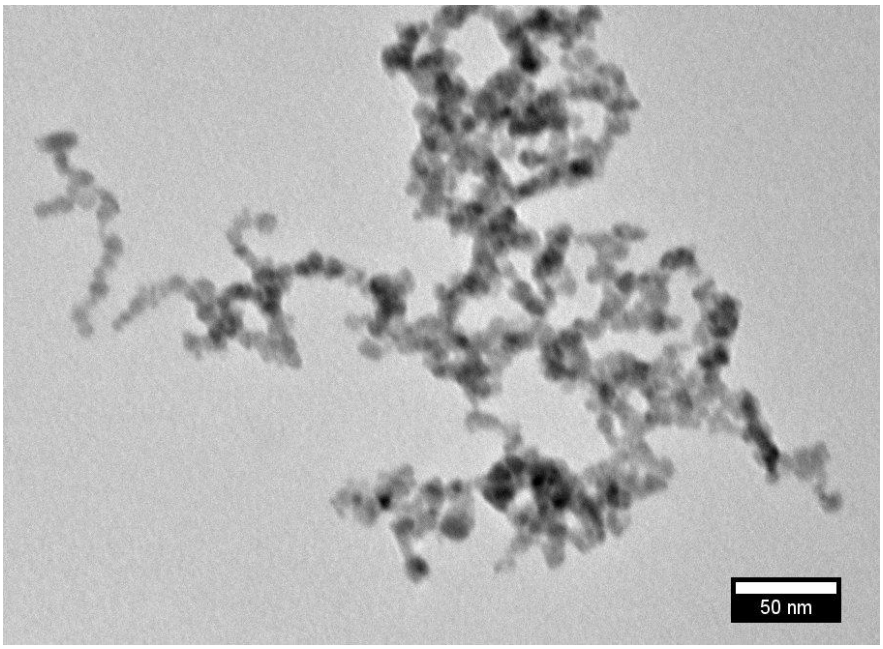

Figure 57: TEM image of CIT2

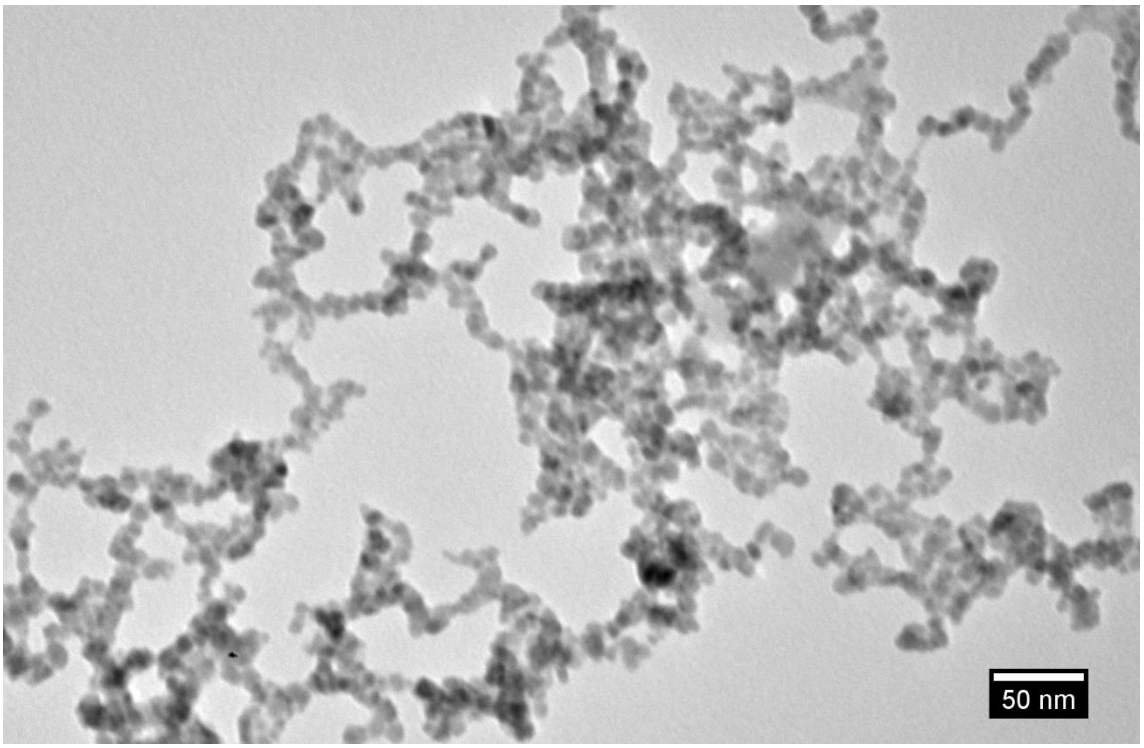

Figure 58: TEM image of CIT3

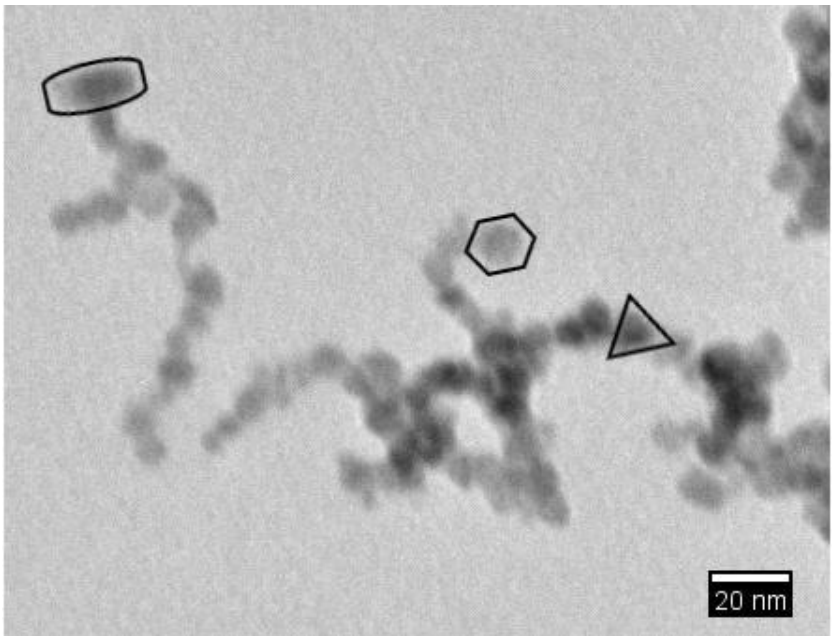

Figure 59:TEM image in which particles with different morphology and comparable dimensions are highlighted

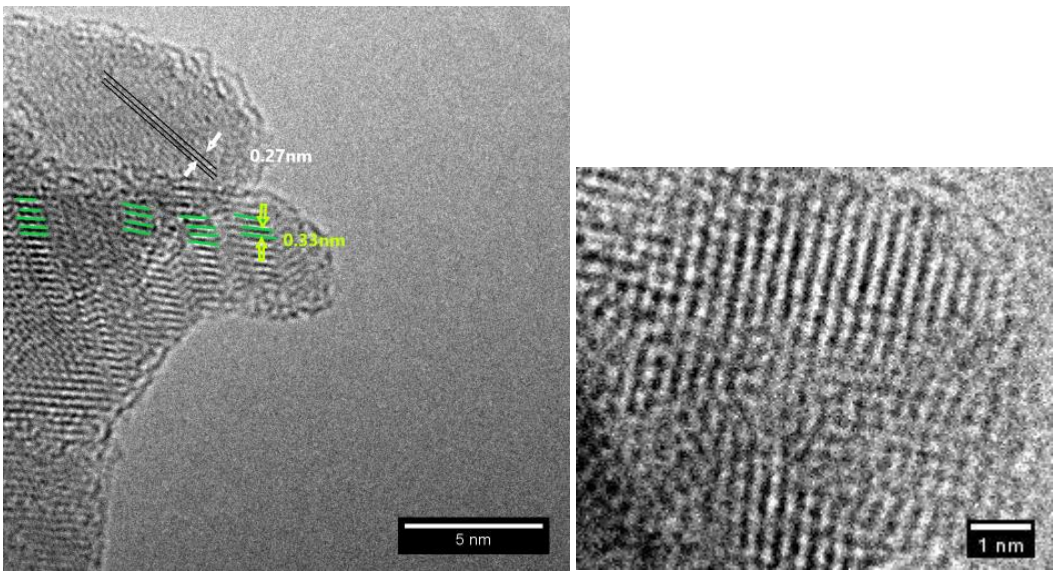

Figure 60: HRTEM of CuS-CIT NPs. On the left, the black lines highlight the (006) planes while the green lines highlight the (100) planes .The image of a single particle composed by different crystalline domains is reported on the right

From HRTEM images it can be seen that single particles are composed by different crystalline domains.

CIT1 and CIT2 sizes are not significantly different while CIT3 average size is a bit larger. All three samples have the same average ratio and therefore particles shapes are averagely the same.
As it can be seen in Figure 63 longer and shorter lengths have similar distribution patterns. CIT2 has the narrower distributions. The larger ratio and shorter length distributions of CIT3 suggest that the bigger the particles are the more anisotropic they are.

Table 5: CIT1, CIT2, CIT3, parameters determined from TEM images

sample	parameter	Value (nm)	Minimum value (nm)	Maximum value (nm)
CIT1	Longer length	9 ± 1	6.0	16.1
	Shorter length	8.2 ± 0.8	5.8	14.0

	ratio	1.19 ± 0.06	1.01	1.55
CIT2	Longer length	9.2 ± 0.8	6.3	13.2
	Shorter length	7.8 ± 0.7	5.3	11.9
	ratio	1.19 ± 0.05	1.01	1.49
CIT3	Longer length	10.4 ± 0.8	6.5	15.0
	Shorter length	8.9 ± 0.8	5.4	14.0
	ratio	1.20 ± 0.02	1.02	1.76

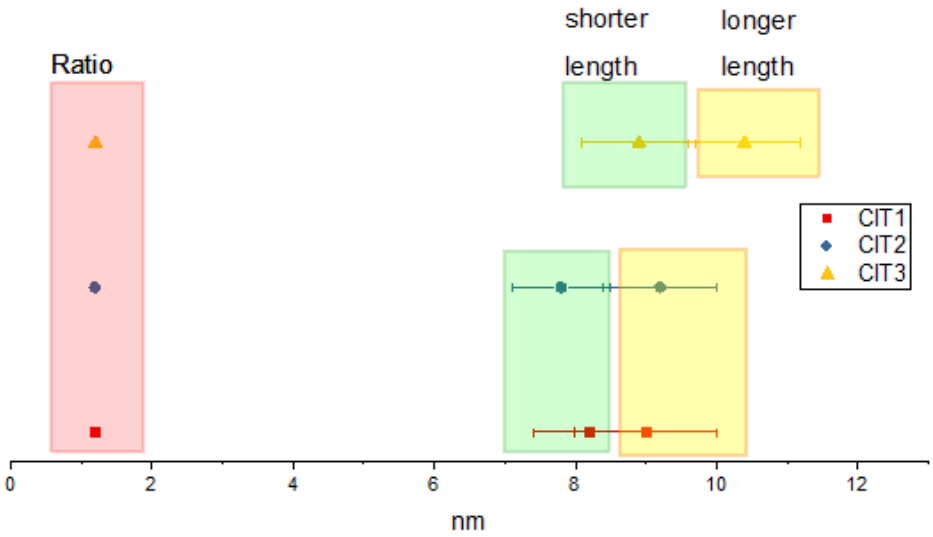

Figure 61: graphical illustration of the values reported in Table 5.. Shorter lengths are reported inside the green box, ratios (longer length/shorter length) are reported inside the red box and longer lengths are reported inside the yellow box

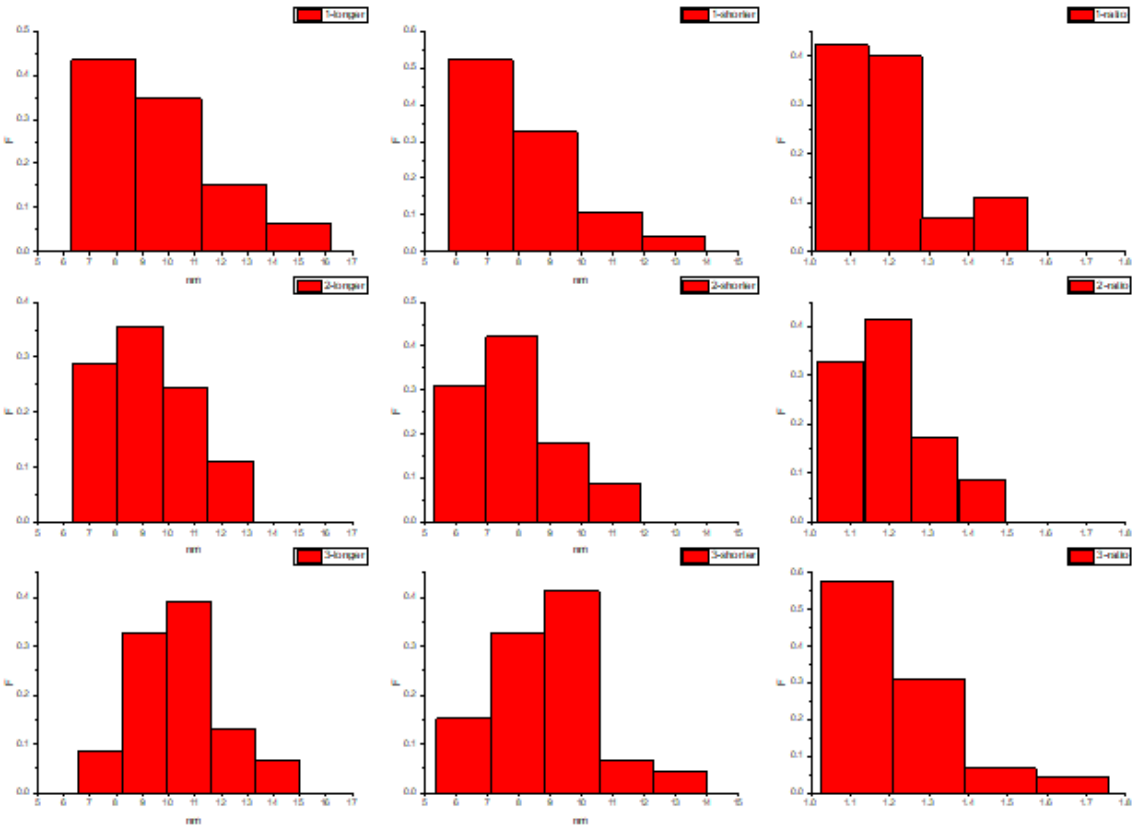

Figure 62: distributions of parameters reported in Table 5. Longer lengths, shorter lengths and the ratio (longer/shorter) are reported from left to right in each row which correspond from the first to the third row to CIT1,CIT2,CIT3.

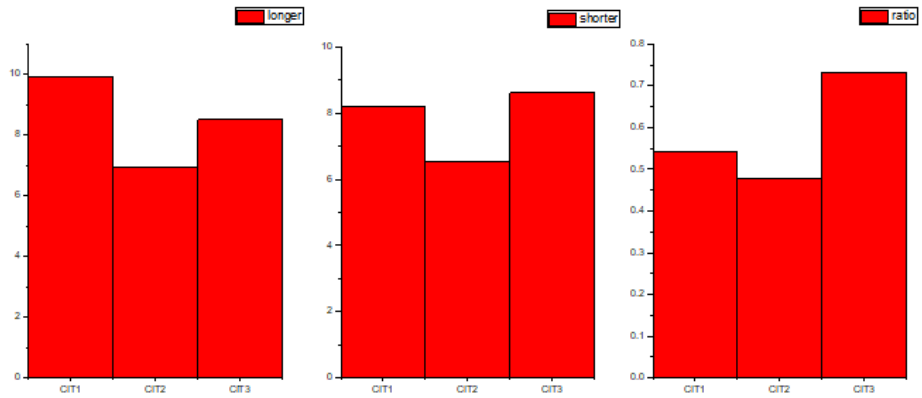

Figure 63: graphical illustration of distribution widths of values reported in Table 5, from right to left: longer length, shorter length and ratio of CIT1, CIT2, CIT3.

FT-IR

CuS-CIT NPs has been purified as described below in the purification paragraph. After desiccation, precipitate NPs (during the purification) have been mixed with KBr to prepare the pellet. The purification is needed to remove the non-bonded organic ligand which otherwise would cover the less intense signal of the bonded ligand.

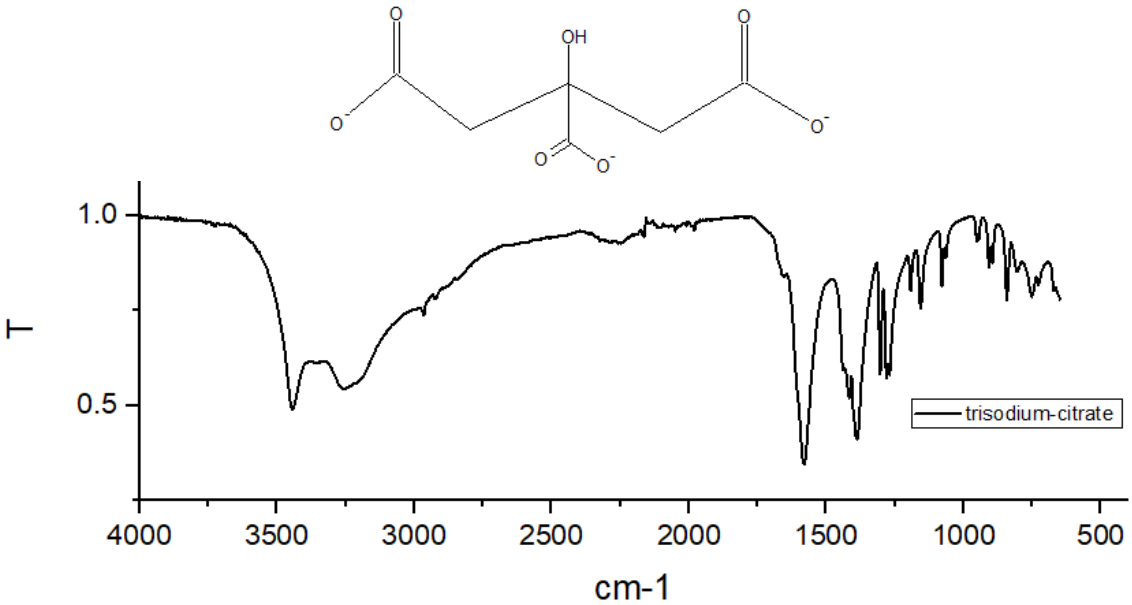

Figure 64:above illustration of citrate molecule, below IR spectra of trisodium citrate di-hydrate

Table 6: expected bands for citrate

	Band position (cm^{-1})
ν(OH)	3450
ν (CH)	2850-3000
ν($-CO_2^-$)	1582-1385
δ(CH)	1350-1480
ρC(=O)-O	~425

The broad band at ~3240cm^{-1} in the spectra of citrate is due to crystal water.

The amount of citrate bounded to particles is low and therefore bands intensities are low. For this reason, the spectrum of the sample has been split to show the three ranges so that to make bands visible.

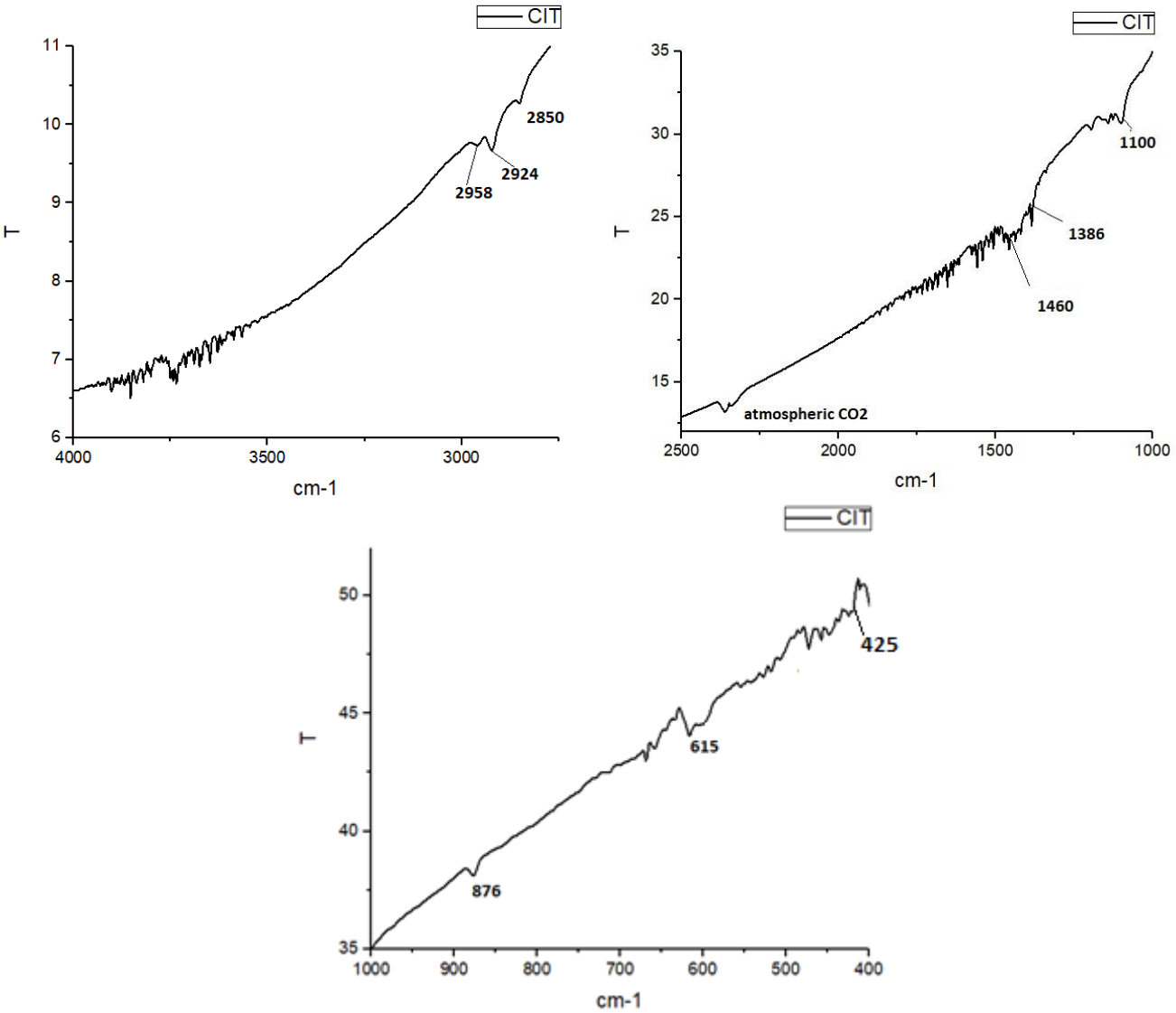

Figure 65: IR spectra of CuS-CIT NPs reported into 3 ranges

In the first part of the spectra, bands of v(CH) are present while there is not any signal of the OH group. In the second part of the spectra, common bands to both NDs and CuS-NPs are present, namely the signals between ~1800-1400 cm^{-1} and the sharp band at 1100cm^{-1}. These bands are evidences of the presence of a thin organic layer that allows the interaction between light and particles core. In the multiple narrow signals region two bands can be seen, a broad one at ~1460cm^{-1} and a sharp one at 1386 cm^{-1}. The broad band at ~1460cm^{-1} can be assigned to v(C=O) which is the most intense band expected in citrate spectrum. Compared to free citrate spectrum this band is shifted to lower wavenumbers and it is broader. In the third part of the spectrum the band at 425cm^{-1} can be assigned to ρC(=O)-O.

The absence of some bands and the changes of positions and shapes of other ones due to carboxylic and hydroxylic groups, prove that citrate bonds the particle through these groups. Furthermore, the spectrum of CuS-CIT NPs suggests that, after the purification only ligand molecules directly bonded to particles form the organic layer.

DLS analysis

An average diameter of 22 nm has been measured for CuS-CIT NPs in solution. It can be considered compatible with the value determined by TEM images taking hydrodynamic radius into account. Since the Pdl value determined is 0.489 the sample is averagely polydisperse. It has to be considered that the sample was one month old when it has been measured and therefore a certain aggregation between particles might have influenced this analysis.

(Distribution by number has been obtained knowing that the CuS-CIT NPs refractive index is 2.2)

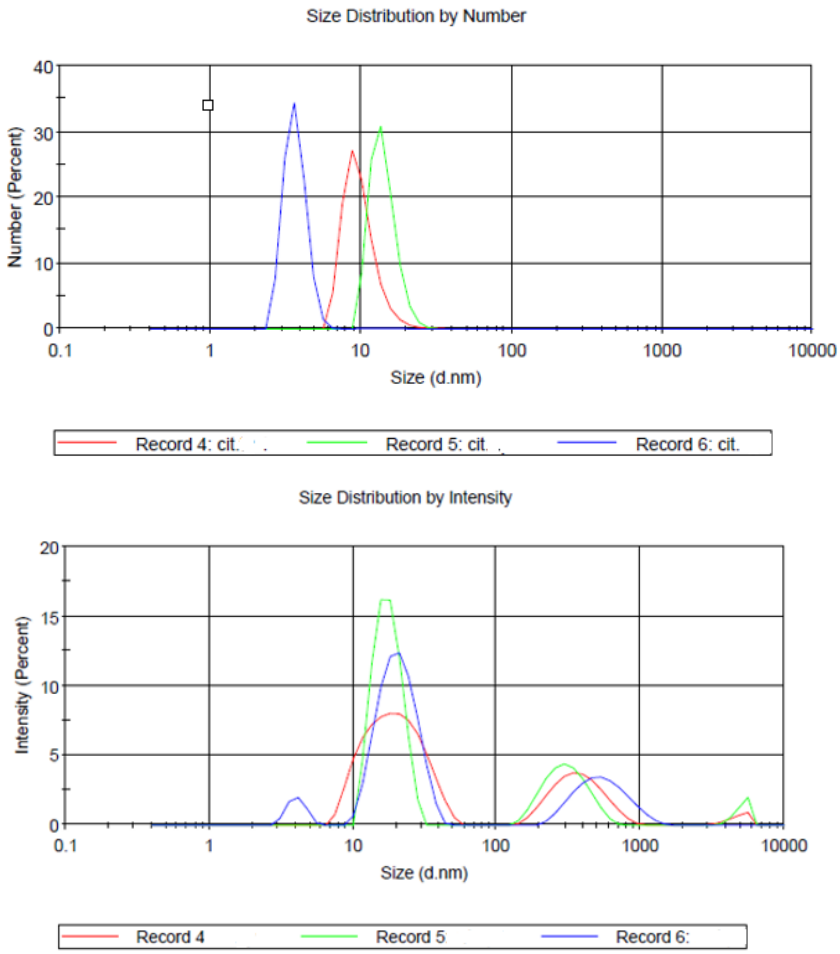

Figure 66: size distribution by number (top) and by intensity (bottom) graphs

UV-VIS Spectroscopy

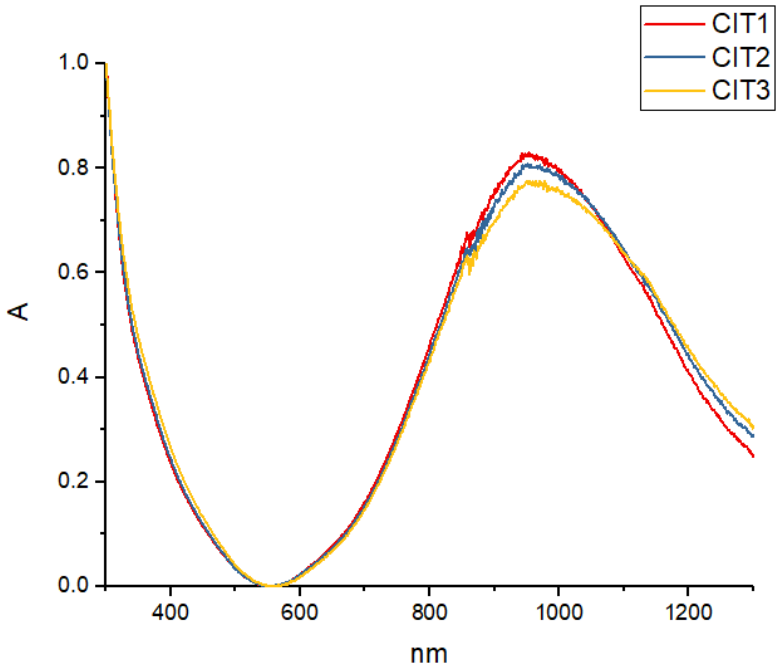

Figure 67: CIT1, CIT2, CIT3 absorption spectra.

Table 7: λ_{max} value of LSPR bands

sample	λmax (nm)
CIT1	953
CIT2	957
CIT3	951

All three sample absorption spectra have a comparable shape and λ_{max}.

Purification

Purification allows to isolate particles from the reaction solution and therefore to remove unreacted reagents and un-bonded ligands from NPs. To remove the particles from the solution at the end of the reaction, these are precipitated through centrifugation together with an anti-solvent. The so obtained precipitate has been used for preparing XRD samples; while two further purification steps are necessary for preparing TEM grids in order to achieve good images. Also, for preparing KBr pellet to acquire the IR spectrum, CuS-CTAB NPs have undergone two purification steps. Before the second purification step the precipitate obtained with the first centrifugation step has been re-disperse in solution.
Different conditions are required depending whether centrifuge (8000rpm, 15 ml Falcon) or ultracentrifuge (1400, 2 ml Eppendorf) is used.

Table 8: purification conditions

1° purification step			**Result of the 1° purification**	
Anti- solvent	**Sample/ solvent**	**Time 8000rpm Time 14000rpm**	**deposit**	**Supernatant solution**
isopropanol	1 / 3	40 min Falcon 20min Eppendorf	Stuck to the walls of the Falcon/ in the bottom of the Eppendorf	Light green

2° purification step	Solvents to re-disperse NPs	Volume of solvents	Time	Solvents for final redispersion
800 rpm (Falcon)	Water+ isopropanol	250 µl + 250 µl	40 min	Water/isopropanol
14000 rpm (Eppendorf)	Isopropanol	2 ml	20 min	Water/isopropanol

After the purification (especially after 2 steps) a bit of water is necessary to re-disperse the particles.
The fact that, after the purification (1 step), the particles are aggregated has been proved by DLS made on a purified sample having an average diameter of 93.0 nm (PdI = 0.222).

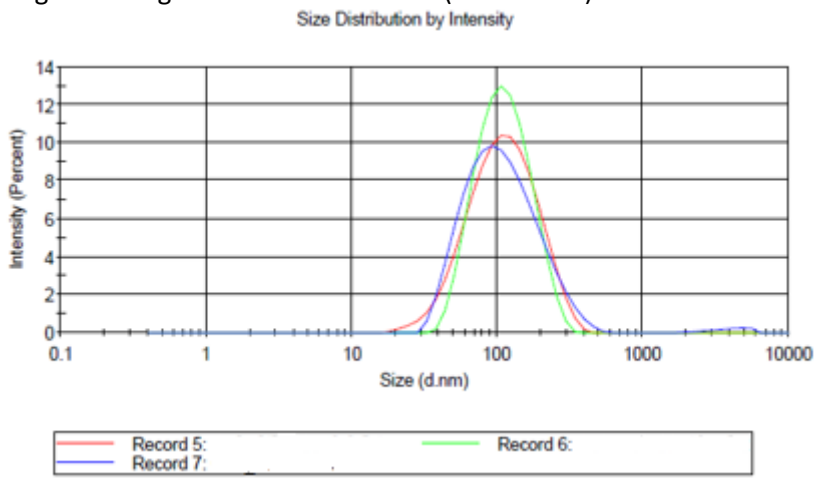

Figure 68:size distribution by intensity of a CuS-CIT NPs purified sample

CuS-PAA ligand polyacrylic acid

In order to evaluate the reproducibility of the protocols, three samples have been prepared and are reported as PAA1, PAA2, PAA3.For the DLS and FT-IR analysis only one sample has been measured.

XRD

All three samples have been used without any purification for preparing XRD samples but PAA1 has been measured also after two purification steps, as described below in the purification paragraph.
PAA1, PAA2, PAA3 have been measured with the Philips XPert diffractometer and only one sample has been measured with D8 Advance Bruker instrument in Bragg-Brentano mode.
All XRD patterns show an intense peak at ~31.8 which matches with the (103) reflection of covellite. In the XRD pattern of non-purified PAA1 there are two peaks at 28.7 and 45.7 which are not present in the pattern of purified PAA1. This suggest that these two peaks might be due to un-reacted salts in the reaction solution. These peaks can be seen also in the PAA2 XRD pattern where they have a low intensity, and in the pattern recorded with the D8 Advance Bruker instrument. Because of the high level of similarity between different phases of $Cu_{2-x}S$, the numerous possible salts derived from the reaction environment and the poor quality of XRD patterns it has not been possible to assign these two peaks, but it can be said that, probably, both digenite phase impurities (basing on what reported in literature) and salts contribute to them.

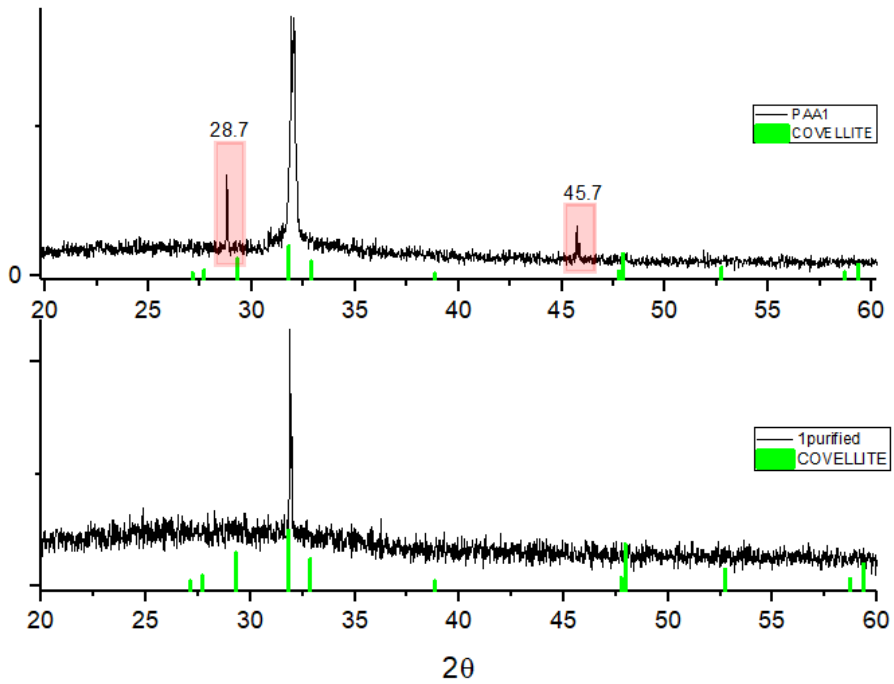

Figure 69: XRD pattern of purified (bottom) and non-purified (top) PAA1 with reference pattern of hexagonal covellite in green.

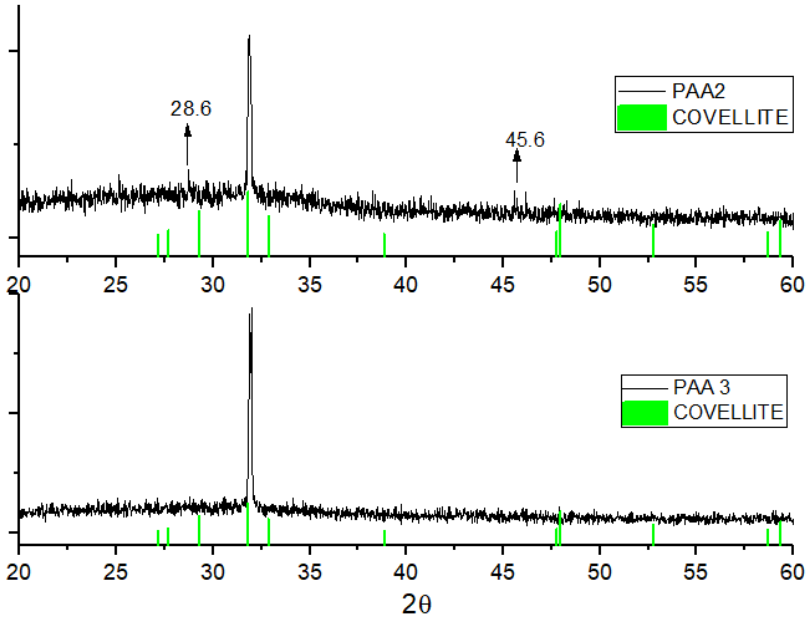

Figure 70: XRD pattern of non-purified (top) PAA2 and (bottom) PAA3, with reference pattern of hexagonal covellite in green.

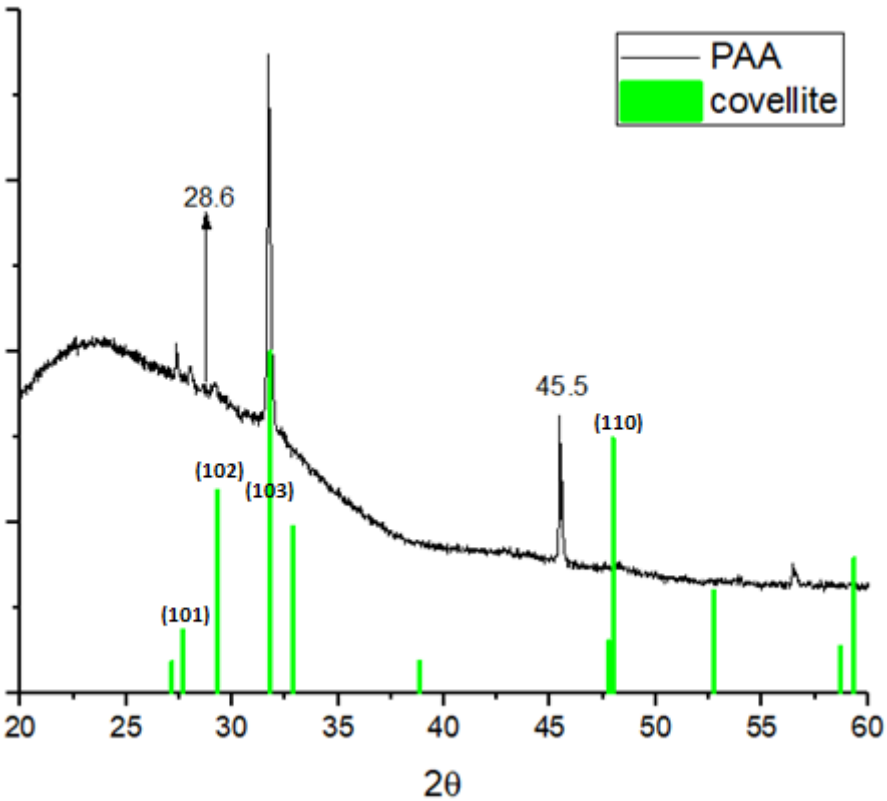

Figure 71: XRD pattern registered with D8 Advance Bruker instrument in Bragg-Brentano mode with reference marks of hexagonal covellite in green.

As can be seen in Figure 71 the XRD patterns matches covellite (102), (101), (110), (103) reflections. The reflection (110) was used in the Scherrer equation to determine the diameter, which has been calculated to be of about 9 ± 1 nm.

In conclusion, based on XRD analysis, the presence of covellite phase can be confirmed in CuS-PAA NPs samples. Nevertheless, other impurity phases might be present.

TEM

The solution obtained as described in the CuS-PAA protocol needs to be purified (as described below) for preparing TEM grids. As described below in the purification paragraph, CuS-PAA Nps purification is hard to achieve and it is proved by the PAA layer present in TEM images.

Different samples have similar NP dimensions and morphology. In TEM images, NPs with size ranging from ~4 to 22nm can be seen. Particles morphologies are the same reported for CuS-CIT NPs and therefore particles with truncated triangular, hexagonal and rod-like shape are present; the smaller particles have, in the majority of cases, nearly-spherical shape.

To assess particle size, the longer and shorter lengths of spherical and hexagonal particles have been measured.

In HRTEM images it can be seen that single particles are composed by different crystalline domains.

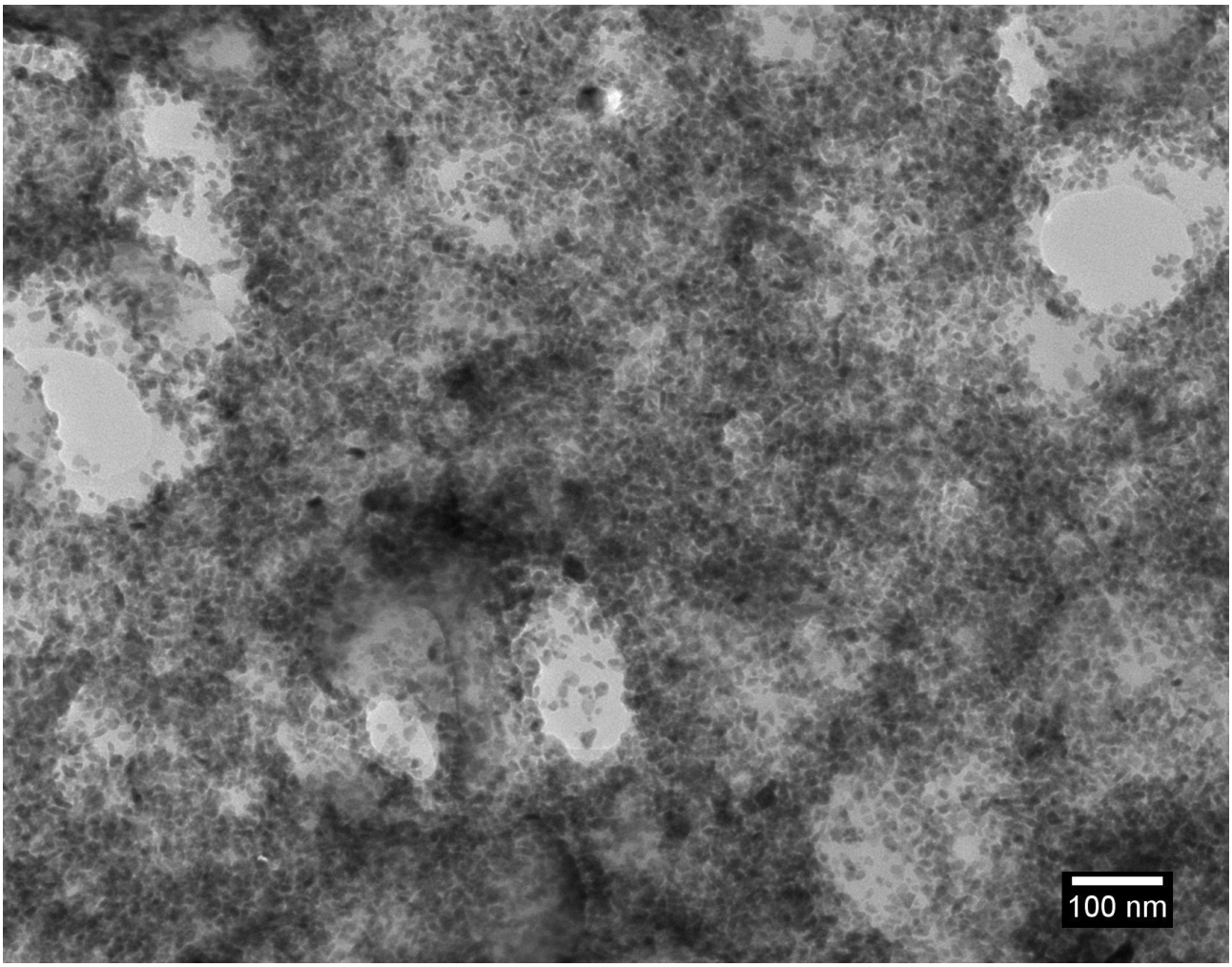

Figure 72: TEM image of PAA1

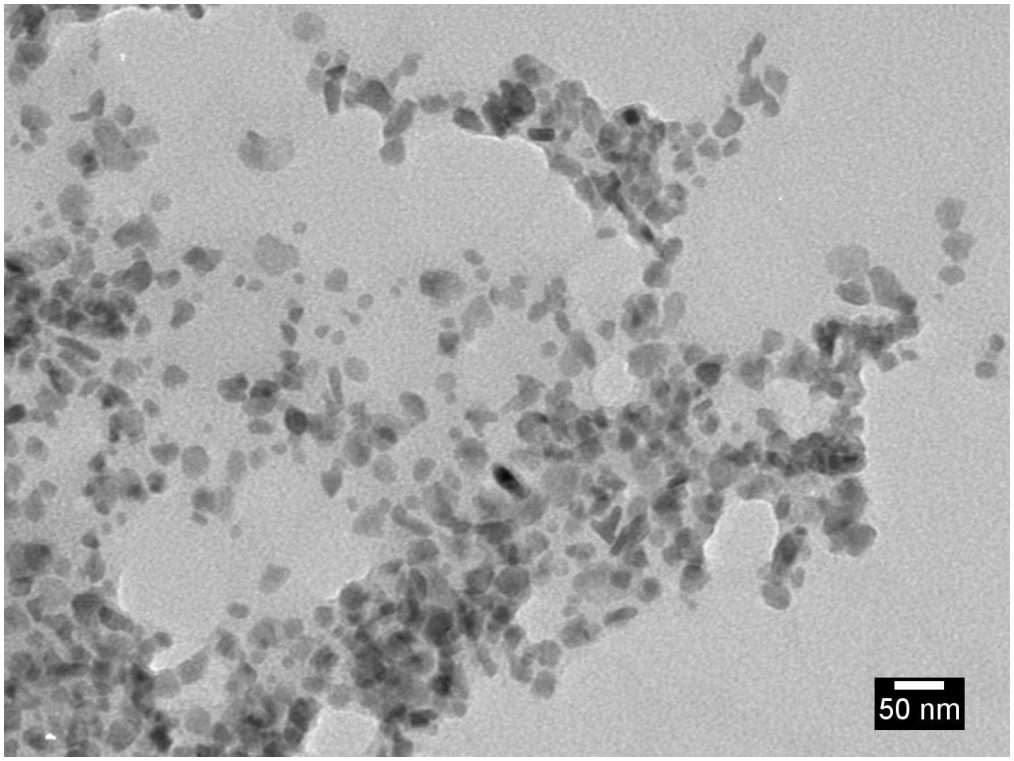

Figure 73: TEM image of PAA2

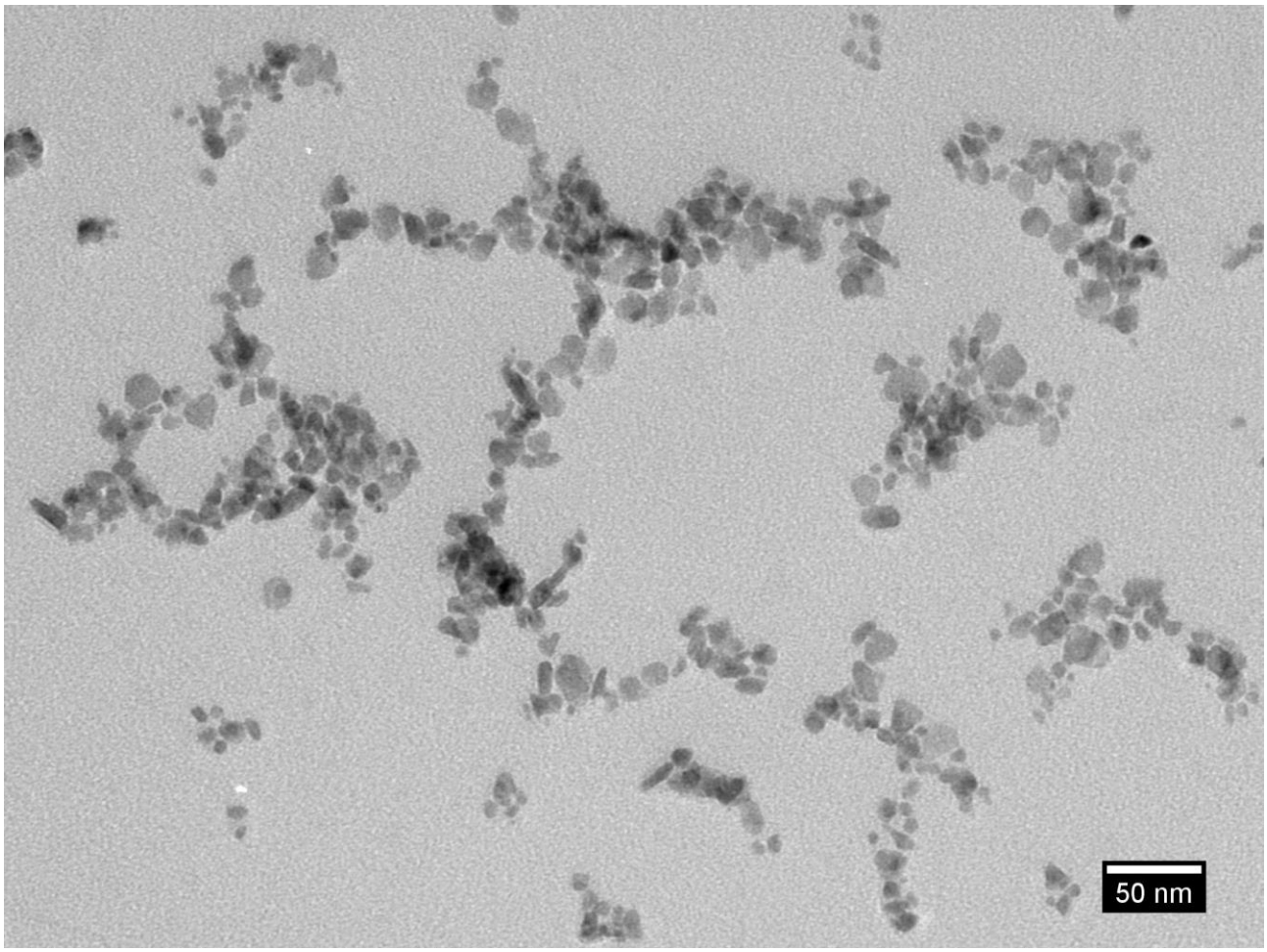

Figure 74:TEM image of PAA3

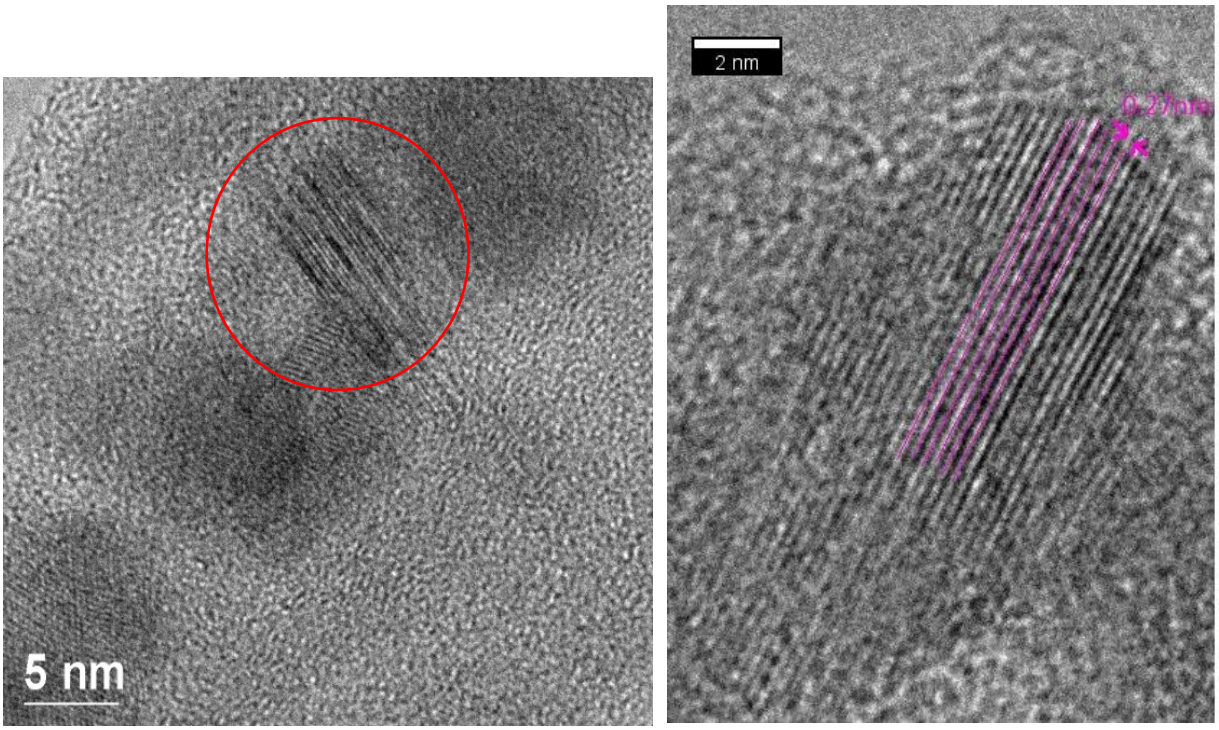

Figure 75: HRTEM image of CuS-PAA NPs. On the left the red circle highlight a ND, on the right the spacing of a NDs edge has been measured. It is equal to 0.27 nm corresponding to (006) plane of covellite suggesting the growth perpendicular to the c-axis.

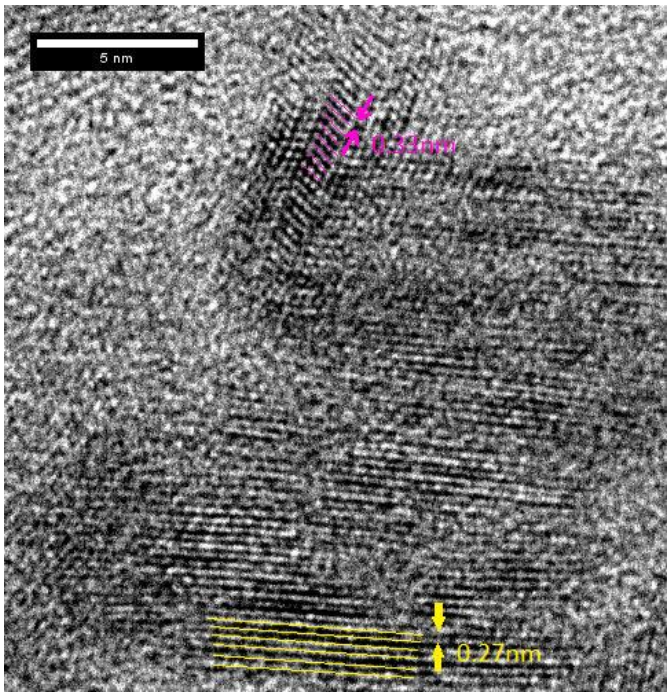

Figure 76:HRTEM of CuS-PAA NPs where the spacing of 0.33 nm corresponding to the (100) plane and 0.27nm corresponding to the (006) plane of covellite are evidenced.

NPs longer length of three samples are comparable while the shorter length of PAA3 is a bit smaller compared to the ones of other samples. All tree samples have comparable average ratio and therefore particles shapes are on average the same. As can be seen in Figure 78, longer and shorter lengths have similar distribution patterns.

Table 9: PAA1,PAA2,PAA3, parameters determined from TEM images

sample	parameter	Average value (nm)	Minimum value (nm)	Maximum value (nm)
PAA1	Longer length	13.0 ± 1	4.3	29.7
	Shorter length	11 ± 1	3.8	27.3
	ratio	1.23 ± 0.04	1.00	1.65
PAA2	Longer length	13.8 ± 0.8	5.3	22.3
	Shorter length	11.4 ± 0.2	4.9	21.6
	ratio	1.22 ± 0.04	1.00	1.88
PAA3	Longer length	12 ± 1	6	22
	Shorter length	9.5 ± 0.8	4.1	18.3
	ratio	1.29 ± 0.05	1.02	1.88

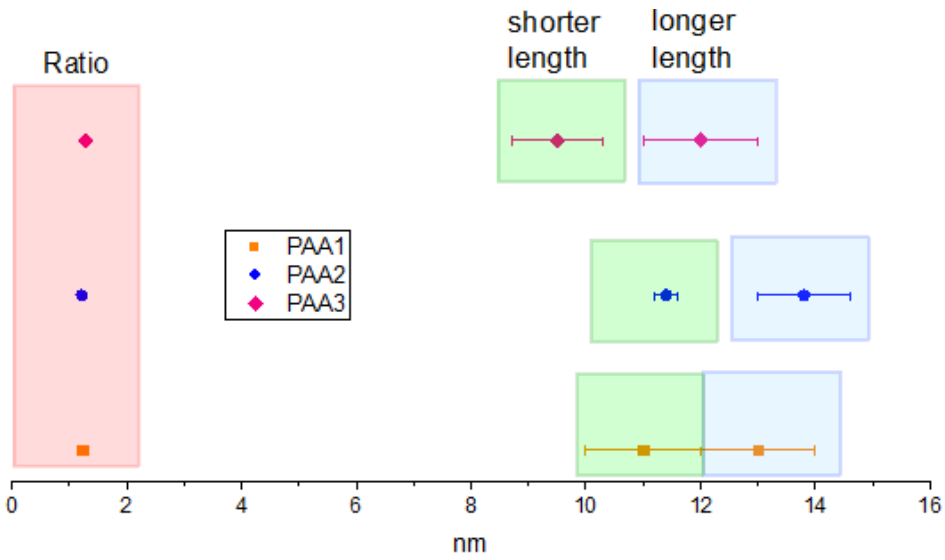

Figure 77: graphical illustration of the values reported in Table 9. Shorter lengths are reported inside the green box, ratios (longer length/shorter length) are reported inside the red box and longer lengths are reported inside the blue box

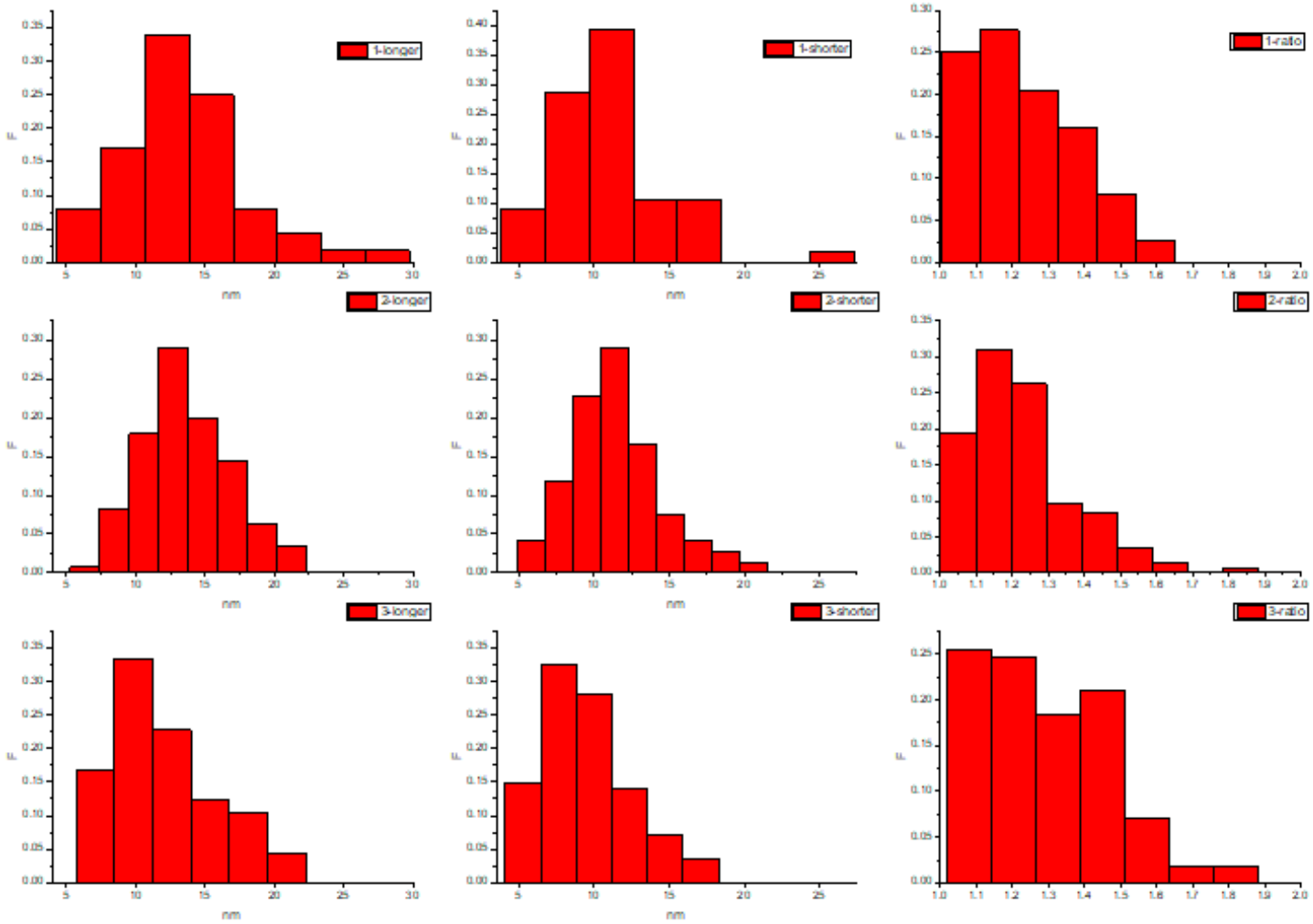

Figure 78: distributions of parameters reported in Table 9.Longer lengths, shorter lengths and the ratio (longer/shorter) are reported from left to right in each row which correspond from the first to the third row to PAA1, PAA2, PAA3

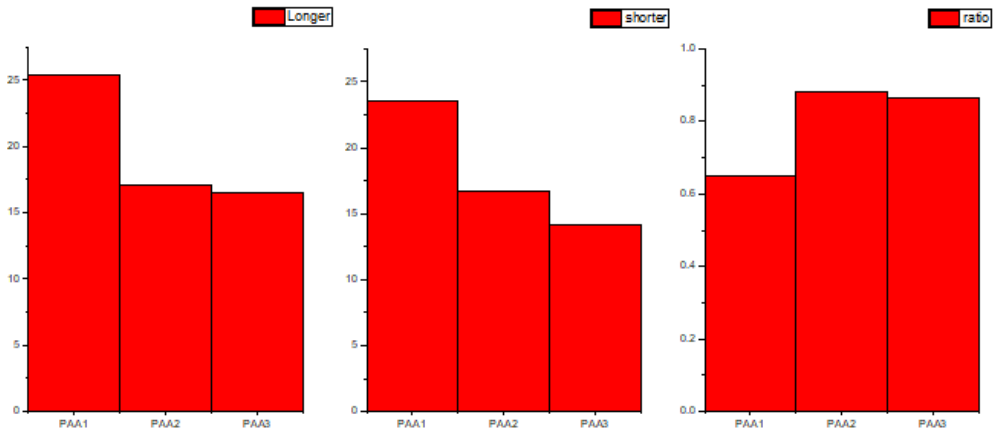

Figure 79: graphical illustration of distribution widths of values reported in Table 9, from right to left: longer dimensions, shorter dimensions and ratios of PAA1,PAA2,PAA3.

FT-IR

As reported in the purification paragraph, the separation of CuS-PAA NPs from the reaction solution is hard to achieve. For this reason, the attempts to use purified CuS-PAA NPs for the FT-IR analysis have led to useless spectra without any visible band due to the scarcity of CuS-PAA NPs in the KBr pellet. Thus, FT-IR has been performed on IR-CARD on which the reaction solution of CuS-PAA NPs has been deposited by drop-casting. In this condition, bands of both bonded and free PAA are expected.

IR spectrum of free PAA contains broad bands due to the multitude of possible local conformations of the polymeric chains (Todica et al. 2015).

Table 10: expected bands position for PAA

	Bands positions (cm-1)
ν(C=O)	1700
δ(OH) and ν(-C-O)	1170-1300
ν(OH)	3450
ν (CH)	2850-3000
δ(CH)	1350-1480

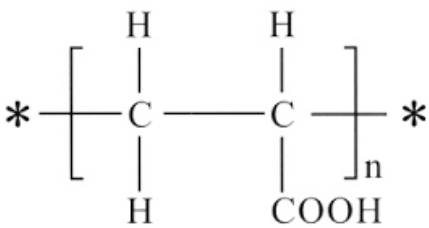

Figure 80: illustration of PAA structure

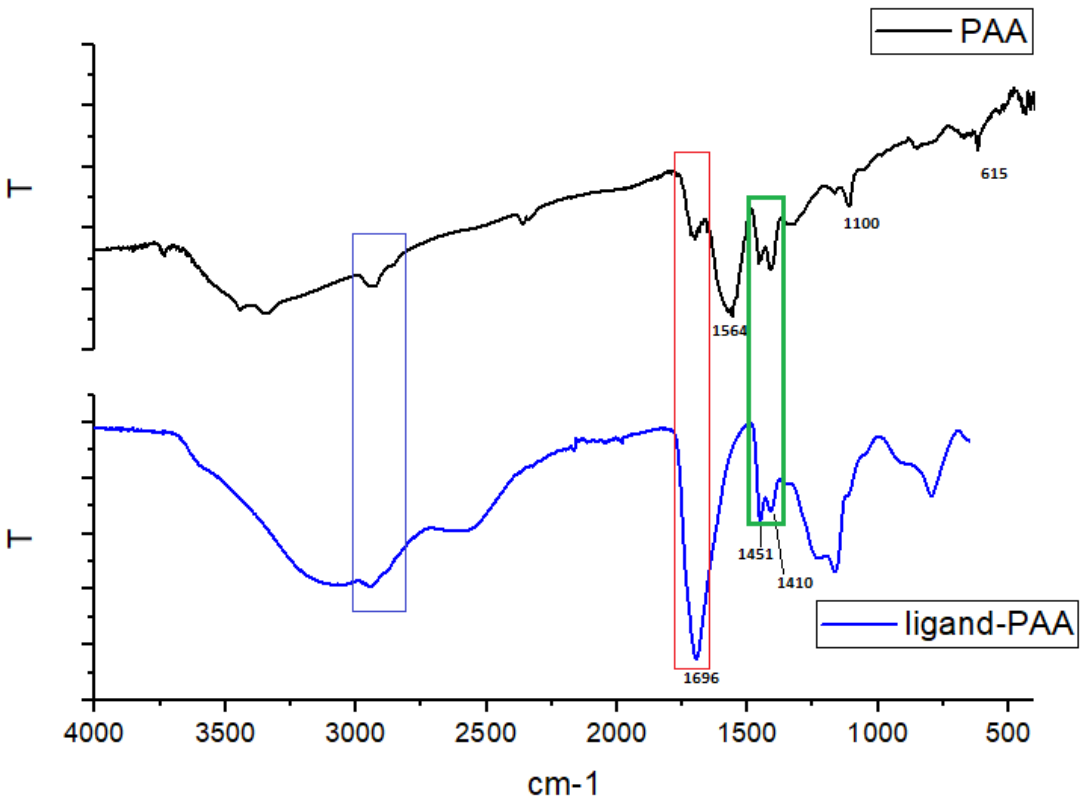

Figure 81: IR spectra of free PAA (below) and CuS-PAA NPs (above)

The IR spectrum of the nanoparticles, despite being obtained from the post reaction solution it is clearly different when compared with the free ligand spectrum. The OH stretching band above 3000cm^{-1} is influenced by intramolecular bonds which occur both in free PAA and in NPs organic layer. For NPs this band is visible at higher wavenumbers and correspond to a shoulder in the free ligand spectrum. This means that part of the contributions to this band are quenched by the bond between PAA and particle core. Thanks to the narrower OH stretching band the C-H stretching bands are clearly visible in the IR spectrum of the NPs (blue box). The red box in Figure 81 highlights the C=O stretching band; in the NPs spectrum 2 close bands can be assigned to this vibrational mode, the less intense one at the same wavenumber of free PAA given by free polymer (present in the reaction solution) and a more intense one shifted to lower wavenumbers due to PAA in the organic layer (a similar shift has been already reported for bonded citrate). Inside the green box the CH bending bands result unaltered in NPs spectrum. The broad double band at ~1300-1100 cm^{-1} due to OH bending and -C-O stretching in the free ligand spectrum in the NPs spectrum is quenched and split into two separated bands, one more intense adjacent the green box and another less intense at 1168 cm^{-1} . Also, for CuS-PAA NPs the characteristic band, assigned to the particles, is visible at 110 cm^{-1}.
These changes in the IR spectra suggest that carboxylic groups are the anchoring groups of PAA.

DLS analysis

A fresh sample of CuS-PAA NPs has undergone DLS analysis without any purification step. An average diameter of 48.2 nm has been measured for CuS-CIT NPs in solution. It can be considered compatible with the magnitude order determined with TEM images taking hydrodynamic radius into account. Since the PdI value determined is 0.494, the sample is averagely polydisperse.

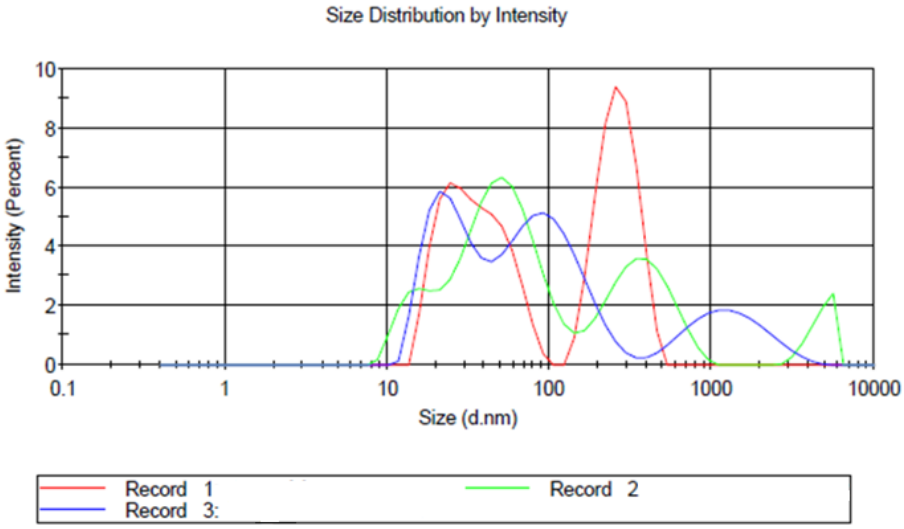

Figure 82: size distribution by intensity of CuS-PAA NPs

UV-VIS Spectroscopy

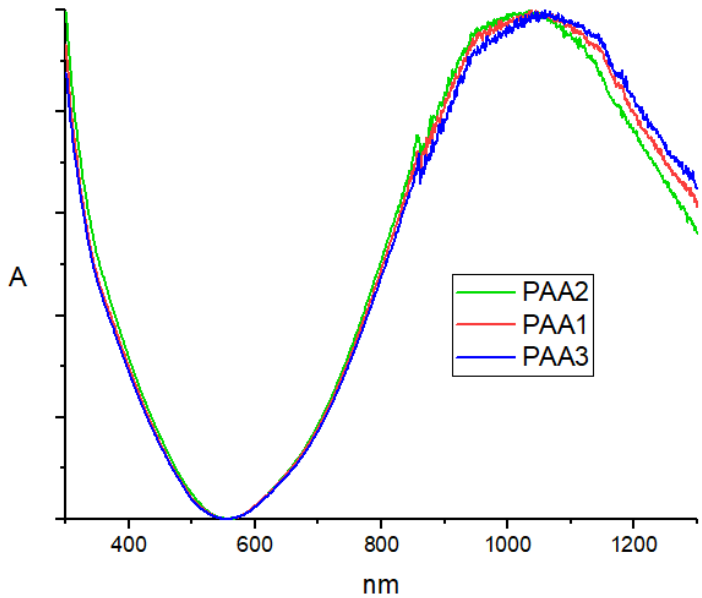

Figure 83: absorption spectra of PAA1, PAA2, PAA3

Table 11: λmax value of samples LSPR bands

Sample	λmax (cm^{-1})
PAA1	1042
PAA2	1032
PAA3	1060

Purification

Different conditions are required depending whether centrifuge (8000rpm, falcon) or ultracentrifuge (14000, eppendorf) for the purification, these are reported in Table 12.

Table 12:purification conditions

1° purification step	antisolvent	Sample/ solvent volume	Time	deposit	Supernatant
800 rpm (Falcon)	THF	1:3	2x40min[20]	Presence of a solid aggregate in the solution (like a seaweed)	Green
14000 rpm (Eppendorf)	Isopropanol	1:3	20 min	Presence of solid in the bottom of Eppendorf	green

2° purification step	Antisolvent	Volume of solvent	Time	redispersion
800 rpm (Falcon)	THF	500µL	25 min	Water
14000 rpm (Eppendorf)	Isopropanol	2 ml	20 min	Water

The amount of solid (particles) that can be collected with both procedures is really small. Especially without ultracentrifuge the separation of NPs from the reaction solution is hard to obtain. For this reason, NPs purified twice have been used to prepare TEM grids and NPs purified one time for XRD sample praparation. The NPs organic layer grants them stability in solution and therefore to promote NPs precipitation this has to be reduced via its solubilization. PAA is soluble in THF, water, methanol and ethanol. Solvents which have been tried as purification means (using centrifuge) are acetone, ethanol, isopropanol, water, methanol but the only one that allowed to obtain a solid with the centrifuge is THF.

CuS-CTAB ligand Cetyl trimethylammonium bromide

In order to evaluate the reproducibility of the protocol, three samples have been prepared and are reported as CTAB1, CTAB2, CTAB3 while CTAB4 has been synthetized with a continuous flow of Argon from the Na_2S adding to the reaction quenching.

XRD

XRD analysis has been performed on NPs obtained by one step of purification. Only one sample of CuS-CTAB has been analysed with D8 Advance Bruker instrument in Bragg-Brentano mode. As it can be seen in Figure 84 all reference peaks of hexagonal covellite match the peaks in the CuS-CTAB XRD pattern. Light-green circles in Figure 84 highlights the peaks at ~45 and 28 which, as already discussed, can be attribute bot to phase impurities and to salts remained after the purification. Anyway, these peak intensities are much less intense than covellite peaks.

[20] After the first centrifugation the solid aggregate present in the solution has been transferred with a pipette into another falcon and centrifugated again to separate it from the liquid collected together.

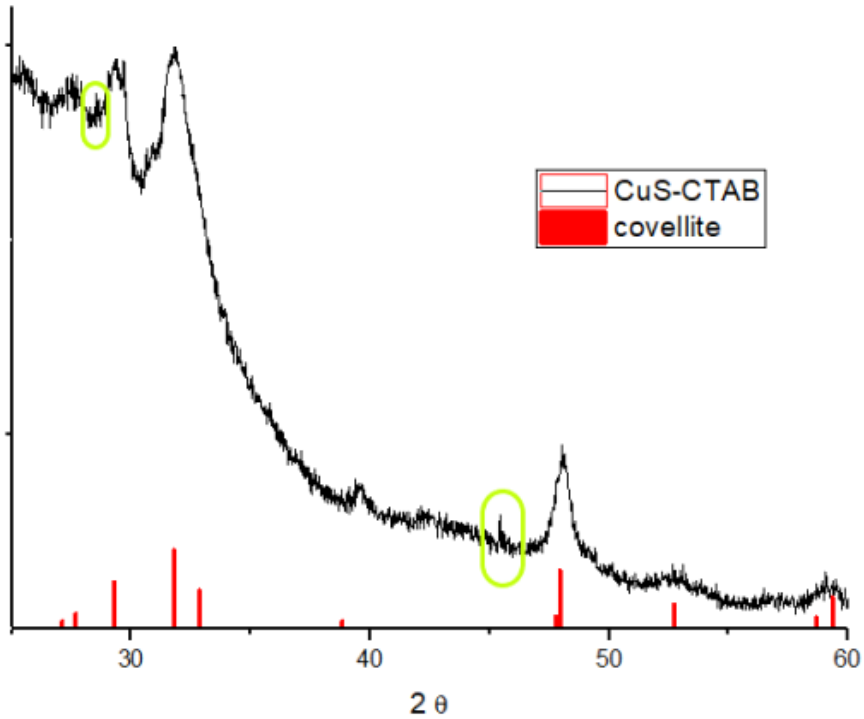

Figure 84: XRD pattern of CuS-CTAB NPs and reference sticks of hexagonal covellite in red.

(110) reflection was used to determine the diameter which has been estimate of 13.0 ± 0.3 nm.

TEM

The solution obtained as described in the CuS-CTAB synthetic protocol has to be purified before preparing TEM grids in order to obtain useful TEM images.

CuS-CTAB NPs of CTAB1, CTAB2, CTAB3 and CTAB4 samples' NPs have similar dimensions and morphology, showed in the following images. In TEM images NPs with size ranging from ~5 to 43nm can be seen. The smaller NPs are nearly-spherical, while the bigger have predominantly truncated triangular and hexagonal shape in addition to the nearly-spherical. Rod-like particles which are nanodisks sitting on their edges and their flat planes are present. Anisotropic particles contained in CuS-CTAB NPs samples are highlighted in Figure 88.

For the determination of particle size, round and hexagonal particles have been considered and, as already reported for CuS-PAA and CuS-CIT, their longer and shorter lengths have been measured.

Particles composed by different crystalline domains are showed in HRTEM images.

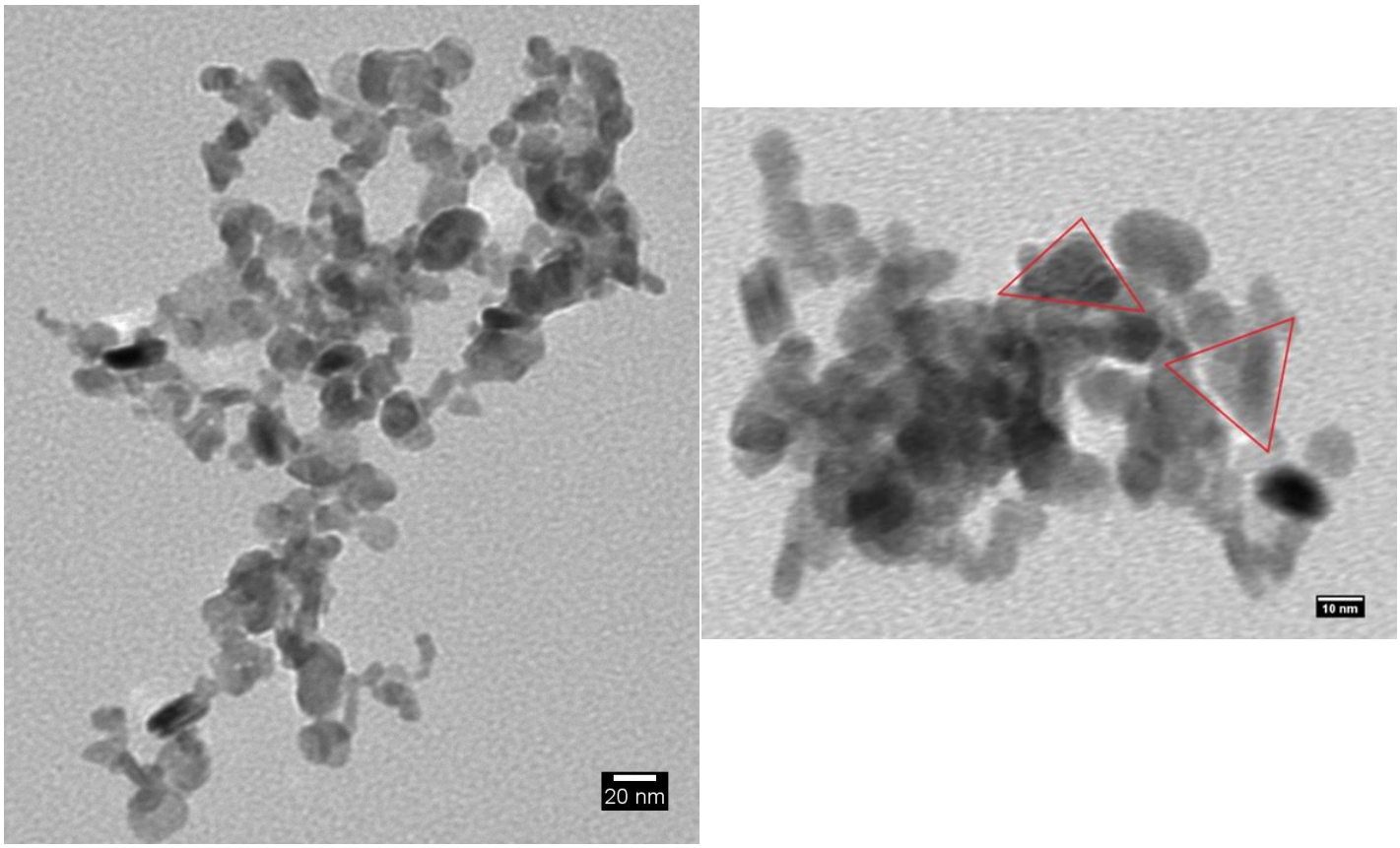

Figure 85: TEM image of CTAB1(left) and CTAB2 (right)

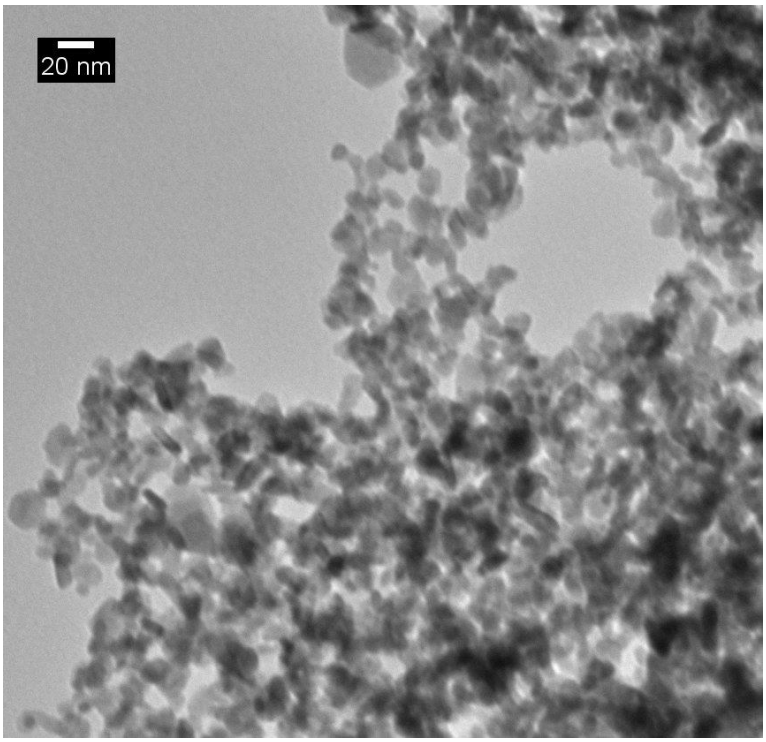

Figure 86: TEM image of CTAB3

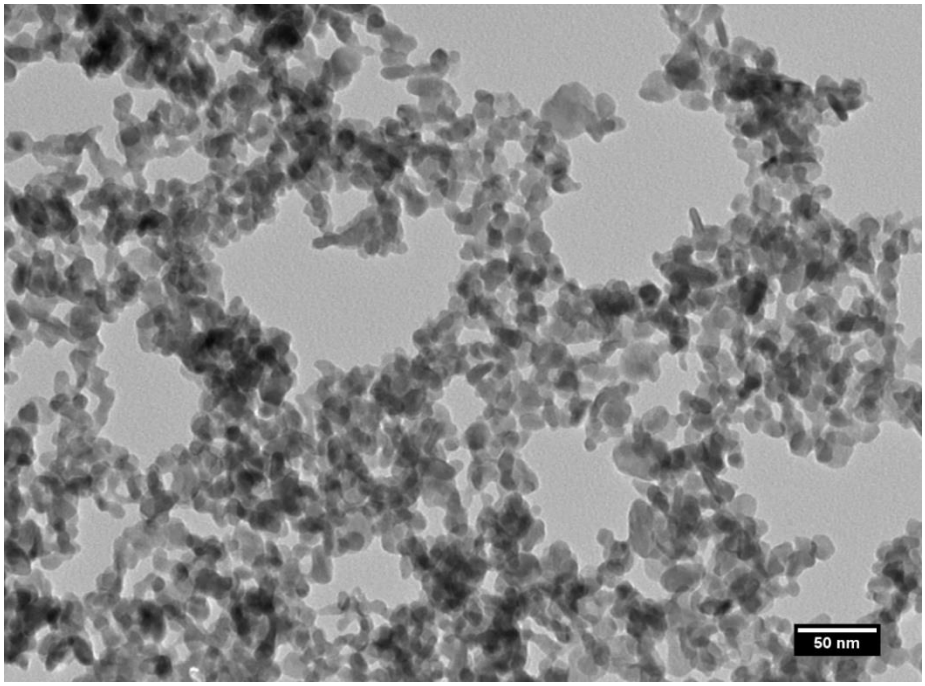

Figure 87: TEM image of CTAB4

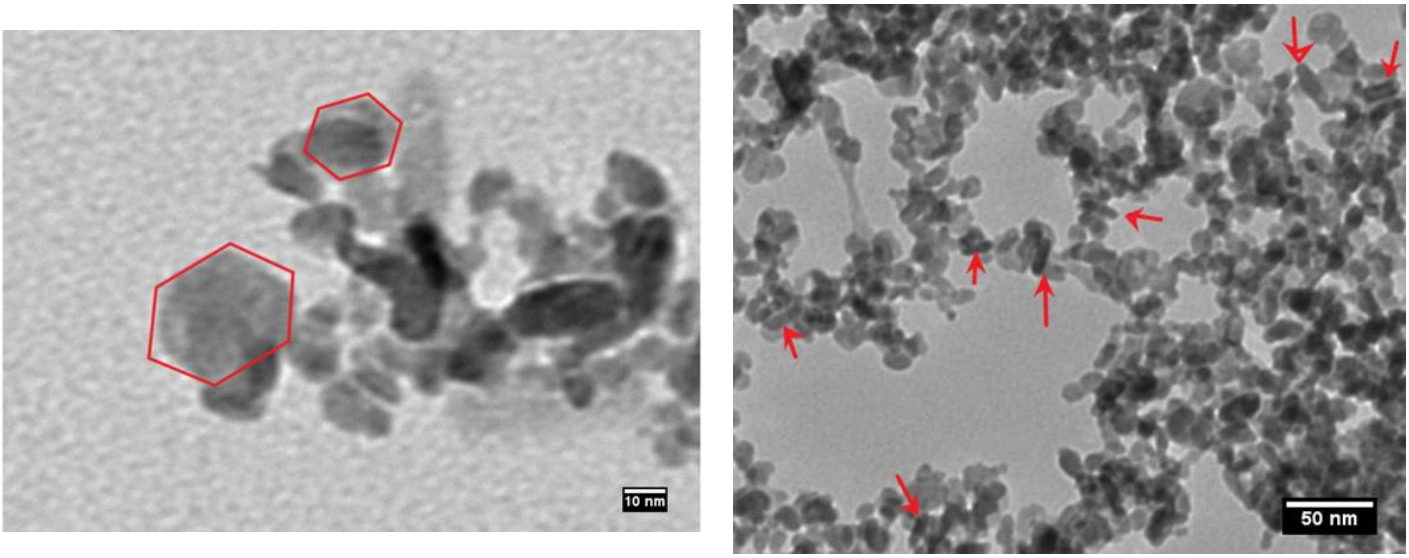

Figure 88: TEM images where anisotropic particles are evidenced, in the image on the right arrows points edge view of NDs.

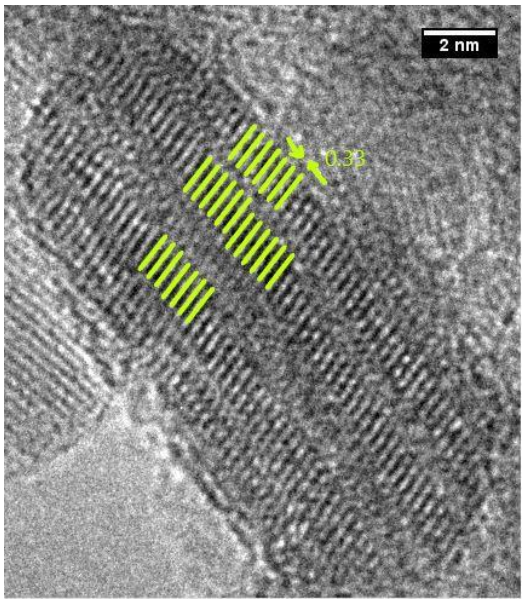

Figure 89: HRTEM of a CuS-CTAB ND sitting on its edge. Green lines highlight crystalline domains with spacing of 0.33nm

Table 13: CTAB1, CTAB2, CTAB3, CTAB4 parameters determined from TEM images

sample	parameter	Average value (nm)	Minimum value (nm)	Maximum value (nm)
CTAB1	Longer length	22 ± 1	7.3	43.3
	Shorter length	15 ± 1	7.2	36.5
	ratio	1.25 ± 0.05	1.00	1.74
CTAB2	Longer length	17 ± 1	6.0	35.3
	Shorter length	12 ± 1	4.6	29.2
	ratio	1.23 ± 0.05	1.02	1.69
CTAB3	Longer length	18 ± 1	7.4	36.1
	Shorter length	13 ± 2	5.5	33.4
	ratio	1.3 ± 0.1	1.0	1.9
CTAB4	Longer length	18 ± 1	8.6	40.8
	Shorter length	13 ± 2	7.2	34.6
	ratio	1.3 ± 0.05	1.00	1.67

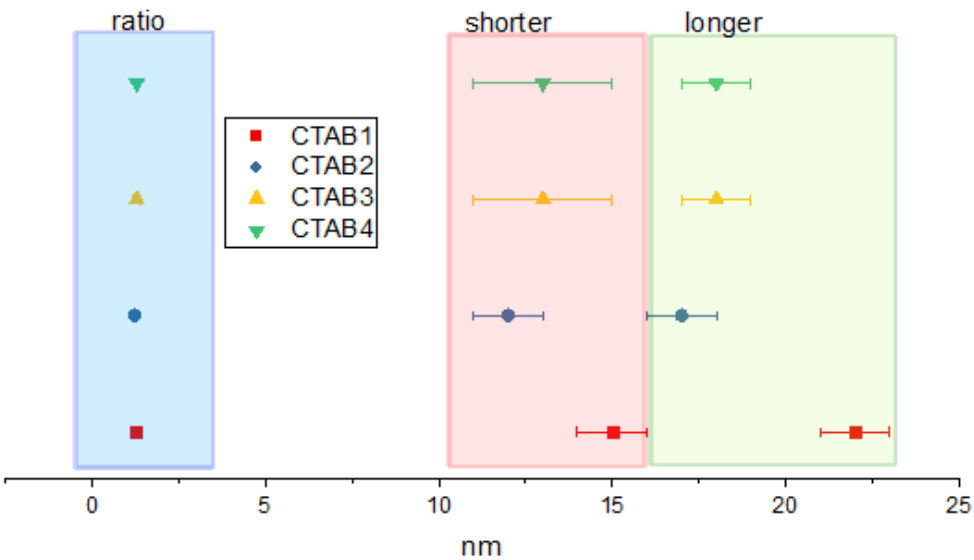

Figure 90: graphical illustration of the values reported in Table 13. Shorter lengths are reported inside the red box, ratios (longer length/shorter length) are reported inside the blue box and longer lengths are reported inside the green box

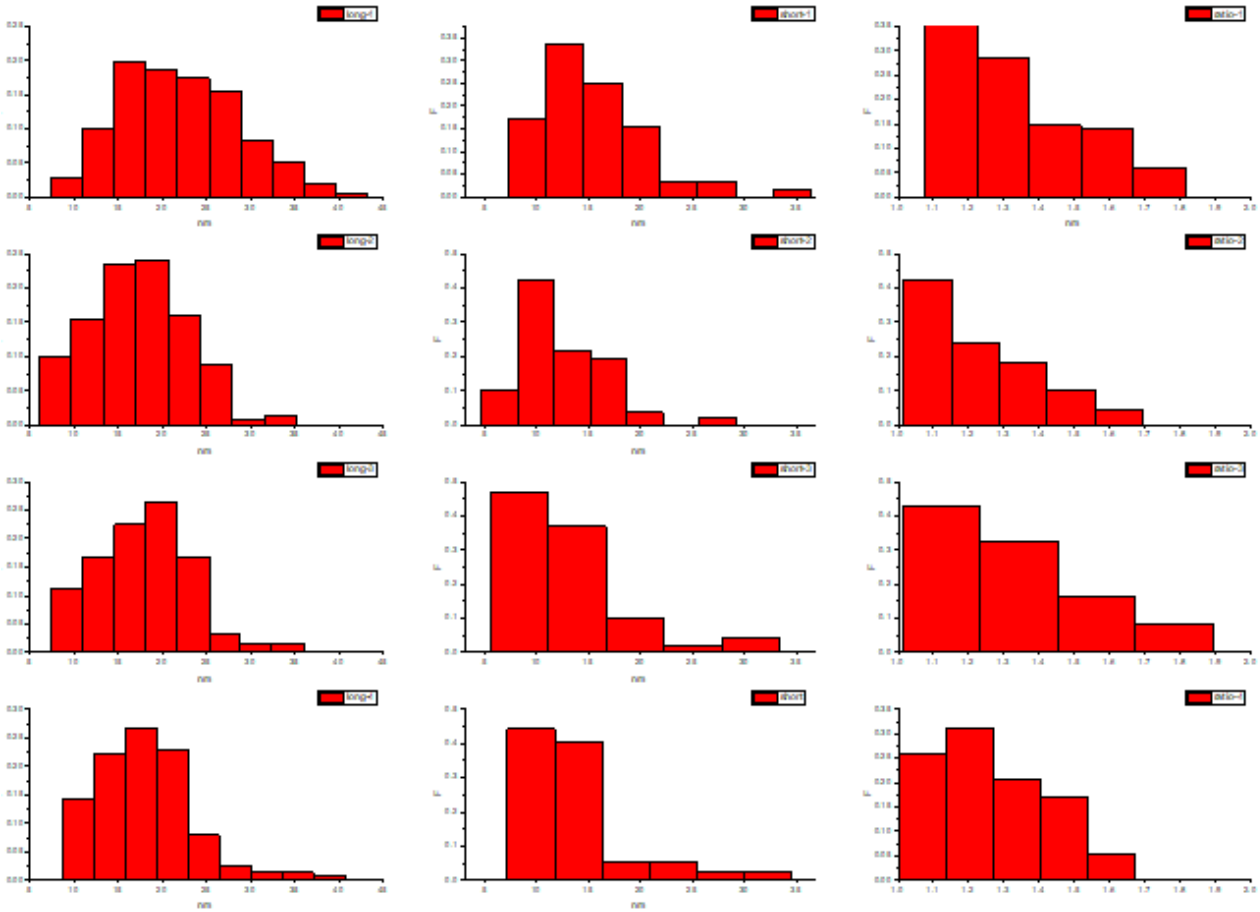

Figure 91: distributions of parameters reported in Table 13. Longer lengths, shorter lengths and the ratio (longer/shorter) are reported from left to right in each row which correspond from the first to the third row to CTAB1, CTAB2, CTAB3, CTAB4.

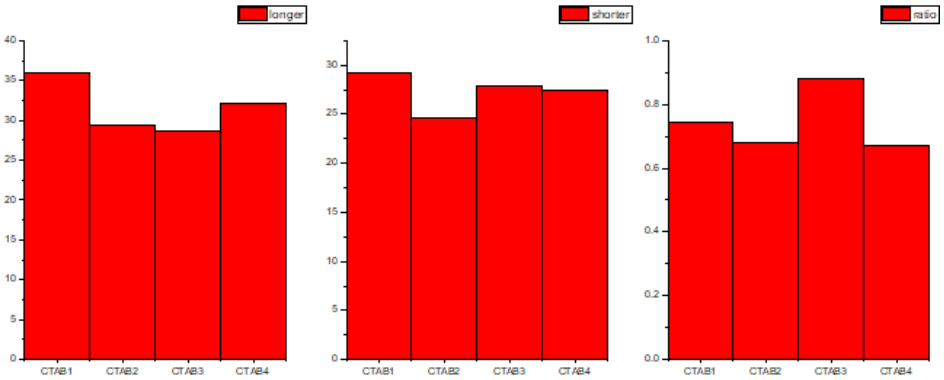

Figure 92: graphical illustration of distribution widths of values reported in Table 13, from right to left: longer dimensions, shorter dimensions and ratios of CTAB1, CTAB2, CTAB3,CTAB4.

For CuS-CTAB NPs the longer and the shorter lengths have different distribution patterns. CTAB4 and CTAB3 have the same longer and shorter average lengths and ratio and also the same distributions of these parameters. Thus, there isn't any difference due to the duration of argon flow. CTAB1 distribution show the largest population with high value of longer length.

FT-IR

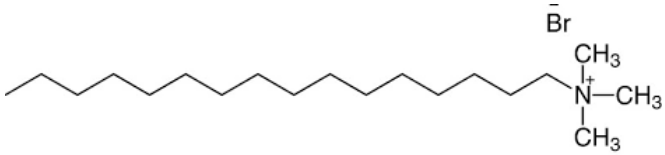

Figure 93: illustration of CTAB structure

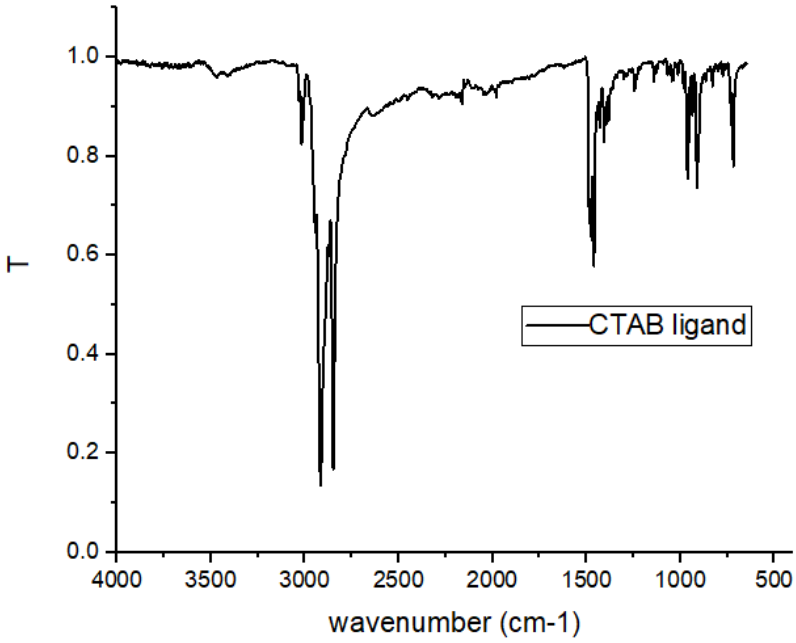

Figure 94: IR spectra of free CTAB

Table 14:expected band positions for CTAB

	Band positions (cm-1)
ν $N(CH_3)_3^+$	3015
ν C-N	960
ν (C-H of CH_2)	2850-3000
δ(C-H of CH_2 and CH_3-N^+)	1460-1490

CuS-CTAB NPs used for FT-IR analysis have undergone two purification steps, as described below in the purification paragraph. After desiccation, precipitate NPs have been mixed with KBr to prepare the pellet. The purification is very effectively at removing CTAB from the layer leading to an easy separation of NPs from the solution. On the other hand, the efficient purification leads to a low intensity of CTAB expected bands in the IR spectrum of NPs. In order to make bands more visible sample spectrum has been reported into two graphs in Figure 95.

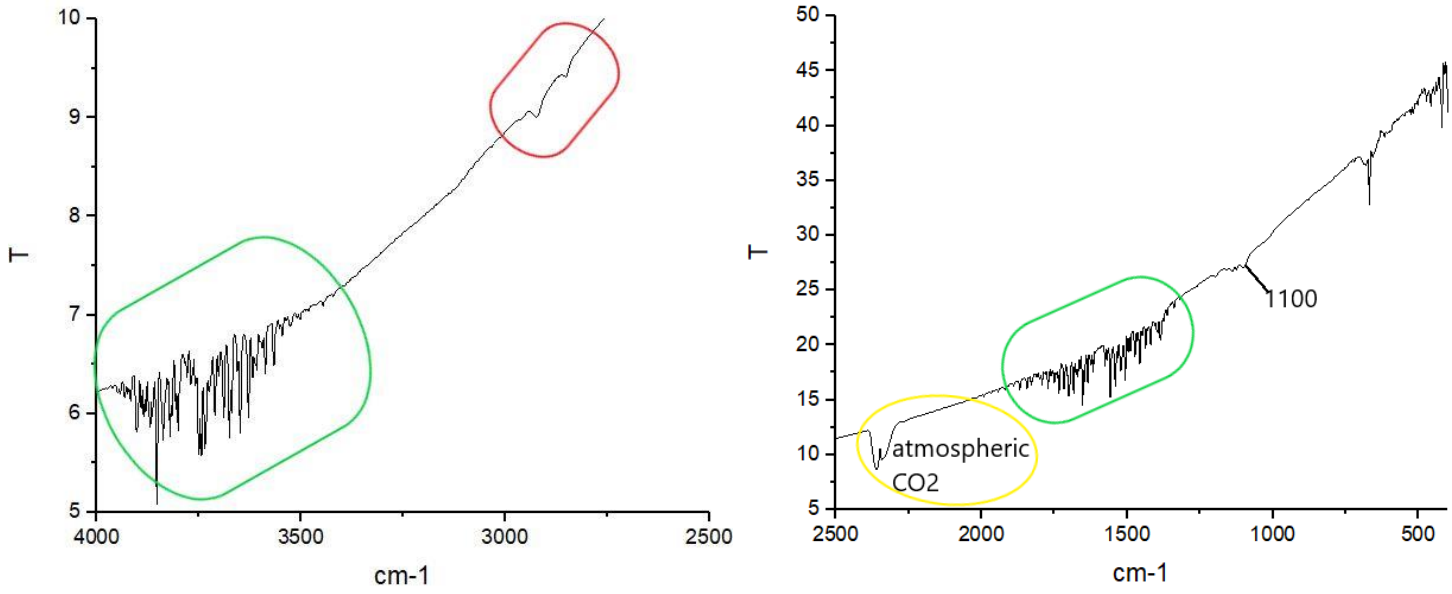

Figure 95: IR spectra of CuS-CTAB NPs reported into two pieces

The only bands proving the presence of CTAB are highlighted in red in Figure 95 and correspond to υ C-H (the signal at 3015 cm^{-1} is not clearly visible). The serrated signals in the green boxes and the peak at 1100 cm^{-1} can be assigned to particles core.
Based on what is reported by (Lu et al. 2015) CTAB molecules bonds the CuS surface through their head group.

DLS analysis

Two non-purified samples of CuS-CTAB NPs solution have been measured. One sample was freshly made and the other one was 1 month old (CTAB4). As already said for CuS-PAA and CuS-CIT, also for CuS-CTAB, DLS confirms the order of magnitude measured from TEM images, taking into account the hydrodynamic radius. Both samples are on average polydisperse (Pdl=0.308 for the fresh sample and Pdl=0.273 for the old sample). The average diameter calculated for the samples are equal to 38.52nm for the fresh sample and 86.48nm for the old sample. Even though in the old sample the particles weren't visibly aggregated, and the two solutions appeared identical DLS analysis evidenced a certain level of aggregation.
(Distribution by number has been obtained knowing that the CuS-CTAB NPs refractive index is 2.2)

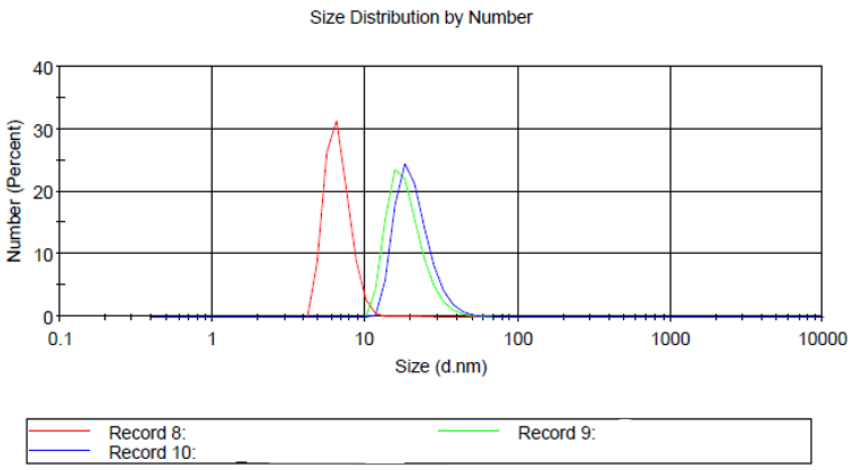

Figure 96: size distribution by number of fresh sample

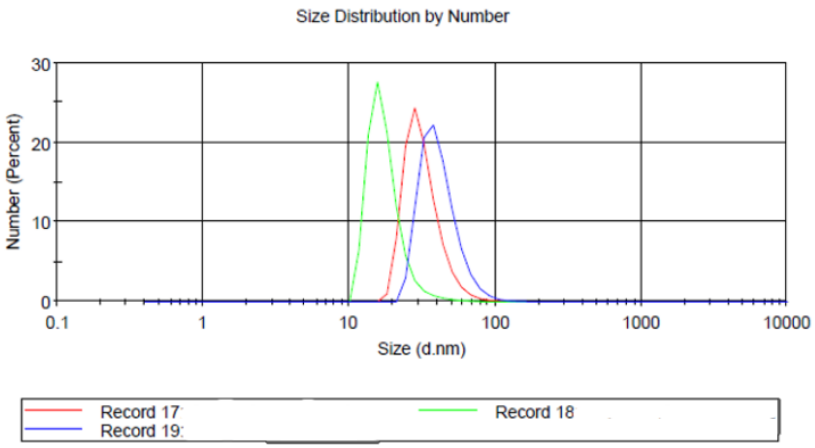

Figure 97: size distribution by number of one-month old sample

UV-VIS spectroscopy

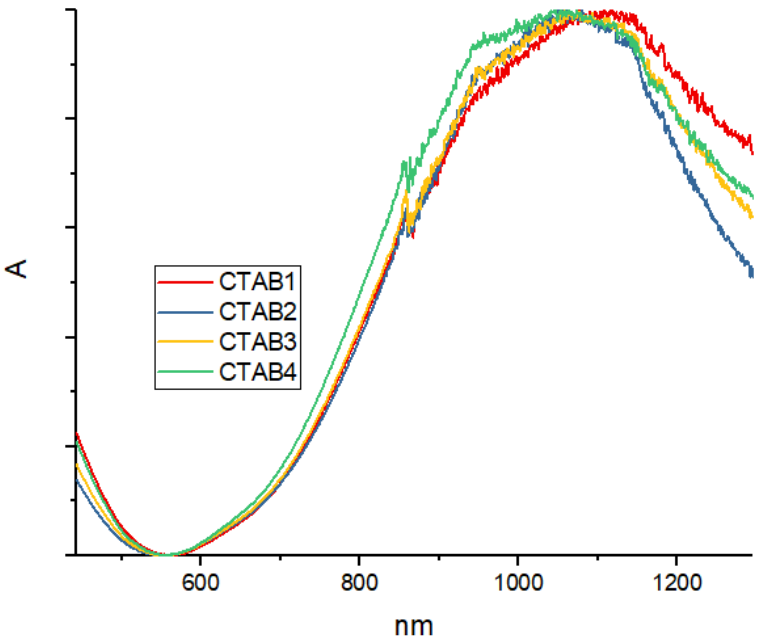

Figure 98: absorption spectra of CTAB1, CTAB2, CTAB3, CTAB4

Table 15: λmax values of samples LSPR bands

Sample	λmax (cm^{-1})
CTAB1	1112
CTAB2	1079
CTAB 3	1070
CTAB4	1056

CTAB1 shows a band profile different from other samples, the main peak can't be clearly identified and therefore its λmax is not reported in Table 15. Furthermore, CTAB1 band is wider due to the lower slope of the high wavenumber tail.

Purification

Isopropanol is a good solvent to precipitate the CuS-CTAB. Indeed, CuS-CTAB NPs are the only particles which completely separate from the liquid that remains clear.

Table 16: Different conditions required for purification depending whether centrifuge (8000rpm, falcon) or ultracentrifuge (1400, Eppendorf) is used.

1° purification step	solvent	Sample/ solvent	Time	Result of the 1° purification: deposit	Result of the 1° purification: solution
800 rpm (Falcon)	isopropanol	1:1	30 min	Stuck to the walls of the Falcon	clear
14000 rpm (Eppendorf)	Isopropanol	1:1	20 min	In the bottom of the Eppendorf	clear

2° purification step	solvent	Volume of solvent	Time	redispersion
800 rpm (Falcon)	isopropanol	500µl	20 min	Isopropanol or water
14000 rpm (Eppendorf)	Isopropanol	2 ml	20 min	Isopropanol or water

2 steps of purification are necessary to prepare TEM grid and also for preparing KBr pellet NPs have undergone two purification steps. One step of purification has been used to prepare XRD sample.
After the second step the precipitate has been re-dispersed in a volume equal to half the volume of the CuS-CTAB solution used. In the re-dispersion of the CuS-CTAB both in water and in isopropanol particles are present as large aggregates and the same result is also obtained mixing isopropanol and water. This can be seen also with the naked eye. Further proof of strong aggregation is the result of DLS analysis (after 1step of purification) that measure an average diameter of 8688nm (PdI 0.430).

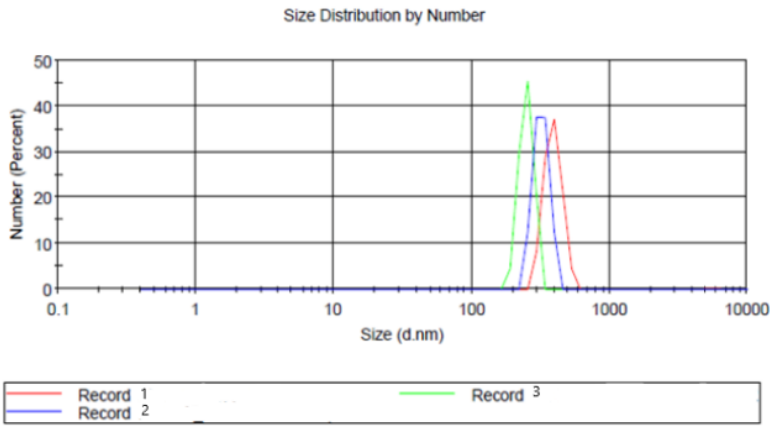

Figure 99: size distribution by number of a CuS-CTAB NPs purified (1step) solution

Comparison between NPs

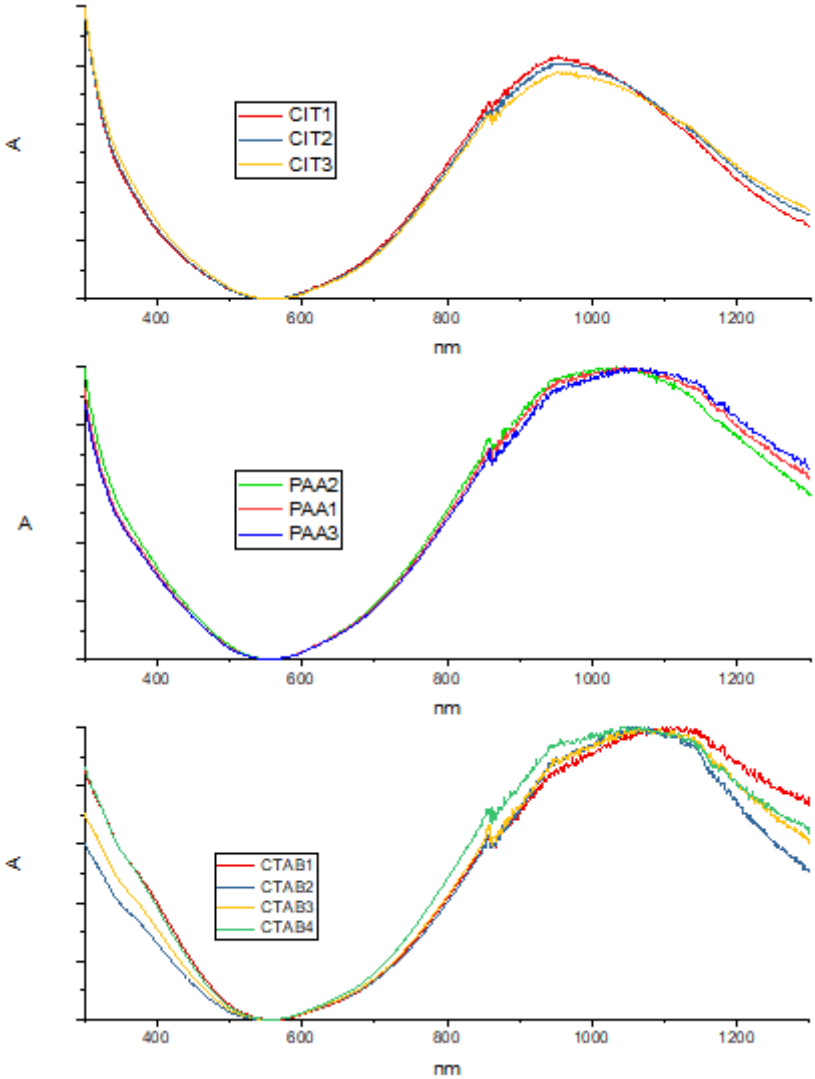

Figure 100: comparison between CuS NPs absorption spectra

CuS-CIT NPs have the narrowest band. CuS-CTAB and PAA NPs bands have higher intensity (as it can be seen in Figure 101 and their λmax is shifted to higher wavelengths. Position and intensity of the bands are influenced by the refractive index of the particles surrounding medium and therefore by the organic layer. The increase of the refractive index leads to a higher intensity and to the red shift of the band. Refractive index of the organic ligands used are reported in Table 17:

Table 17: refractive index of organic ligands

ligand	Refractive index
CIT	1.394
CTAB	1.336
PAA	1.527

Based on the refractive index the experimental trend of NPs LSPR bands is not explained and therefore this parameter influence on the absorption spectra is negligible compared to other factors. Indeed, the change in the LSPR bands can be explained with a different content of disk-like nanoparticles. When larger (than the spherical particles) flat particles are present the band red shifts and the intensity increase(Marin et al. 2018)(Zhu et al. 2015a). CuS CIT NPs are in fact the particles with the narrower size distribution, smaller

average size and ratio. All these parameters suggest that these samples are composed mostly of nearly-spherical particles and further confirmation is the absence of narrow reflections in their XRD patterns.

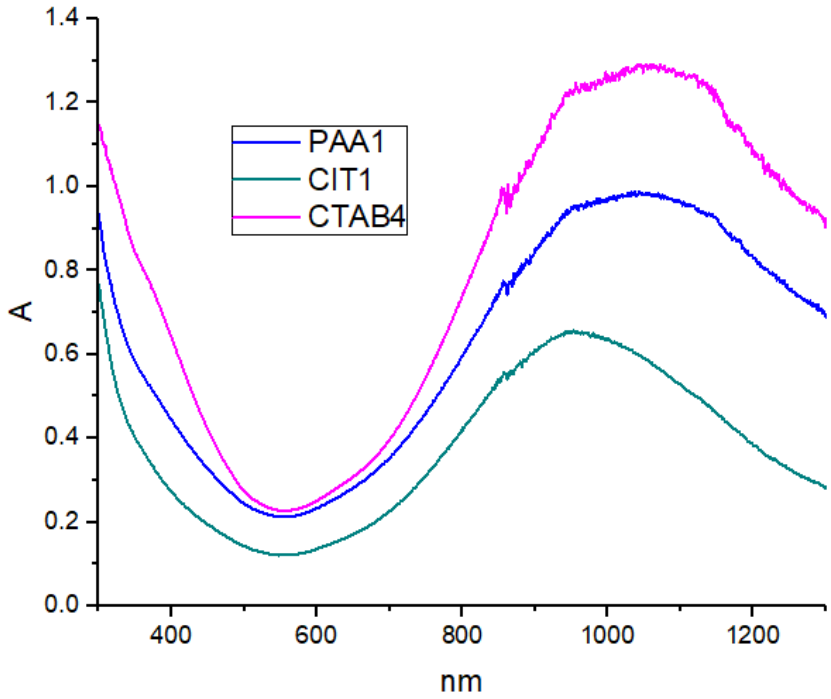

Figure 101: comparisons between CuS NPs to highlight differences in bands intensity

Based on absorption spectra it can be said that CuS-CTAB NPs synthesis is the less reproducible one.
The ratio distribution and average value are useful to estimate the content of disk-like particles which are characterized by higher value of r than the nearly spherical particles. Indeed, CuS-CTAB NPs samples having the higher average sizes should have also the lower λmax if the particles would be spherical (Zhu et al. 2015b), in contrast to what experimentally determined. On the other hand, CuS-CTAB NPs have the higher average value of ratio suggesting the higher content of disk-like NPs which explain the high λmax. Furthermore, ratio distributions may be correlated to the absorption band shape; CTAB1 which shows an asymmetric band with wider longer wavelength tails has a lack of the smaller population in r distribution.

Conclusions

Two heat up synthetic protocols for the production of disk-like nanocrystals of copper sulphides have been studied. The factor which leads to covellite phase with the first synthetic protocol has been recognised to be the oxidation state of the copper ion used which has to be Cu(II). The second synthetic approach, instead, leads to covellite NDs starting from Cu(I) salt. The NDs obtained with the second synthetic protocol have smaller size, narrower distribution and a thicker organic layer and consequently they form superstructures in solution, altering their absorption spectra. The differences between the results obtained with the two synthetic protocols arise from the different reaction temperature and ratio [Cu monomers] / [S monomers]. The monomers ratio depends on the precursor's treatment and its influence on the NDs morphologies has been demonstrated. The NDs growth perpendicular to c axis has been proved by means of HRTEM images. The absorption spectra of covellite NDs follow what is reported in literature.

Further studies on samples taken during the reaction are needed to better understand nucleation and growth mechanisms in the heat up methods. To indagate fully the organic shell composition and therefore to reach a better comprehension of the parameters that influence the assembly an NMR and an AFM-IR studies would be useful. Indeed, it is possible that particles form at different reaction time and temperature leading to different organic layers of NDs in the sample.

Copper sulphide nanoparticles with citrate, PAA and CTAB as organic ligands have been synthetized through a green approach and they have been fully characterized. CuS-CIT NPs have size about 10nm, mainly spherical shape, narrow distribution and their synthesis is reproducible. For these particles further studies to asses their phases are needed and their heat conversion efficiency should be measured.
The particles synthetized with CTAB and with PAA have a larger distribution, larger size and different morphologies since hexagonal and truncated triangular shaped NDs are produced along with spherical particles. Further studies are needed to reduce the number of larger flat nanoparticles obtained from the reaction.
The reaction parameters affecting the NPs optical and morphological features are: the temperature, the amount of organic ligand used to control the growth, the pH of the reaction mixture and the ratio S/Cu(Marin et al. 2018). The ratio S/Cu is the parameter that, among the others shows the strongest influence on particles morphology and therefore further synthesises of CuS-CTAB and CuS-PAA NPs with a lower ratio S/Cu are needed to address the ratio value that lead to particles with homogeneous morphology.

Bibliography

Amendola, V., R. Pilot, M. Frasconi, O. M: Maragò, and M. A. Iati. 2017. "Surface Plasmon Resonance in Gold Nanoparticles : A Review." *Journal of Phisics: Condensed Matter* 29.

Blachnik, R., and A. Müller. 2001. "The Formation of Cu2s from the Elements II. Copper Used in Form of Foils." *Thermochimica Acta* 366 (1): 47–59. https://doi.org/10.1016/S0040-6031(00)00711-5.

Boey, H T, W L Tan, N H H Abu Bakar, M Abu Bakar, and J Ismail. 2007. "Formation and Morphology of Colloidal Chitosan-Stabilized Copper Sulfides." *Journal of Physical Science* 18 (1): 87–101. https://doi.org/10.1007/BF00001125.

C. Beynis, (Graduate School of the University at Bu alo). 2014. "'Counterdoping' and Tuning of the Near Infrared Plasmonics in Non Stoichiometric Copper Sulfide for Solar Cell Application." State University of New York at Buffalo.

Chen, L., M. Sakamoto, R. Sato, and T. Teranishi. 2015. "Determination of a Localized Surface Plasmon Resonance Mode of Cu<inf>7</Inf>S<inf>4</Inf> Nanodisks by Plasmon Coupling." Faraday Discussions. Royal Society of Chemistry. 2015. https://doi.org/10.1039/c4fd00239c.

Comin, Alberto, and Liberato Manna. 2014. "New Materials for Tunable Plasmonic Colloidal Nanocrystals." *Chemical Society Reviews* 43 (11): 3957–75. https://doi.org/10.1039/c3cs60265f.

Cotton, F.A., and G. Wilkinson. 1988. *Advanced Inorganic Chemistry*. Edited by Wiley. 6th ed.

Coughlan, Claudia, Maria Ibáñez, Oleksandr Dobrozhan, Ajay Singh, Andreu Cabot, and Kevin M. Ryan. 2017. "Compound Copper Chalcogenide Nanocrystals." *Chemical Reviews* 117 (9): 5865–6109. https://doi.org/10.1021/acs.chemrev.6b00376.

D.J. Chakrabarti, and D.E. Laughlin. 1983. "The Cu-S (Copper-Sulfur) System." *Bulletin of Alloy Phase Diagrams*.

Dixit, Sharad G., Anand R. Mahadeshwar, and Santosh K. Haram. 1998. "Some Aspects of the Role of Surfactants in the Formation of Nanoparticles." *Colloids and Surfaces A: Physicochemical and Engineering Aspects* 133 (1–2): 69–75. https://doi.org/10.1016/S0927-7757(97)00126-X.

Embden, Joel Van, Anthony S.R. Chesman, and Jacek J. Jasieniak. 2015. "The Heat-up Synthesis of Colloidal Nanocrystals." *Chemistry of Materials* 27 (7): 2246–85. https://doi.org/10.1021/cm5028964.

Faucheaux, Jacob A., Alexandria L D Stanton, and Prashant K. Jain. 2014. "Plasmon Resonances of Semiconductor Nanocrystals: Physical Principles and New Opportunities." *Journal of Physical Chemistry Letters* 5 (6): 976–85. https://doi.org/10.1021/jz500037k.

He, Jian, Lisha Ai, Xin Liu, Hao Huang, Yuebin Li, Mingguang Zhang, Qianru Zhao, Xingguo Wang, Wei Chen, and Haoshuang Gu. 2018. "Plasmonic CuS Nanodisk Assembly Based Composite Nanocapsules for NIR-Laser-Driven Synergistic Chemo-Photothermal Cancer Therapy." *Journal of Materials Chemistry B* 6 (7): 1035–43. https://doi.org/10.1039/c7tb02772a.

Hsu, Su Wen, Whitney Bryks, and Andrea R. Tao. 2012. "Effects of Carrier Density and Shape on the Localized Surface Plasmon Resonances of Cu 2-XS Nanodisks." *Chemistry of Materials* 24 (19): 3765–71. https://doi.org/10.1021/cm302363x.

Hsu, Su Wen, Charles Ngo, and Andrea R. Tao. 2014. "Tunable and Directional Plasmonic Coupling within Semiconductor Nanodisk Assemblies." *Nano Letters* 14 (5): 2372–80. https://doi.org/10.1016/B978-0-08-100552-1.00018-X.

Jun, Young Wook, Jin Sil Choi, and Jinwoo Cheon. 2006. "Shape Control of Semiconductor and Metal Oxide Nanocrystals through Nonhydrolytic Colloidal Routes." *Angewandte Chemie - International Edition* 45 (21): 3414–39. https://doi.org/10.1002/anie.200503821.

Kore, R. H., J. S. Kulkarni, and S. K. Haram. 2001. "Effect of Nonionic Surfactants on the Kinetics of Disproportion of Copper Sulfide Nanoparticles in the Aqueous Sols." *Chemistry of Materials* 13 (5): 1789–93. https://doi.org/10.1021/cm010013r.

Kriegel, Ilka, Francesco Scotognella, and Liberato Manna. 2017. "Plasmonic Doped Semiconductor Nanocrystals: Properties, Fabrication, Applications and Perspectives." *Physics Reports* 674: 1–52. https://doi.org/10.1016/j.physrep.2017.01.003.

Lesyuk, Rostyslav, Eugen Klein, Iryna Yaremchuk, and Christian Klinke. 2018. "Copper Sulfide Nanosheets with Shape-Tunable Plasmonic Properties in the NIR Region." *Nanoscale* 10 (44): 20640–51.

https://doi.org/10.1039/c8nr06738d.
Liu, Maixian, Xiaozheng Xue, Chayanjit Ghosh, Xin Liu, Yang Liu, Edward P. Furlani, Mark T. Swihart, and Paras N. Prasad. 2015. "Room-Temperature Synthesis of Covellite Nanoplatelets with Broadly Tunable Localized Surface Plasmon Resonance." *Chemistry of Materials* 27 (7): 2584–90. https://doi.org/10.1021/acs.chemmater.5b00270.
Liu, Xin, Xianliang Wang, Bin Zhou, Wing Cheung Law, Alexander N. Cartwright, and Mark T. Swihart. 2013. "Size-Controlled Synthesis of Cu2-XE (E = S, Se) Nanocrystals with Strong Tunable near-Infrared Localized Surface Plasmon Resonance and High Conductivity in Thin Films." *Advanced Functional Materials* 23 (10): 1256–64. https://doi.org/10.1002/adfm.201202061.
Lu, Feng, Jinfeng Wang, Lin Yang, and Jun Jie Zhu. 2015. "A Facile One-Pot Synthesis of Colloidal Stable, Monodisperse, Highly PEGylated CuS@mSiO2nanocomposites for the Combination of Photothermal Therapy and Chemotherapy." *Chemical Communications* 51 (46): 9447–50. https://doi.org/10.1039/c5cc01725d.
Luther, George W., Stephen M. Theberge, Tim F. Rozan, David Rickard, C. C. Rowlands, and Anthony Oldroyd. 2002. "Aqueous Copper Sulfide Clusters as Intermediates during Copper Sulfide Formation." *Environmental Science and Technology* 36 (3): 394–402. https://doi.org/10.1021/es010906k.
Marin, R., A.Skripka, L. V. Besteiro, A. Benayas, Z. Wang, A. O. Govorov, P. Canton, and F.Vetrone. 2018. "Heat Conversion: Highly Efficient Copper Sulfide-Based Near-Infrared Photothermal Agents: Exploring the Limits of Macroscopic Heat Conversion." *Small* 49.
McPhail, Martin R., and Emily A. Weiss. 2014. "Role of Organosulfur Compounds in the Growth and Final Surface Chemistry of PbS Quantum Dots." *Chemistry of Materials* 26 (11): 3377–84. https://doi.org/10.1021/cm4040819.
National Nanotechnology Initiative. 2018. "No Title." Nano.Gov. 2018. https://www.nano.gov/nanotech-101/what.
Ruggiero, E., S. De Castro, A.Habtemariam, and L. Salassa. 2016. "Upconverting Nanoparticles For The Near Infrared Photoactivation Of Transition Metal Complexes: New Opportunities And Challenges In Medicinal Inorganic Photochemistry." *Dalton Trans* 45.
Rui, Xianhong, Huiteng Tan, and Qingyu Yan. 2014. "Nanostructured Metal Sulfides for Energy Storage." *Nanoscale* 6 (17): 9889–9924. https://doi.org/10.1039/c4nr03057e.
Silverstein, R.M., F. X. Webster, and D.J. Kiemle. 2015. *Identificazione Spettrometrica Di Composti Organici*. Edited by casa editrice Ambrosiana. Seconda.
Thomson, Jordan W., Kaz Nagashima, Peter M. MacDonald, and Geoffrey A. Ozin. 2011. "From Sulfur-Amine Solutions to Metal Sulfide Nanocrystals: Peering into the Oleylamine-Sulfur Black Box." *Journal of the American Chemical Society* 133 (13): 5036–41. https://doi.org/10.1021/ja1109997.
Todica, M., R. Stefan, C. V. Pop, and L. Olar. 2015. "IR and Raman Investigation of Some Poly(Acrylic) Acid Gels in Aqueous and Neutralized State." *Acta Physica Polonica A* 128 (1): 128–35. https://doi.org/10.12693/APhysPolA.128.128.
Viswanatha, R., and D. D. Sarma. 2007. *Growth of Nanocrystals in Solution*. *Nanomaterials Chemistry: Recent Developments and New Directions*. https://doi.org/10.1002/9783527611362.ch4.
Wang, Z., X.-D. Wen, R. Hoffmann, J. S. Son, R. Li, C.-C. Fang, D.-M. Smilgies, and T. Hyeon. 2010. "Reconstructing a Solid-Solid Phase Transformation Pathway in CdSe Nanosheets with Associated Soft Ligands." *Proceedings of the National Academy of Sciences* 107 (40): 17119–24. https://doi.org/10.1073/pnas.1011224107.
Wilcox, Teresa, and Amy Hirshkowitz. 2015. "NIH Public Access" 85 (0 1): 1–27. https://doi.org/10.1016/j.neuroimage.2013.08.045.The.
Wolf, Andreas, Torben Kodanek, and Dirk Dorfs. 2015. "Tuning the LSPR in Copper Chalcogenide Nanoparticles by Cation Intercalation, Cation Exchange and Metal Growth." *Nanoscale* 7 (46): 19519–27. https://doi.org/10.1039/c5nr05425g.
Wu, Haibin, and Wei Chen. 2011. "Synthesis and Reaction Temperature-Tailored Self-Assembly of Copper Sulfide Nanoplates." *Nanoscale* 3 (12): 5096–5102. https://doi.org/10.1039/c1nr10829h.
Xia, Younan, Xiaohu Xia, and Hsin Chieh Peng. 2015. "Shape-Controlled Synthesis of Colloidal Metal Nanocrystals: Thermodynamic versus Kinetic Products." *Journal of the American Chemical Society* 137 (25): 7947–66. https://doi.org/10.1021/jacs.5b04641.

Xie, Yi, Luigi Carbone, Concetta Nobile, Vincenzo Grillo, Stefania D'Agostino, Fabio Della Sala, Cinzia Giannini, et al. 2013. "Metallic-like Stoichiometric Copper Sulfide Nanocrystals: Phase- and Shape-Selective Synthesis, near-Infrared Surface Plasmon Resonance Properties, and Their Modeling." *ACS Nano* 7 (8): 7352–69. https://doi.org/10.1021/nn403035s.

Xie, Yi, Andreas Riedinger, Mirko Prato, Alberto Casu, Alessandro Genovese, Pablo Guardia, Silvia Sottini, et al. 2013. "Copper Sulfide Nanocrystals with Tunable Composition by Reduction of Covellite Nanocrystals with Cu+ions." *Journal of the American Chemical Society* 135 (46): 17630–37. https://doi.org/10.1021/ja409754v.

Zeni, Luigi. n.d. "Lezione Optoelettronica."

Zhang, Hui, Yiqiang Zhang, Jingxue Yu, and Deren Yang. 2008. "Phase-Selective Synthesis and Self-Assembly of Monodisperse Copper Sulfide Nanocrystals." *Journal of Physical Chemistry C* 112 (35): 13390–94. https://doi.org/10.1021/jp801507h.

Zhao, Yixin, Hongcheng Pan, Yongbing Lou, Xiaofeng Qiu, Junjie Zhu, and Clemens Burda. 2009. "Plasmonic Cu 2 - x S Nanocrystals : Optical and Structural Properties of Copper-Deficient Copper (I) Sulfides," no. I: 4253–61.

Zhu, Dongxu, Aiwei Tang, Haihang Ye, Miao Wang, Chunhe Yang, and Feng Teng. 2015a. "Tunable Near-Infrared Localized Surface Plasmon Resonances of Djurleite Nanocrystals: Effects of Size, Shape, Surface-Ligands and Oxygen Exposure Time." *Journal of Materials Chemistry C* 3 (26): 6686–91. https://doi.org/10.1039/c5tc01310k.